Karlsruher Institut für Technologie

PHYSIKALISCHES INSTITUT

FAKULTÄT FÜR PHYSIK

KARLSRUHER INSTITUT FÜR TECHNOLOGIE

Coherent manipulation of microscopic defects in a superconducting phase qubit

Kohärente Manipulation mikroskopischer Defekte in einem supraleitenden Phasen-Qubit

Diplomarbeit

von

Grigorij Grabovskij

June 29, 2010

Referent:	**Prof. Dr. A. V. Ustinov**
Korreferent:	Prof. Dr. M. Siegel
Betreuer:	Dr. P. Bushev

Zusammenfassung

Quantenbits, oder Qubits, sind heutzutage ein heißes Thema in der Physik. Es gibt Theorien, die belegen, dass ein Quantencomputer tatsächlich einige wichtige mathematische Probleme in viel kürzerer Zeit lösen kann als ein herkömmlicher Computer [43]. Der eigentliche Unterschied zwischen den Qubits und den klassischen Bits ist, dass die Qubits den Regeln der Quantenmechanik folgen. Ein Bit kann sich nur in einem der zwei Zustände „0“ oder „1“ befinden. Ein Qubit dagegen ist in der Lage, jede beliebige Superposition $a|0\rangle + b|1\rangle$ anzunehmen, wobei in der Quantenmechanik die jeweiligen Zustände Grundzustand ($|0\rangle$) und angeregter Zustand ($|1\rangle$) genannt werden, und a und b komplexe Zahlen repräsentieren.

Qubits sind ausgezeichnete Objekte, um die Quantenmechanik tiefer zu ergründen und um die Dekohärenz, die die eigentliche Verknüpfung zwischen der Quanten- und der klassischen Physik darstellt, besser zu verstehen. Schon mit zwei oder drei gekoppelten Qubits kann man die komplexe Zeitentwicklung jedes einzelnen Qubits studieren, ohne sich dabei auf statistische Berechnungen von vielen Quantensystemen einschränken zu müssen. Eines der vielversprechendsten Konzepte für die Basis eines Quantencomputers sind elektronische Schaltkreise aus supraleitenden Materialien. Im Gegensatz zu anderen Ansätzen ist bei supraleitenden Qubits die Resonanzfrequenz einstellbar. Des weiteren lassen sich alle bekannten Bauteile aus dem Gebiet der Elektrotechnik einfach an das Qubit anschließen. Das vereinfacht die Kontrolle und die Kopplung sehr. Die Initialisierung, die Operationen und das Auslesen werden durch die Benutzung einer Stromquelle, eines Mikrowellengenerators und eines Spannungsmessgerätes gesteuert. Die Wechselwirkung zwischen den Qubits wird durch induktive oder kapazitive Kopplung vermittelt. Ein anderer wichtiger Vorteil von supraleitenden Qubits ist, dass sie mit bereits etablierten Methoden wie Elektronenstrahllithographie oder Schrägbedampfung (double angle shadow evaporation) hergestellt werden.

Die Experimente in dieser Diplomarbeit wurden mit einem Phasen-Qubit durchgeführt. Ein Phasen-Qubit ist eine supraleitende Schleife, die durch einen Josephson-Kontakt (JK) unterbrochen ist. Diese Schaltung ist auch unter dem Namen rf-

SQUID bekannt. Das Verhalten dieses Qubits bei Temperaturen von einigen Millikelvin wird durch ein Quasiteilchen mit einer Masse in einem ein-dimensionalen, unharmonischen Potential festgelegt. Die Quantenvariable für das Potential ist der Phasenunterschied der beiden Supraleiter quer durch den JK (Josephson-Phase). Da das Qubitpotential von dem zirkulierenden Strom in der Schleife abhängt, kann es mittels eines angelegten externen Flusses kontrolliert werden. Dies wirkt sich auf die Energieunterschiede der Quantenzustände und somit auch auf die Resonanzfrequenz des Qubits aus. Mittels Mikrowellenpulsen, die auf das Qubit geschickt werden, und anschließender Messung des Qubits kann die Eigenfrequenz gefunden werden.

Bei Spektren von Phasen-Qubits werden Aufspaltungen der Resonanzkurve beobachtet. Die Erklärung hierfür sind mikroskopische Zweiniveausysteme (ZNS), die mit dem Qubit wechselwirken. Die eigentliche Natur der ZNS ist noch nicht vollständig erforscht. Jedoch konnte der größte Teil als Gitterdefekte identifiziert werden, die in der Isolationsschicht des JK sitzen. Die Gitterdefekte sind auch als Tunnelsysteme in Gläsern sowie kristallinen Festkörpern bekannt. Aufgrund ihrer starken Wechselwirkung mit dem Qubit werden die ZNS für die relativ kurzen Kohärenzzeiten des Phasen-Qubits verantwortlich gemacht. Auf der anderen Seite haben wir experimentell bewiesen, dass die ZNS auch kohärentes Verhalten zeigen. In unserem Fall war das Phasen-Qubit an zwei ZNS gekoppelt, deren Zerfallszeiten T_1 die des Qubits um einen Faktor von 4 übertrafen. Des weiteren erfüllten diese ZNS die Bedingung eines idealen Atoms: die Dephasierungszeit T_2 ist durch T_1 begrenzt, so dass die Beziehung $T_2 \approx 2T_1$ erfüllt ist.

Um das Verhalten der komplizierten Dynamik, die dieses dreiteilige Quantensystem aufweist, zu verstehen, haben wir zwei Ansätze diskutiert. Der direkte Weg benutzt den Formalismus der Dichtematrix. Dafür wurde eine Simulation im Program Matlab® geschrieben. Es berechnet die Zeitentwicklung der Dichtematrizen für drei Quantensysteme mit je zwei Niveaus, die miteinander wechselwirken. Um auch der Dekohärenz Rechnung zu tragen, wird in dieser Simulation die Mastergleichung in der Lindblad Form für das komplette System bestehend aus 8 Niveaus gelöst. Die einzigen Parameter, die die Simulation benötigt, sind die Resonanzfrequenzen und die Dekohärenzzeiten T_1 und T_2 der Untersysteme sowie die jeweiligen Kopplungskonstanten zwischen dem Phasen-Qubit und den zwei ZNS. Wir haben gezeigt, dass sich die Dynamik durch dieses Model sehr genau beschreiben lässt.

Der andere Ansatz ist eher intuitiv. Wir haben die Repräsentation und die Zeitentwicklung eines Quantensystems bestehend aus zwei Zuständen auf der Blochspäre eingeführt. Der Zustand lässt sich demnach durch den Blochvektor beschreiben. Das ist ein Einheitsvektor mit einem Azimut- und Polarwinkel. Für einen bestimmten

Hamiltonian lässt sich die Zeitentwicklung des Blochvektors durch eine Rotation um eine Achse veranschaulichen, die durch die Eigenzustände des Hamiltonians bestimmt ist. Die Blochsphäre erweist sich auch nützlich bei der Betrachtung des Qubit-ZNS sowie des ZNS-Qubit-ZNS Systems, wenn man sich sinnvoll auf einen zwei-dimensionalen Unterraum einschränkt. Während der Experimente hatte das komplette System maximal nur eine Anregung, somit konnten Zustände, die höheren Anregungen entsprechen, vernachlässigt werden. Da der Grundzustand nicht mit anderen Zuständen interagiert und somit die Rotationen nicht beeinflusst, wurde er auch nicht berücksichtigt. Jedoch muss man beachten, dass das System mit der Zeit in den Grundzustand zerfällt und dass die Amplitude der Oszillationen zwischen den Zuständen deshalb gegen Null konvergiert.

Das gekoppelte Qubit-ZNS System besteht aus vier Zuständen. Somit bleiben nur zwei Zustände übrig, deren Dynamik auf der Blochsphäre sehr anschaulich erklärt werden kann. Wir haben die Eigenzustände des Qubit-ZNS Systems in Resonanz auf zwei Arten präpariert, einmal durch eine zweifache Rotation des Blochvektors um die x- und z-Achse, und ein anderes Mal durch eine direkte Rotation um eine eingestellte Achse. Um diese Zustände nachzuweisen, haben wir das Qubit in Resonanz mit dem ZNS gebracht und das Verhalten der Wahrscheinlichkeit, das Qubit im angeregten Zustand zu finden, beobachtet. Gerade wenn die Eigenzustände generiert wurden, verschwanden die Oszillationen. Durch diese Kohärenz und Kontrollierbarkeit beider Quantensysteme haben wir demonstriert, dass wir in der Lage sind das Qubit und das ZNS in einen beliebigen Zustand zu präparieren. Des weiteren haben wir erklärt, dass sich diese Messdaten auch als eine Tomographie interpretieren lassen. Durch die Einschränkung auf den zwei-dimensionalen Unterraum entsteht nämlich ein Hamiltonian, der exakt die gleiche Form hat wie der eines Qubits, das von Mikrowellen angetrieben wird.

Des weiteren haben wir zum ersten Mal kohärente Dynamik zwischen zwei ZNS hergestellt und diese miteinander verschränkt. Um auch die Dynamik des dreiteiligen ZNS-Qubit-ZNS Systems auf der Blochsphäre zu visualisieren, nutzten wir den relativ großen Energieunterschied der zwei ZNS zueinander von mehr als 200 MHz aus. Wenn sich also das Qubit in Resonanz mit einem ZNS befindet, entspricht die Zeitentwicklung des zweiten ZNS der eines freien Quantensystem. Die Verschränkung beider ZNS kommt zustande, indem man erst das Qubit mit einem ZNS verschränkt, und dann die restliche Anregung des Qubits auf das zweite ZNS überträgt. Auch das haben wir bewiesen. Das System ZNS-Qubit-ZNS wurde einmal in einen verschränkten und ein anderes Mal in einen separablen Zustand der beiden ZNS präpariert, wobei sich das Qubit nach der Präparation in seinem Grundzustand befindet. Nach einem zusätzlichen Mikrowellenpuls konnten wir unterschiedliche Oszillationen beobachten. Während die Schwingungen des verschränkten Zustandes nur die Frequenz aufwiesen, die dem Energieunterschied der beiden ZNS entspricht, zeigten die Oszillationen des separablen Zustandes alle vier Frequenzen der jeweiligen Unterschiede der Energieniveaus.

Unsere Experimente zeigen somit das große Potential des Phasen-Qubits, existierende mikroskopische zwei-Niveau Defekte in Festkörpern quantenmechanisch zu manipulieren. Deshalb erscheint es naheliegend, die ZNS als einen eingebauten Quantenspeicher oder sogar auch als eigenständige Qubits zu benutzen.

Contents

Chapter 1

Introduction

Quantum bits, or qubits, are at the present time a hot topic in physics. In fact, some mathematical problems can be solved on a quantum computer in much shorter times than on conventional computers [43]. The key difference of the qubit in comparison to a classical bit lies in the laws of quantum mechanics. While a state of a bit is either "0" or "1", a state of a qubit is an arbitrary superposition $a|0\rangle + b|1\rangle$, where $|0\rangle$ and $|1\rangle$ are referred to as the ground and excited state, respectively, and a and b are complex numbers. Thus, qubits have to be two-level quantum systems with sufficiently long coherence times. They must be controllable, i.e. one is able to initial them in an arbitrary state and perform a readout. Furthermore, it should be possible to couple qubits for establishing quantum gates and to extend the qubit array to a desired number of qubits. These are the criteria postulated by D. DiVincenzo in the year 2000 [16] which identify a quantum system as a qubit. The set of qubits fulfilling these requirements constitutes the base of a quantum computer.

Although a computer based on quantum manipulation is not yet implemented, qubits already spark great interest in the physical society. Qubits are excellent objects for getting deeper understanding of quantum mechanics and decoherence effects that constitute, in fact, the link between quantum and classical physics. On one hand, the full control over one qubit requires a connection to the laboratory equipment. On the other hand, the qubit has to be sufficiently isolated from the noisy environment to ensure long coherence times. Therefore, most experiments are still the topic of fundamental research. By coupling only two or three qubits it gets possible not only to prove theoretical predictions on an expectation value of many quantum systems, but also to observe the complex state evolution of each qubit independently.

There are many approaches in realizing qubits. For example, photons [29], electron spins [33], nuclear spins [27], trapped ions [7] or NV centers in diamonds (nitrogen-vacancy centers) [5] were experimentally proven to serve as qubits. However, the most promising concept nowadays to create qubits for quantum computation is based on electrical circuits made of superconducting materials. In contrast to other concepts, their resonance frequency is tunable. All standard elements known from electrical engineering can be connected to the qubit just by wiring. This feature makes the controlling and coupling very easy. The initialization, operation and readout of the qubit are controlled by using a current source, a voltmeter and a microwave generator. The interaction between qubits can be established either by inductive or capacitive coupling. Furthermore, superconducting qubits are made on chip using standard techniques like electron beam lithography or double angle evaporation.

Superconducting qubits are based on the effect of the Josephson junction (JJ). The JJ is a tunneling barrier which separates the superconducting layer by an insulator. Due to the junction capacitance and the non-linear Josephson inductance these qubits can be compared with non-linear LC-resonators. Thus, they are multi-level systems with non-equidistant level separation. That is a crucial factor for quantum computation. The two lowest states are defined as the ground state $|0\rangle$ and the excited state $|1\rangle$.

Superconducting qubits are subdivided in three main types: charge, flux and phase qubits. Charge qubits are working only with one Cooper pair that tunnels into or out of a superconducting island. The basis states of a flux qubit are superpositions of the current flowing clockwise or counterclockwise. A phase qubit is based rather on current than on charge, and the levels result from the quantization of an anharmonic potential. Since couple of years also combination of these approaches were presented to the scientific society, e.g. quantronium [53], transmon [46] or fluxonium [34].

Since the resonance frequency of these qubits can be adjusted, one can record its spectrum. In many experiments, the spectrum possesses avoided level crossings. They appear due to microscopic two-level systems (TLSs) coupled to the qubit. The nature of TLSs is still unknown. However, the majority was identified to be lattice defects, which are also known as tunneling systems in glasses as well as in crystalline solids. Due to their strong interaction with the qubit they are held to be responsible for the decoherence effects in superconducting qubits. On the other hand, they constitute also coherent quantum systems, and it was even suggested to use them as quantum memory.

We found that our sample possesses two TLSs whose decay times exceed that of the qubit by a factor of 4. Furthermore, their dephasing time T_2 is limited by the decay time T_1 fulfilling the relation $T_2 \approx 2T_1$ as it would be the case for an ideal atom. Therefore, one can also think to use them as qubits. This work presents experiments on a Josephson junction phase qubit strongly coupled to these two TLSs. The operation regime of the phase qubit is summarized in the second chapter. In the third chapter, the theory required to understand the behavior of the quantum systems is explained. The measurements that prove coherent dynamics between the qubit and one TLS and between the two TLSs mediated by the qubit are presented in the forth chapter.

Chapter 2

Basics of the phase qubit

To understand the behavior of the phase qubit, we have to analyze its elements. As mentioned in the introduction, superconducting phase qubits can be compared with LC-resonators. They possess some capacitive and inductive elements, and therefore form a multi-level system. However, a LC-resonator can not serve as a qubit since all transitions between neighboring states are degenerated. For qubit operations, however, the transition frequency between the states $|0\rangle$ and $|1\rangle$ has to be sufficiently different from other transition frequencies. Due to this reason, superconducting qubits need a strong non-linear element to ensure non-equidistant level separation. That can be achieved by using the Josephson tunnel junction (JJ). It is described in the first section.

In fact, the first proposal for a phase qubit was just a current biased JJ [14, 36]. However, this approach was abandoned. Since it requires a galvanic connection to the laboratory equipment, the decoherence times are too short. Nowadays, a phase qubit consists of a JJ enclosed in a superconducting loop (rf-SQUID [3, 8]) and is controlled via mutual coupling to a flux biasing coil. The readout is done by a dc-SQUID magnetometer which is also inductively coupled to the qubit [32, 8]. The principles of the rf-SQUID and the qubit operation will be discussed in the second section. The chip that served for experiments in this thesis is presented in the third section. In the forth section, designs of a phase qubit consistent with Aluminum double angle evaporation technique (designed for IPHT, Jena) are presented. Unfortunately, due to technical problems and complexity of the chip it has not arrived yet so that I can not present experimental data.

2.1 Josephson junction

2.1.1 Josephson equations

A problem where two superconductor bulks are interrupted by a weak link was considered by B. D. Josephson. A weak link is a small area where the number of Cooper pairs in comparison to the number in the outlying regions is decreased. A narrowing of the superconductor strip line is an example of the weak link. Another interesting example is a carbon nanotube [28]. In our case, the weak link is a thin insulating layer between two overlapping strip lines. Josephson formulated his famous equations in 1962 [26] where he predicted a supercurrent through the junction. He was honored with the Nobel prize in 1973, and in his honor the weak link is referred to as the Josephson junction (JJ).

We follow here the analysis of [32]. According to the theory of Ginzburg and Landau [45], a superconductor is described as a condensate defined by a single wave function Ψ

$$\Psi = \Psi_0(\vec{x}, t) e^{i\phi(\vec{x},t)}, \tag{2.1}$$

where ϕ is a collective phase and the wave function is normalized to the density of the Cooper pairs. When considering two superconductors coupled through a weak link with each other, they may have different collective phases, denoted as ϕ_1 and ϕ_2. The Josephson equations depend only on the Josephson phase

$$\varphi = \phi_1 - \phi_2 \tag{2.2}$$

which is defined as the difference between the two collective phases. The first Josephson equation predicts a supercurrent through the JJ

$$I_S(t) = I_c \sin\varphi(t). \tag{2.3}$$

I_c is the critical current which in turn depends on parameters of the superconductor and on the geometry of the JJ. The first Josephson equation tells that a current biased JJ with a current I_S less than I_c will still be superconducting and will not yield a voltage drop. The second Josephson equation gets important when considering currents above I_c. The resulting voltage drop fulfills the relation

$$\dot{\varphi} = \frac{2e}{\hbar}V = \frac{2\pi}{\Phi_0}V \approx 2\pi \cdot 483.6\frac{\mathrm{MHz}}{\mu\mathrm{V}}V, \tag{2.4}$$

where $\Phi_0 = h/2e$ is the magnetic flux quantum and e is the electron charge. Thus, when there is no voltage drop across the junction, the time derivative of the phase evolution is zero. In contrast, the “velocity” $\dot{\varphi}$ is proportional to the voltage drop with the characteristic factor of the JJ.

2.1.2 The RCSJ model

The rather complex dynamics can be understood by using the RCSJ model [51, 40]. This model is only valid for small JJs. This is the case when its dimensions are significantly smaller than the spatial variations of the Josephson phase, typically 5-30 μm. In contrast, when considering long JJs, the distribution of φ across the junction has also to be taken into account.

According to the RCSJ model, a small JJ consists of three elements in parallel: a superconducting element according to Eqs. (2.3) and (2.4), an ohmic resistance R and a capacitance C (upper part in Fig. 2.1(a)). R is responsible for the damping and thus for the loss of energy. C is the geometrical capacitance. It will be also important in further analysis. To reduce the resonance frequency of the qubit, an additional capacitance C_{ext} can be connected in parallel to the Josephson junction so that

$$C = C_J + C_{ext}, \tag{2.5}$$

where C_J is the intrinsic capacitance of the JJ due to the overlap of the strip lines. According to Kirchhoff's law, the total current flowing through the junction reads

$$0 = -I + I_c \sin\varphi + \frac{V}{R} + C\dot{V} = -I + I_c \sin\varphi + \frac{1}{R}\frac{\Phi_0}{2\pi}\dot{\varphi} + C\frac{\Phi_0}{2\pi}\ddot{\varphi}. \tag{2.6}$$

We can compare this equation with a particle in a one-dimensional potential $U(x)$. According to classical Hamiltonian mechanics, the equation of motion reads

$$0 = m\ddot{x} + D\dot{x} + \frac{\partial U(x)}{\partial x}, \tag{2.7}$$

where m is the mass of the particle and D is the damping constant. By multiplying Eq. (2.6) with $\Phi_0/2\pi$ and identifying x with φ, we find the corresponding factors to be

$$m = C\left(\frac{\Phi_0}{2\pi}\right)^2, \quad D = \frac{m}{RC} \text{ and} \tag{2.8}$$

$$U_J(\varphi) = \frac{I_c\Phi_0}{2\pi}\left(-\frac{I}{I_c}\varphi - \cos\varphi\right). \tag{2.9}$$

By introducing the Josephson energy $E_J = I_c\Phi_0/2\pi$ and normalizing the total current flowing through the junction $\gamma = I/I_c$, we can rewrite Eq. (2.9) as

$$U_J(\varphi) = E_J(-\gamma\varphi - \cos\varphi). \tag{2.10}$$

This "washboard potential" is plotted in Fig. 2.1(a) for three different γ. For currents near I_c the particle can tunnel and run down the potential. This results in a voltage drop across the JJ. The angular resonance frequency ω_0 can be obtained by solving the differential Eq. (2.7). For small underdamped JJ (low damping factor) the expression for ω_0 reads

$$\omega_0 = \sqrt{\frac{1}{m}\frac{d^2U}{d\varphi^2}} = \omega_p\sqrt{\cos\varphi} = \omega_p\sqrt[4]{1-\gamma^2}, \tag{2.11}$$

where the angular plasma frequency ω_p has been introduced:

$$\omega_p = \sqrt{\frac{2\pi I_c}{\Phi_0 C}}. \tag{2.12}$$

One can see from Eq. 2.11 that the resonance frequency decreases with biasing. At a bias current of $I = I_c$ ω_0 is zero. We introduce here the Josephson inductance L_J according to the relation

$$\omega_0 = \frac{1}{\sqrt{L_J C}}. \tag{2.13}$$

Thus,

$$L_J = \frac{\Phi_0}{2\pi}\frac{1}{I_c\cos\varphi} = L_{J,0}\frac{1}{\cos\varphi(t)}, \tag{2.14}$$

where we have defined $L_{J,0} = \Phi_0/2\pi I_c$. Note that the expression for L_J is consistent with the standard definition of the inductance $L = V/\dot{I}$. However, the nature of this inductance is not a stored energy in the magnetic field. The inductance can be rather explained by the kinetic inductance [14, 45] known from the behavior of superconductors at high frequencies.

2.2 The phase qubit

2.2.1 From the current biased Josephson junction to the rf-SQUID

In fact, a phase qubit was initially defined as a current biased Josephson junction [14, 36]. The usual frequencies for JJs lie in the microwave range with frequencies around 5-20 GHz. For example, a frequency of 10 GHz corresponds to a temperature

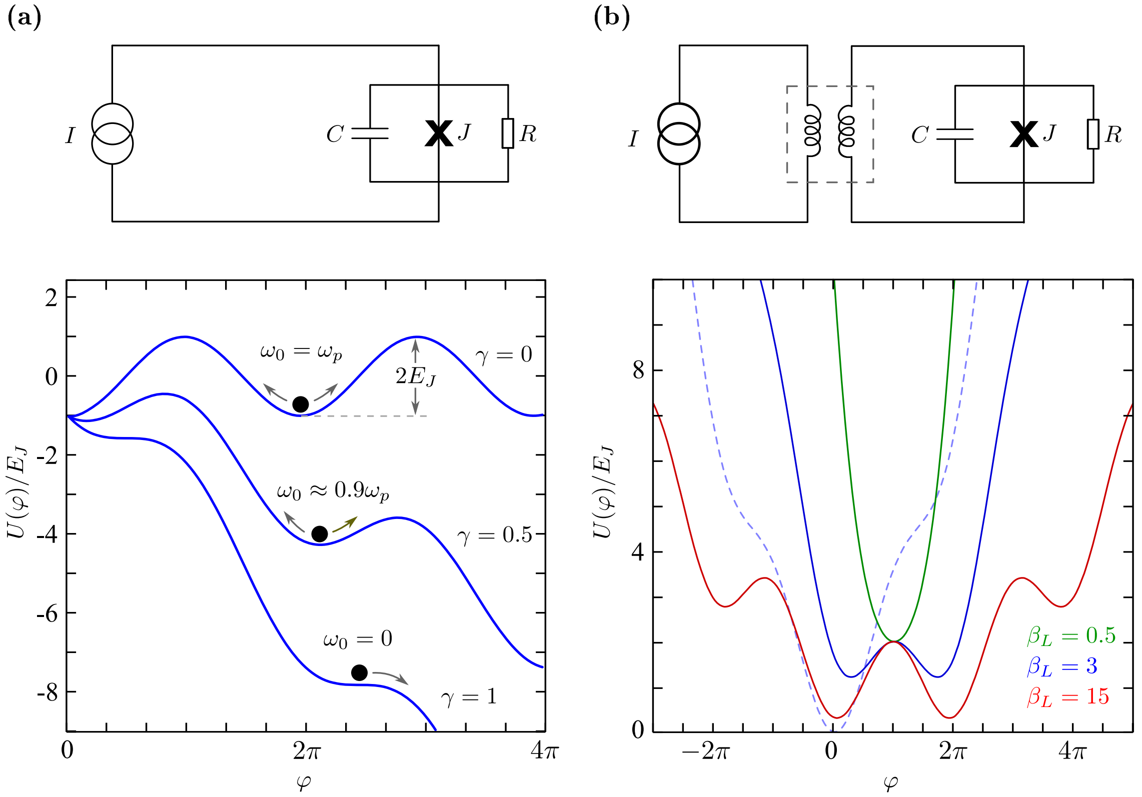

Figure 2.1: **(a)** Upper part: circuit for a current biased JJ. Lower part: The washboard potential is drawn for different current biases. **(b)** Upper part: circuit for a flux biased rf-SQUID. Lower part: The potential is plotted for different β_L-parameters at $\Phi_{ext} = \Phi_0/2$. The potential for $\beta_L = 3$ is also shown for $\Phi_{ext} = 0$ (dashed, light blue curve)

of $T = hf/k_B \sim 500\,\mathrm{mK}$. To ensure that the first excited state can not be populated due to thermal photons, the operating temperature has to be significantly lower. This can be achieved by using a Dilution refrigerator since it can reach temperatures of ~10 mK [23]. Its mode of operation can be compared with evaporative cooling. At temperatures below 1 K, a mixture of two isotopes ^{3}He and ^{4}He undergoes spontaneous phase separation to form a ^{3}He-rich phase and a ^{3}He-poor phase. A transition of ^{3}He atoms from the ^{3}He-rich phase to the ^{3}He-poor phase costs energy which results in a cooling effect. The volume in which this takes place is known as the mixing chamber. In a continuous circulation process, the ^{3}He/^{4}He-mixture is pumped from the side of the ^{3}He-poor phase, outside the mixing chamber ^{3}He is separated from ^{4}He (^{3}He has a lower boiling temperature) and delivered back to the mixing chamber to the ^{3}He-rich phase.

By biasing the JJ with a current, the resonance frequency can be adjusted (Eq. 2.11). Then, the qubit operation is performed by combining the dc-current with the microwave signal. The readout is managed by a short current pulse which tilts the potential so that the particle tunnels and runs down the potential if it is in the excited state. Thus, by measuring the voltage drop across the JJ the state of the qubit can be determined. The first experimental data were published by J. Martinis *et al.* in 2002 [38] which proved that a current biased JJ can perform all operations needed for a single qubit: initialization, Rabi oscillations and readout. The qubit possessed a decay time of 20 ns. The decoherence times could be increased by using a new design. The JJ was enclosed in a loop [36] and controlled by an externally applied flux, the readout was done by a dc-SQUID magnetometer coupled inductively to the qubit. This reduced the number of quasiparticles (electrons) in the JJ since the qubit was not switched to the dissipative regime for the readout. The resonance spectrum of that qubit with the new design possessed a large number of avoided level crossings [48] due to two-level systems (TLSs). TLSs are tunneling systems known from glasses and amorphous materials. Since they strongly interact with the qubit they reduce its decoherence time. A large number of these two-level defects was identified to be located in the insulating layer of the JJ itself [37]. The next boost was then achieved by significantly decreasing the area of the JJ. By increasing the critical current density, I_c and E_J can be kept constant. A big capacitor shunting the JJ compensates the small intrinsic junction capacitance C_J and pulls down ω_p (Eq. 2.12) [50].

2.2.2 rf-SQUID

A rf-SQUID is a superconducting loop interrupted by the JJ which is inductively coupled to the current source (upper part of Fig. 2.1(b)). A detailed analysis of this circuit one can find in [3]. An externally applied magnetic flux Φ_{ext} induces current in the loop which opposes the external flux. The total flux Φ_{tot} in the rf-SQUID can be expressed as

$$\Phi_{tot} = \Phi_{ext} + L_{geo} I = \Phi_{ext} - L_{geo} I_c \sin\varphi, \tag{2.15}$$

where L_{geo} is the geometrical inductance of the loop and I is the current circulating in the loop. Note that φ is negative indicating the suppression of the external flux. Due to the flux quantization in a superconducting loop we find φ to be

$$\varphi = 2\pi \frac{\Phi_{tot}}{\Phi_0} \tag{2.16}$$

Thus, the circulating current I can be expressed as

$$I = \frac{\Phi_{tot} - \Phi_{ext}}{L_{geo}} = \frac{\Phi_0}{2\pi L_{geo}} \left(\varphi - 2\pi \frac{\Phi_{ext}}{\Phi_0} \right). \tag{2.17}$$

The new potential $U(\varphi)$ is the sum of the magnetic energy $L_{geo}I^2/2$ and the junction energy $U_J(\varphi)$ given in Eq. (2.10) [32].

$$U(\varphi) = E_J\left(1 - \cos\varphi + \frac{(\varphi - 2\pi\Phi_{ext}/\Phi_0)^2}{2\beta_L}\right), \tag{2.18}$$

where β_L is defined as

$$\beta_L = \frac{2\pi L_{geo} I_c}{\Phi_0} = \frac{L_{geo}}{L_{J,0}} \tag{2.19}$$

the ratio of the geometric and the Josephson inductance. That potential is plotted for different β_L in Fig. 2.1(b). Aiming the rf-SQUID to operate as a phase qubit, β_L has to satisfy

$$1 < \beta_L < 4.6. \tag{2.20}$$

There are two reasons for that condition. On one hand, it should be possible to initialize the qubit. Therefore, the potential should have at a particular flux bias, e.g. $\Phi_{ext} = 0$, only one well. That corresponds to the upper limit of β_L. On the other hand, the readout of the qubit is only manageable if there are at least two wells in the qubit potential. By applying a flux pulse the potential is tilted so that the quasiparticle tunnels to the other well if it is in the excited state. That defines the lower condition for β_L.

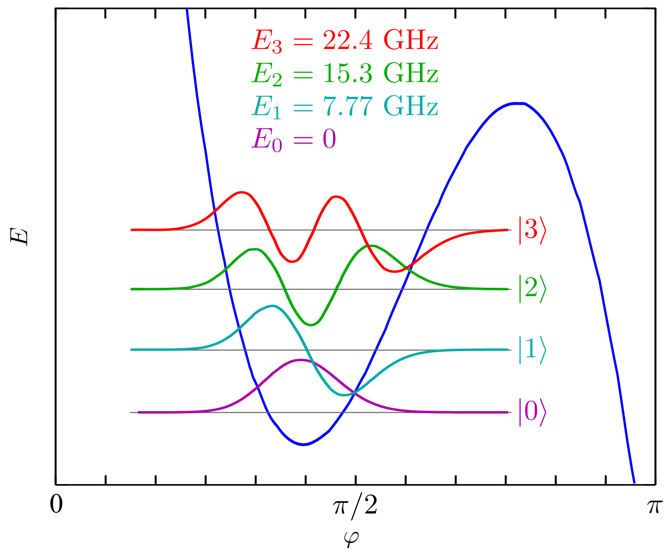

Figure 2.2: The small left well of the double well potential (Eq. 2.18) at $\Phi_{ext} \lesssim \Phi_0$ and the corresponding wave functions are shown. The curve simulates the potential of the chip used in this thesis (Sec. 4.1.1) at an external flux of $0.81\Phi_0$. The parameters are: $I_c = 1.7\mu$A, $L = 720$ pH, $C = 850$ fF and $\beta_L = 3.6$.

J. Lisenfeld wrote a function in the programming language Matlab® [32] which calculates the eigenenergies and eigenstates of the potential given in Eq. 2.18. As parameters, the function requires the critical current I_c, the capacitance C, the loop inductance L and the reduced external flux $\Phi = \Phi_{ext}/\Phi_0$. For the parameters of the chip used in this thesis (see next section) the result of that function is shown in Fig. 2.2 for a reduced external flux of 0.81.

2.3 Designing a phase qubit with aluminum double angle shadow evaporation

2.3.1 The method

The technique of metal deposition from two angles was invented by G. Dolan [17]. In comparison to other fabrication processes, the double angle evaporation method allows to design JJs with a very small area and small critical currents by using one run and one mask only. The wafer is first covered by two resists. A sketch of the mask of a JJ can be seen in the upper part of Fig. 2.3(a). The hatched rectangles are the areas where the upper resist has to be removed. It is developed in a usual way using e-beam lithography. Due to the structure of the lower resist, it is developed faster than the upper one. This forms a resist profile with an undercut, and if the width of the upper resist is thin enough a "Dolan bridge" is created. This situation is drawn in the lower part of Fig. 2.3(a). The black thick line symbolizes the Dolan bridge. Al is sputtered first from one side (left red arrow). Then, O_2 is added so that aluminum oxidizes resulting in a thin layer of AlO_x. Afterwards, Al is sputtered from the other side (right red arrow). The result is displayed in the middle sketch of Fig. 2.3(a). Far away from the JJ, there is a double layer of Al. Near the junction, there is only one layer of Al since each of these two regions was one time in the shadow of the Dolan bridge. Directly under the Dolan bridge, there is a double layer of Al which forms the JJ. Note that if the direction of a superconducting strip line is transversal to the Al evaporation, its width is enlarged. This situation is displayed on the right hand side of Fig. 2.3(a).

For example, a flux qubit fabricated with that technique one can see in Fig. 2.3(b) [6]. There, the junction area of the small JJs is approximately 0.05 μm^2 and the critical current density is 1000 A/cm^2. The charge and the flux qubits are rather small objects and require small junctions because their potential is rather given by the junction parameters than by the geometrical inductance. Thus, it does not constitute a problem to fabricate the whole qubit with the double angle evaporation method. In contrast, a phase qubit needs a large inductance. Usually, the loop for a phase qubit spans over an area of 100x100 μm^2 and possesses two or three

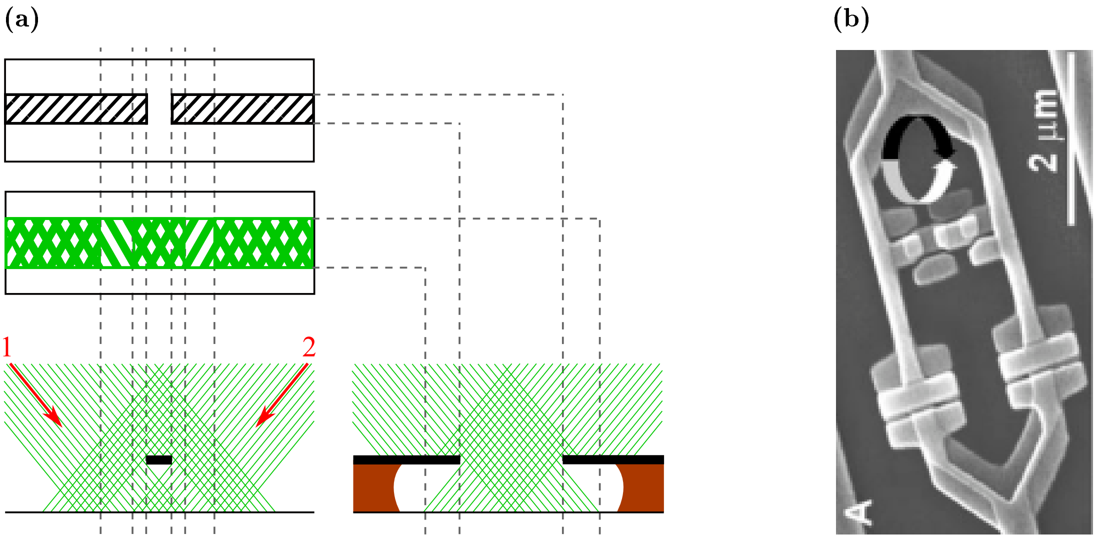

Figure 2.3: **(a)** Al double angle shadow evaporation. Upper part: The mask for one JJ. The small interruption in the strip line will be the "Dolan bridge". Middle part: The result after the evaporation. Lower part: the lower resist (brown) develops faster than the upper resist (black). This creates an undercut and so the Dolan bridge. Al is sputtered on the sample first from one side, and after oxidization of Al from the other side. **(b)** A flux qubit fabricated by the double angle evaporation method. [6].

turns (the connection between different layers is made with vias). Such structures are fabricated by using photo or e-beam lithography, they can not be realized with double angle evaporation.

2.3.2 The chip design

Like in the case of fluxonium qubit [34], we decided to use additional large JJs to increase the inductance of the qubit (Fig. 2.4). We designed some chips from IPHT (Jena, Germany), and so our design has to fit their requirements. The angle of the Al evaporation is ±30° from the vertical axis. The thickness of the lower resist is 290 nm which results in a maximal overlap of 335 nm for zero width of the Dolan bridge. We decided to fix the overlap of the junctions to 200 nm. Thus, the Dolan bridge has a width of 120 nm and a length of 1.5 μm for the large junctions. According to the experience of IPHT, this construction should be stable. With a critical current density of 200 A/cm^2 the critical current I_c^l and the Josephson inductance $L_{J,0}^l$ (Eq. 2.14) are

$$I_c^l = 0.6\mu\text{A and } L_{J,0}^l = 1.6 \text{ nH}. \tag{2.21}$$

The superscript letter l denotes the values for the large junction.

The Josephson energy depends on the critical current and therefore on the small junction. Since there will be a circulating current in the loop we have to ensure that

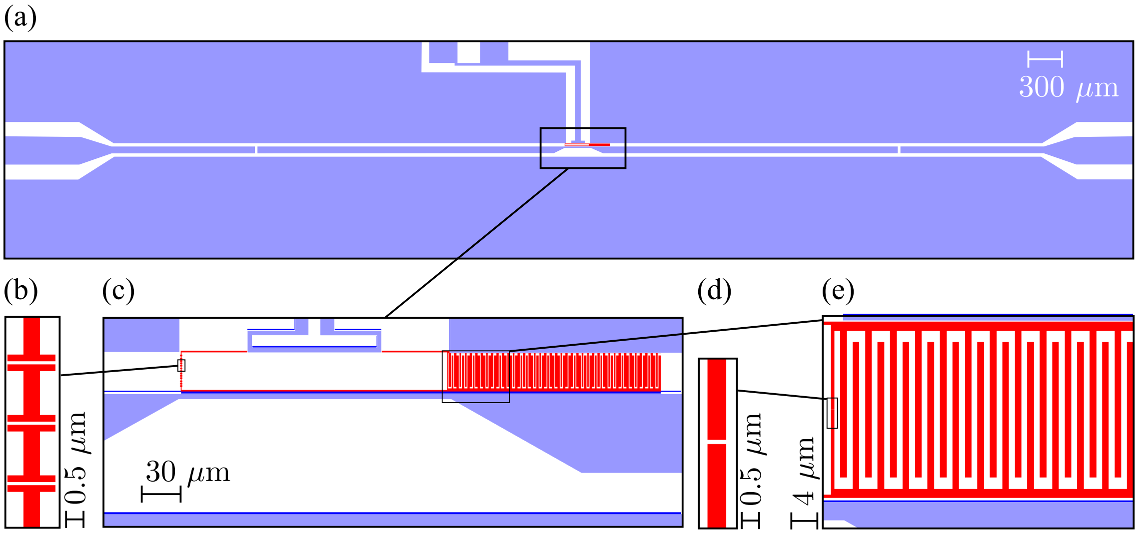

Figure 2.4: The design of the chip for IPHT, Jena. **(a)** The coplanar waveguide resonator (light blue) is shown. The qubit **(c)** is inductively coupled to the resonator. Above the qubit one can see the bias line. A part from the array of 13 large junctions is shown in **(b)** and the small junction in **(d)**. A cutout of the interdigital capacitor is drawn in **(e)**

the Josephson phase of the large junctions does not change significantly, otherwise their inductance will not be constant. One can easily estimate, that if the critical current I_c^s of the small junction is by a factor of 3 smaller than I_c^l than even at a circulating current of I_c^s in the loop the inductance of the large junctions increases only by a factor of 1.06. Thus,

$$I_c^s = \frac{1}{3} I_c^l = 0.2\ \mu\text{A and } L_{J,0}^s = 4.8\ \text{nH}. \tag{2.22}$$

For a phase qubit I_c^s is small, since the height of the potential is defined by E_J. In comparison, the large junctions in the fluxonium qubit are also around a factor three larger that the small junction. However, since fluxonium is assigned to the type of charge qubits, the critical current of the small junction is designed to be ~ 20 nA.

The next aspect concerns the area of the loop. The area should have a maximal possible value. First of all, the qubit will be inductively coupled to a resonator. Second, for a reasonable β_L-parameter (Eq. 2.19) the inductance of the loop should exceed the inductance of the small junction by a factor of 4 (preferable). We decided to fabricate the loop with an area of 200x30 μm^2 with a width of the strip line of 0.5 μm. This corresponds to a geometrical inductance of $L_{geo} = 0.5$ nH (calculated by the program FastHenry). According to the theory, we can increase the β_L-parameter by additional large JJs in the loop. We decided to have 13 large JJs, which results in a β_L factor of 4.4.

Finally, we have to adjust the shunt capacitor. A reasonable plasma frequency for a phase qubit lies in the range of $10-15$ GHz. By using Eq. (2.12), the value for the capacitance is ≈ 100 fF. Since we have to work in only one layer, the capacitor has to have a long, interdigital form. We fixed the thickness of the fingers to be 1.5 μm to ensure that they will not break due to the undercut. The length of the fingers and the distance between them is 25 μm and 1 μm, respectively. Thus, the capacitor prolongs the width of the qubit of 30 μm. The capacitance for a pair of fingers was simulated to be 2.64 fF (program SONNET®, test version). To have 100 fF we need 38 finger pairs resulting in a total length of 150 μm.

The whole qubit with a total area of 350x30 μm^2 was embedded in a coplanar $\lambda/2$ resonator made of Nb. The width of the central line is 60 μm and the gap between the central line and ground is 31 μm. This results in an inductance and capacitance density of $\mathcal{L} = 405$ nH/m and $\mathcal{C} = 160$ pF/m so that $Z = \sqrt{\mathcal{L}/\mathcal{C}} \approx 50\Omega$. The resonance frequency and the quality factor of the resonator are designed to match 9 GHz and 10^4 (length of resonator: 6450 μm, gap of the capacitors in the central line: 25 μm), respectively. At these frequencies the qubit has 2-3 levels. For the bias line of the qubit the ground of the resonator was interrupted. Before the measurement, we plan to connect the two grounds via bonding wires. The coupling strength between qubit and resonator was estimated to be $\sim$ 50 MHz. All parameters concerning qubit and resonator are summarized in Tab. (2.1).

(a)

	small JJ	large JJ
area [μm^2]	0.2x0.5	0.2x1.5
I_c [μA]	0.2	0.6
E_J [GHz]	99	300
$L_{J,0}$ [nH]	1.6	0.55

(b)

	resonator - qubit	bias line - qubit
mutual inductance [pH]	100	20

Table 2.1: **(a)** The parameters of the small and large JJ. **(b)** The mutual inductances between qubit and resonator, and qubit and the bias line.

Chapter 3

Two-level quantum systems

This chapter summarizes the theory necessary to understand the physical behavior of a qubit coupled to two-level quantum systems. The first part considers the two-level quantum system in general. The Bloch sphere is introduced to represent the quantum states as vectors and to visualize the time evolution. The master equation in the Lindblad form is explained and applied on three examples (Rabi oscillations, Relaxation and Ramsey fringes). The second part introduces the parasitic two-level systems (TLS) and their coupling to the qubit.

3.1 Two-level quantum system

A two-level quantum system is the basis of any coherent dynamical processes on quantum scale. Even such complex and macroscopic objects like superconducting qubits are well described by quantum mechanics. Almost all applications like e.g. quantum information processing [56] or single photon source [22] use the lowest two levels.

3.1.1 Description of the Bloch sphere

Let us start this chapter by considering a quantum system described by an usual time-independent Hamiltonian H

$$H = \begin{pmatrix} E & g/2 \\ g^*/2 & 0 \end{pmatrix}, \tag{3.1}$$

where g is the coupling strength with a possible complex phase. In the case of $g = 0$, the eigenstates of the Hamiltonian are the ground state $|0\rangle$ and the excited state $|1\rangle$

with corresponding energies 0 and E. The vectorial notation for theses states is

$$|0\rangle = \begin{pmatrix} 0 \\ 1 \end{pmatrix},\ |1\rangle = \begin{pmatrix} 1 \\ 0 \end{pmatrix}. \tag{3.2}$$

Any quantum mechanical state $|\psi\rangle$ of this system can be expressed as a superposition of the basis states with complex coefficients. These four degrees of freedom shrink to two after normalizing and setting the phase of the ground state to zero. Thus, $|\psi\rangle$ can be written as

$$|\psi\rangle = \cos\frac{\theta}{2}|0\rangle + \sin\frac{\theta}{2}\ e^{-i\varphi}|1\rangle = \begin{pmatrix} \sin\frac{\theta}{2}\ e^{-i\varphi} \\ \cos\frac{\theta}{2} \end{pmatrix} \tag{3.3}$$

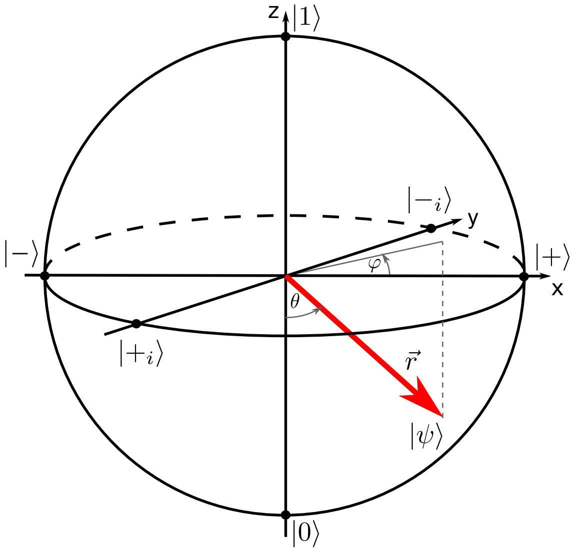

Figure 3.1: Bloch sphere. Quantum states and (x,y,z)-representations: $|0\rangle$ (0,0,-1), $|1\rangle$ (0,0,1), $|-\rangle=(|0\rangle-|1\rangle)/\sqrt{2}$ (-1,0,0), $|+\rangle=(|0\rangle+|1\rangle)/\sqrt{2}$ (1,0,0), $|+_i\rangle=(|0\rangle+i|1\rangle)/\sqrt{2}$ (0,-1,0), $|-_i\rangle=(|0\rangle-i|1\rangle)/\sqrt{2}$ (0,1,0). The state $\psi\rangle$ (red bold arrow) is defined by the angles θ and φ.

This representation is very convenient because it is possible to represent the state graphically by a vector on a so called Bloch sphere (Fig. 3.1). The Bloch sphere is located symmetrically on a right-handed coordinate system with a radius of 1. The ground state $|0\rangle$ is placed on the bottom ($z = -1$) and the excited state $|1\rangle$ on top ($z = +1$). On the x-axis, the states $|-\rangle$ ($x = -1$) and $|+\rangle$ ($x = +1$) and on the y-axis the states $|+_i\rangle$ ($y = -1$) and $|-_i\rangle$ ($y = +1$) are located. These states are defined as follows:

$$|+\rangle = \frac{|0\rangle + |1\rangle}{\sqrt{2}};\ |-\rangle = \frac{|0\rangle - |1\rangle}{\sqrt{2}};\ |+_i\rangle = \frac{|0\rangle + i|1\rangle}{\sqrt{2}};\ |-_i\rangle = \frac{|0\rangle - i|1\rangle}{\sqrt{2}} \tag{3.4}$$

Please note here the similarity of the definitions. The factor in front of the lower state $|0\rangle$ is always real and positive. And only the state $|1\rangle$ may have a phase resulting from the complex coefficient. Although the cosine term in Eq. (3.3) might be negative for some θ, one can always make it positive by multiplying the state by -1. The representation of the state ψ as a vector on the Bloch sphere then follows automatically from the angles θ and φ. For example, if $\theta = 0°$ we have the ground state. $\theta = 90°$ and $\varphi = 90°$ result in the state $|-_i\rangle$. Since the Bloch sphere is not only spanned by the quantum states but also by the x-,y-,z-axis it is obvious to find also an expression of the quantum mechanical state in the (x,y,z)-representation. One can easily verify that the components of the position vector $\vec{r}$ can be written as

$$r_j = \langle\psi|\sigma_j|\psi\rangle,\ j \in \{x, y, z\} \tag{3.5}$$

with σ_j being the Pauli matrices [42]. Then,

$$\vec{r} = \begin{pmatrix} \sin\theta\cos\varphi \\ \sin\theta\sin\varphi \\ -\cos\theta \end{pmatrix}. \tag{3.6}$$

Let us now come back to the Hamiltonian in Eq. (3.1). The eigenenergies are

$$E_\pm = \frac{E}{2} \pm \frac{1}{2}\sqrt{E^2 + |g|^2}. \tag{3.7}$$

$|\psi_\pm\rangle$ denote the eigenstates. They can be expressed as

$$|\psi_+\rangle = \cos\frac{\alpha}{2}|0\rangle + \sin\frac{\alpha}{2}\ e^{-i\beta}|1\rangle = \begin{pmatrix} \sin\frac{\alpha}{2}\ e^{-i\beta} \\ \cos\frac{\alpha}{2} \end{pmatrix} \text{ and} \tag{3.8}$$

$$|\psi_-\rangle = -\sin\frac{\alpha}{2}|0\rangle + \cos\frac{\alpha}{2}\ e^{-i\beta}|1\rangle = \begin{pmatrix} \cos\frac{\alpha}{2}\ e^{-i\beta} \\ -\sin\frac{\alpha}{2} \end{pmatrix} \tag{3.9}$$

$$\text{with } \beta = \text{phase}(g),\ \tan\alpha = -\frac{|g|}{E}. \tag{3.10}$$

β is here the phase of the coupling strength g when it is written in the form $g = |g|\exp(i\beta)$. It is necessary to mention that the states $|\psi_+\rangle$ and $|\psi_-\rangle$ always point into opposite directions on the Bloch sphere. This results from the fact that all eigenvectors of different eigenvalues of a hermitian matrix are lying in orthogonal subspaces. Due to the factor 1/2 in front of the angle α we have to add 180° to α of e.g. $|\psi_+\rangle$ to get the orthogonal state $|\psi_-\rangle$. The states $|\psi_\pm\rangle$ are thus forming an axis which will be very important when regarding the time evolution of a Bloch vector.

3.1.2 Time evolution and rotation

The time evolution of a two-level quantum system starting with an arbitrary state $|\psi_0\rangle$ is well known. Here we want to show the corresponding time dependent behavior of the Bloch vector.

Let $|\psi_0\rangle$ have the form

$$|\psi_0\rangle = \cos\frac{\theta}{2}|0\rangle + \sin\frac{\theta}{2}\; e^{-i\varphi}|1\rangle = \begin{pmatrix} \sin\frac{\theta}{2}\; e^{-i\varphi} \\ \cos\frac{\theta}{2} \end{pmatrix} \tag{3.11}$$

The time evolution of this state is given by the Schrödinger equation

$$\frac{d}{dt}|\psi(t)\rangle = \frac{d}{dt}U(t)|\psi_0\rangle = -\frac{i}{\hbar}HU(t)|\psi_0\rangle, \tag{3.12}$$

where $U(t)$ denotes a unitary matrix. We use standard methods to solve this equation. First, the coordinates of the initial state are transformed to the basis of the eigenstates of H. Thus, the Hamiltonian gets a diagonal form where the entries are the eigenenergies. After that, the resulting vector is transformed back. The time dependent unitary operator $U(t)$ can then be rewritten as

$$U(t) = e^{-iHt/\hbar} = Be^{-iDt/\hbar}B^{-1} \tag{3.13}$$

with the unitary matrix[1] B and the diagonal matrix[2] D

$$B = \begin{pmatrix} \sin\frac{\alpha}{2}\; e^{-i\beta} & \cos\frac{\alpha}{2}\; e^{-i\beta} \\ \cos\frac{\alpha}{2} & -\sin\frac{\alpha}{2} \end{pmatrix} \text{ and } D = \begin{pmatrix} \omega/2 & 0 \\ 0 & -\omega/2 \end{pmatrix}, \tag{3.14}$$

where

$$\omega = \frac{\sqrt{E^2+g^2}}{\hbar}. \tag{3.15}$$

Note here, that the matrices B and D are expressed in such a way that the state

---

[1] The columns of the matrix B are the new basis vectors w_i. B then describes the coordinate transformation from the new basis to the Cartesian one: $B\cdot(e_i)_W = w_i$, and thus $(e_i)_W = B^{-1}\cdot w_i$.

[2] Originally the eigenenergies of $|\psi_\pm\rangle$ are $E_\pm$ (Eq. 3.7). The equal terms $E/2$ are not important: $U'(t) = Be^{i(D+E/2\cdot\mathbb{1})t/\hbar}B^{-1} = U(t)\cdot e^{iEt/2\hbar}$. The additional complex factor $e^{i\lambda}$ with unity length doesn't affect the behavior of $U(t)$.

$|\psi_+\rangle$ has higher energy than the state $|\psi_-\rangle$. The resulting unitary operator is

$$U(t) = \begin{pmatrix} \cos\frac{\omega}{2}t + i\sin\frac{\omega}{2}t\,\cos\alpha & -i\sin\frac{\omega}{2}t\sin\alpha\, e^{-i\beta} \\ -i\sin\frac{\omega}{2}t\sin\alpha\, e^{i\beta} & \cos\frac{\omega}{2}t - i\sin\frac{\omega}{2}t\,\cos\alpha \end{pmatrix}. \tag{3.16}$$

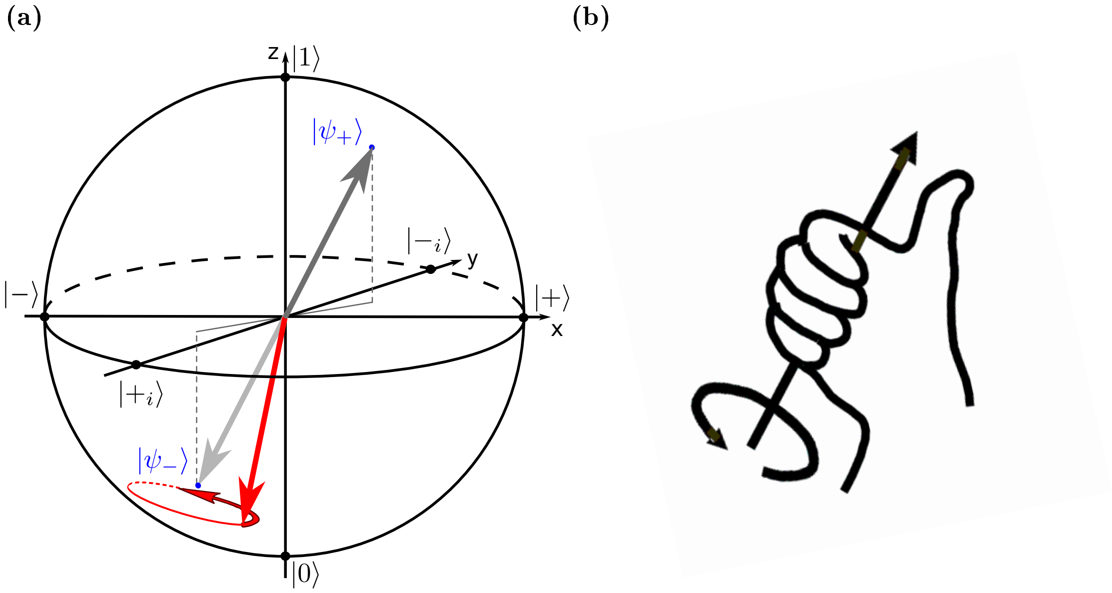

Figure 3.2: **(a)** Time evolution of a Bloch vector (red arrow without contour): the vector rotates around the axis formed by the eigenstates of the Hamiltonian $|\psi_+\rangle$ (dark grey arrow) and $|\psi_-\rangle$ (grey arrow) with $E_+ > E_-$. The curved red arrow with the dark edge shows the direction of rotation. **(b)** Visualization of (a) with the right-hand rule. The thumb points into direction of the energetically higher state $|\psi_+\rangle$

Let us now visualize this time dependence on the Bloch sphere. Therefore, we compare $U(t)$ with the standard expression for an unitary rotation matrix

$$R_{\vec{n}}(\delta) = \mathbb{1}\cos\frac{\delta}{2} - i\sin\frac{\delta}{2}\vec{n}\cdot\vec{\sigma} \tag{3.17}$$

which rotates a vector around the unit vector $\vec{n} = (n_x, n_y, n_z)$ by an angle δ [32]. The vector $\vec{\sigma} = (\sigma_x, \sigma_y, \sigma_z)$ symbolizes the set of Pauli matrices. Thus, we find that $\delta = \omega t$ and $\vec{n}$ is pointing exactly to the state $|\psi_+\rangle$ fulfilling Eq. (3.6)

$$\vec{n} = \begin{pmatrix} \sin\alpha\cos\beta \\ \sin\alpha\sin\beta \\ -\cos\alpha \end{pmatrix}. \tag{3.18}$$

So, for future experiments we can find the time evolution of the Bloch vector very easily. The matrix in Eq. (3.17) and thus also $U(t)$ are satisfying the right-hand rule. This means, if the thumb of the right hand is parallel to the rotation axis defined by the eigenstates and is pointing to the energetically higher state, then the other fingers show the direction of rotation of the Bloch vector (Fig. 3.2).

3.1.3 Density matrix and Lindblad equation

The formalism of density matrix was introduced by Lev Landau [30] and independently by John von Neumann in 1927. The density matrix allows not only to describe a pure state which is a superposition of the basis states but also statistical mixtures. Therefore, this representation is crucial when considering the preparation and time evolution of a quantum system in thermal equilibrium including the effects of decoherence. The expectation value of many measurements on one system (e.g. qubit or TLS) can be reproduced as well as the expectation value of one experiment on an ensemble consisting of many systems (e.g. the effective spin of many atoms, tunneling systems in solid materials).

The density matrix ρ is defined as

$$\rho = \sum_j p_j |\psi_j\rangle\langle\psi_j|, \ \sum_j p_j = 1, p_j > 0, \tag{3.19}$$

where $|\psi_j\rangle$ are pure states. The sum over more then two different pure states yields a statistical mixture. The main idea is to have a matrix where the diagonal reflects the probability to measure a system in a particular state. Therefore, the trace always has to be 1. The non-diagonal entries shed light on the coherence of the pure states of one system or entanglement between different subsystems.

Let us consider some special cases to demonstrate these ideas. For the ground state and the excited state,

$$\rho_0 = |0\rangle\langle 0| = \begin{pmatrix} 0 & 0 \\ 0 & 1 \end{pmatrix}, \ \rho_1 = |1\rangle\langle 1| = \begin{pmatrix} 1 & 0 \\ 0 & 0 \end{pmatrix}. \tag{3.20}$$

For example, we have prepared the qubit in the excited state. Due to relaxation, after some time the probability to measure the qubit in the state $|1\rangle$ will be only 0.5. This is exactly the case of a statistical mixture without any coherence:

$$\rho_{mixt} = 0.5\rho_1 + 0.5\rho_0 = \begin{pmatrix} 0.5 & 0 \\ 0 & 0.5 \end{pmatrix}. \tag{3.21}$$

In contrast, the density matrix for the pure states $|\pm\rangle$ is

$$\rho_+ = |+\rangle\langle+| = 0.5 \begin{pmatrix} 1 & 1 \\ 1 & 1 \end{pmatrix}, \ \rho_- = |-\rangle\langle-| = 0.5 \begin{pmatrix} 1 & -1 \\ -1 & 1 \end{pmatrix}. \tag{3.22}$$

Here, the off-diagonal entries clearly identify these pure states. If the system in this case is not affected by relaxation but only by so called dephasing, the result will be that only the off-diagonal terms will vanish with time. Thus, both density matrices $\rho_\pm$ will pass into ρ_{mixt} (Eq. 3.21). The former pure states then are transformed into a statistical mixture where only the corresponding probabilities $|\langle 1| \pm |1\rangle|^2 = |\langle 0| \pm |0\rangle|^2$=0.5 are conserved. For a more detailed analysis of mathematics, in particular of the quantum mechanics, please refer to literature [10].

The Schrödinger equation in the density matrix formalism can be written as

$$\dot{\rho} = \sum_i p_i(|\dot{\psi_i}\rangle\langle\psi_i| + |\psi_i\rangle\langle\dot{\psi_i}|) = -\frac{i}{\hbar}[H,\rho] \tag{3.23}$$

This expression describes already the time evolution of a statistical mixture. However, it still operates in a perfectly isolated environment. This means that the time evolution of each pure state the density matrix consists of is given by the usual Schrödinger equation (Eq. 3.12). But unfortunately, it is not possible to completely decouple a system from the surrounding world. First of all, any quantum system is in thermal equilibrium with the environment. Furthermore, depending on the experimental setup, the system is knowingly coupled to electric fields, magnetic fields, measurement devices, etc. This fact manifests itself in so called decoherence process.

To describe this process of damping, a master equation is needed. We will use here the Lindbladian form [12]:

$$\dot{\rho} = -\frac{i}{\hbar}[H,\rho] + \sum_j \Gamma_j \mathcal{L}_j, \text{ with} \tag{3.24}$$

$$\mathcal{L}_j = L_j \rho L_j^\dagger - \frac{1}{2}(L_j^\dagger L_j \rho + \rho L_j^\dagger L_j). \tag{3.25}$$

L_j and Γ_j are the Lindbladian operator and the characteristic rate corresponding to the jth decoherence channel, respectively. Since the first term describes the time evolution of the Schrödinger equation, the whole information about the damping is concentrated in the other terms. The Lindblad equation is a first-order differential equation with a sum on the right side of the equal sign. Thus, apart from the unperturbated evolution, the solution will have exponentially decaying factors depending on the form of L_j. In the next sections for the most important experiments (Rabi oscillations, relaxation and Ramsey fringes) the solution for the Lindblad equation is calculated.

Let us consider now the three decoherence channels. Therefore, we define the entries of the 2x2 density matrix. By using the hermiticity and the trace of 1, we find

$$\rho = \begin{pmatrix} \rho_{11} & \rho_{10} \\ \rho_{10}^* & 1-\rho_{11} \end{pmatrix}. \tag{3.26}$$

The notation is in such a way that $\rho_{11} = \langle 1|\rho|1\rangle$ and $\rho_{10} = \langle 1|\rho|0\rangle$. As mentioned above, there are a lot of ways for the excited state to loose its energy and so to relax into the ground state. This effect is described by the characteristic time $T_1 = 1/\Gamma_1$. The corresponding matrix is the annihilation operator σ_-

$$\sigma_- = \begin{pmatrix} 0 & 0 \\ 1 & 0 \end{pmatrix}. \tag{3.27}$$

By setting $L_1 = \sigma_-$ we get

$$\mathcal{L}_1 = \begin{pmatrix} -\rho_{11} & -\rho_{10}/2 \\ -\rho_{10}^*/2 & \rho_{11} \end{pmatrix} \tag{3.28}$$

Usually, also the creation operator $\sigma_+ = \sigma_-^T$ is taken into account. However, in our regime it is negligible. The excited state of the qubit has a frequency which is higher than 6 GHz. In contrast, the corresponding "thermal" frequency at a temperature of 30 mK is about $f_{therm} = k_B T/h \approx 0.6$ GHz. The probability to have an excitation can be expressed by the Boltzmann factor:

$$\langle 1|\rho|1\rangle = e^{-hf/k_BT} \approx 5 \cdot 10^{-5} \tag{3.29}$$

The next very important decoherence channel is pure dephasing. The Lindblad operator L_2 equals the matrix $\sigma_z/\sqrt{2}$ and so

$$\mathcal{L}_2 = \begin{pmatrix} 0 & -\rho_{10} \\ -\rho_{10}^* & 0 \end{pmatrix} \tag{3.30}$$

with the corresponding characteristic time $T_2^* = 1/\Gamma_2^*$. Here the star does not symbolize a complex conjugated time but distinguishes from the time T_2 defined in following.

The complete Linbladian equation for our case then is

$$\frac{d}{dt}\begin{pmatrix}\rho_{11} & \rho_{10} \\ \rho_{10}^* & 1-\rho_{11}\end{pmatrix} = -\frac{i}{\hbar}[H,\rho] + \begin{pmatrix}-\Gamma_1\rho_{11} & -\Gamma_2\rho_{10} \\ -\Gamma_2\rho_{10}^* & \Gamma_1\rho_{11}\end{pmatrix} \tag{3.31}$$

where

$$\Gamma_2 = \frac{1}{T_2} = \frac{\Gamma_1}{2} + \Gamma_2^* = \frac{1}{2T_1} + \frac{1}{T_2^*} \tag{3.32}$$

is the inverse dephasing time.

The operator $\mathcal{L}_1$ is responsible for both decoherence processes decay and dephasing, whereas $\mathcal{L}_2$ affects only dephasing and does not describe any energy transfer between states and environment. Therefore, it serves as the operator for the so called pure dephasing channel. In the case of large T_2^*, the dephasing time is limited by T_1 so that $T_2 \lesssim 2T_1$. This relation is applied to the ideal atom. The decoherence times T_1 and T_2 can be extracted from two measurements [6] decay (Sec. 3.1.5) and Ramsey experiment (Sec. 3.1.6).

Here I want to outline briefly the differences and similarities of terms used in nuclear magnetic resonance (NMR) and quantum information. Theoretical methods of describing the behavior of a spin like Bloch vector representation or Rabi oscillations have their roots in the field of NMR [54]. However, when considering the same spin as a qubit it is common to use the definitions accepted in the field of quantum computation [43]. I suppose that happened because NMR is dealing with an ensemble of many spin 1/2-systems, whereas for quantum information the behavior of each individual spin is important. Both theories use the decay time (or longitudinal relaxation) T_1 in the same way. In contrast, in NMR it is common to define the dephasing time (or transverse relaxation time) T_2 as the dephasing due to unregulated perturbations or due to thermal equilibrium or magnetic field fluctuations. Therefore, T_2 concerns each spin 1/2-system independently and is called homogeneous dephasing time. The inhomogeneous dephasing time T_2' accounts for rather constant energy shifts due to e.g. inhomogeneity of the applied magnetic field or the coupling of a large number of spins resulting in the Zeemann-shift, dipole-dipole interaction, etc. [15]. However, theoretically it is very difficult to take them all into account. Either way, the spins then are subjects of slightly different conditions which results in dephasing of the complete ensemble given by the inverse characteristic time $1/T_2^* = 1/T_2 + 1/T_2'$. Thus, the measured time in the Ramsey experiment always yields T_2^*. To cancel the inhomogeneous dephasing resulting in the homogeneous time T_2, other experimental method like the Spin-Echo [19] must be employed. The pulse sequence in Spin-Echo is the same as in the Ramsey experiment but with an additional π-pulse between the two $\pi/2$-pulses. This corresponds to a rotation of the Bloch vector in one direction and then its return after applying the π-pulse.

In the field of quantum information, T_2 denotes the total dephasing time for one qubit only, depending on both T_1 (decay rate) and T_2^* (pure dephasing) (Eq. 3.32). Since the qubit does not interact with other qubits of the same energy (when detuned from two-level systems) the only pure dephasing channel is noise which is mostly homogeneous. Since qubits are operated in a GHz regime it is reasonable to distinguish between low frequency and high frequency noise. In fact, the first one can be considered as an inhomogeneity because it does not change the conditions for the qubit during one pulse sequence but affects rather many independent measurements. Therefore, the low frequency noise component should be canceled out in a Spin-Echo experiment. The pure dephasing time of the phase qubit used in this thesis (Sec. 4.1.1) increases by a factor of 3 when performing the Spin-Echo experiment [50].

3.1.4 Rabi oscillations

Rabi oscillations are coherent oscillations between two states of a quantum system when they interact with a resonant or near-resonant field. First, they were described in the area of NMR by Isidor Rabi in 1938 (Nobel Price in 1944). Rabi oscillations appear for example when a spin 1/2-system is perturbated by an oscillating magnetic field [54] or in quantum optics, when an atom is passing a cavity field [47]. We may employ the basic results of that theory in describing the oscillations of our artificial atom driven by a microwave field. To understand this rather complex effect in this section the two standard approximations are introduced and the Lindbladian equation (3.25) is solved.

Rotating wave approximation (RWA) and Janes-Cummings-Hamiltonian

The description of Rabi oscillations in a quantized electro-magnetic field was made by E. Jaynes and F. Cummings [25]. The main simplification is referred to as the rotating wave approximation (RWA). We follow here the analysis of Zimmermann [57]. The total Hamiltonian can be written as

$$H_{tot} = H_q + H_0 + H_{int}, \tag{3.33}$$

with H_q and $H_0 = \hbar\omega_0(a^\dagger a + 1/2)$ being the Hamiltonian of the qubit (Eq. 3.1) and the microwave field, respectively. H_{int} is the interaction term wich is usually expressed as

$$H_{int} = \vec{E} \cdot \vec{d}. \tag{3.34}$$

$\vec{E}$ is the oscillating electrical field of the microwave and $\vec{d}$ is the dipole operator of the qubit. The field quantization allows us to write the electrical field in terms of the creation and annihilation operator $a^\dagger$ and a

$$\vec{E} \propto (a + a^\dagger). \tag{3.35}$$

Assuming that the microwave field is polarized parallel to the x-axis $\vec{E} = E_x \vec{e_x}$. This component then couples only to the part of the dipole of the qubit in x-direction so that the dipole operator of the qubit can be simplified to

$$d_x \propto \sigma_x = \sigma_- + \sigma_+. \tag{3.36}$$

Thus, the interaction Hamiltonian can be written as

$$H_{int} = \frac{\hbar\Omega_0}{2}(\sigma_- + \sigma_+)(a + a^\dagger) \tag{3.37}$$

with the coupling strength $\hbar\Omega_0$. In the Heisenberg picture the time evolutions of the operators a, $a^\dagger$ and $\sigma_\pm$ are

$$a(t) \propto e^{-i\omega_0 t},\ a^\dagger(t) \propto e^{i\omega_0 t} \text{ and} \tag{3.38}$$

$$\sigma_\pm(t) \propto e^{\pm i\omega_q t}. \tag{3.39}$$

The core idea of the RWA is to neglect the fast oscillating terms $\sigma_+ a^\dagger$ and $\sigma_- a$ [55]. When considering long time scales, i.e. when the slow oscillating terms $\sigma_- a^\dagger$ and $\sigma_+ a$ show little variations, this approximation can be justified by two reasons. First of all, they violate the conservation of energy since they implicit a simultaneous excitation of the qubit and creation of a photon and a decay of the qubit and annihilation of a photon, respectively. This would be important only on a very short time scale. Secondly, the RWA is only valid if the frequency is in the vicinity of the resonance of the atom. The fast oscillating terms then will very fast average to zero since they rotate in opposite directions with angular frequencies of $\sim \pm 2\omega_0$ to each other. Therefore, they are called "counter rotating terms".

The resulting Hamiltonian is called Jaynes-Cummings-Hamiltonian (JCH). It has the form

$$H_{JCH} = H_q + H_0 + \frac{\hbar\Omega_0}{2}(\sigma_- a^\dagger + \sigma_+ a) \tag{3.40}$$

Dressed states model

For further analysis we need a matrix representation for the JCH defined in Eq. (3.40). In first instance, it is not obvious how to solve this problem since the JCH works with the electro-magnetic field which has an infinite number of modes. However, the dressed states picture suggests a solution.

Let us assume, the microwave field has n photons. If the qubit is in its ground state the initial state then is $|0, n\rangle$.

$$H_{JCH}|0, n\rangle = \left(n + \frac{1}{2}\right)\hbar\omega_0|0, n\rangle + \frac{\hbar\Omega_0}{2}\sqrt{n}|1, n-1\rangle \tag{3.41}$$

If on the other hand we consider the state $|1, n-1\rangle$ then

$$H_{JCH}|1, n-1\rangle = E + \left(n - \frac{1}{2}\right)\hbar\omega_0|1, n-1\rangle + \frac{\hbar\Omega_0}{2}\sqrt{n}|0, n\rangle \tag{3.42}$$

We see that the JCH combines only the states $|0, n\rangle$ and $|1, n-1\rangle$. Thus, the energy is oscillating between the qubit and the microwave field with a frequency scaling with $\sqrt{n}$. It is then not necessary to consider how many photons the electro-magnetic field has as long as the number is very high.

By shifting the lower energy to 0 and setting $\Omega = \Omega_0\sqrt{n}$ this Hamiltonian can be expressed in the matrix notation as

$$H_{JCH} = \begin{pmatrix} E - \hbar\omega_0 & \hbar\Omega/2 \\ \hbar\Omega/2 & 0 \end{pmatrix}. \tag{3.43}$$

By using this Hamiltonian, the angular Rabi frequency is defined as the difference between the eigenenergies $E_\pm$ (Eq. 3.7)

$$\Omega_R = \frac{E_+ - E_-}{\hbar} = \sqrt{\left(\frac{E}{\hbar} - \omega_0\right)^2 + \Omega^2} \tag{3.44}$$

The matrix in Eq. (3.43) looks very similar to the Hamiltonian considered at the beginning of this chapter (Eq. 3.1). The difference is on one hand that the coupling between the states is a real number. This has no physical meaning since it follows from the assumption that the microwave field is polarized parallel to the x-axis. On the other hand, the energy of the excited state is lowered by the energy of the microwaves. This is exactly the idea of the RWA to express the time evolution of the qubit with respect to the field.

By using the formalism described in Sec. (3.1.2) we can draw the time evolution of the qubit on the Bloch sphere. Since the coupling here is real the angle β in Eq. (3.18) is zero. If the qubit is in resonance with the microwave field $E = \hbar\omega_0$, $\alpha = 90°$ and so the Bloch vector is performing a full rotation around the x-axis from the ground state to the excited state (Fig. 3.2). In the off-resonant limit the rotation axis converges to the z-axis either with α going to zero ($E < \hbar\omega_0$) or approximating 180° ($E > \hbar\omega_0$). The corresponding Rabi oscillations will then be faster with a much lower amplitude (Fig. 3.3a). It is necessary to mention here that also when the microwave source is turned off and $\Omega = 0$ Eq. (3.43) is still valid. This results when considering the evolution of a two-level quantum system in the rotating frame defined by the microwave frequency $\omega_0/2\pi$ [55].

Damping of Rabi oscillations

After analyzing the driven qubit without any losses it is also important to consider decoherence effects. The coherent interaction between the qubit and the microwave field is a crucial factor for applications on longer time scales. To simplify matters, let the qubit be in resonance with the microwave. The Hamiltonian (Eq. 3.43) can then be written as

$$H_{res} = \hbar \begin{pmatrix} 0 & \Omega/2 \\ \Omega/2 & 0 \end{pmatrix}. \tag{3.45}$$

As discussed above, the eigenstates of H_{res} are $|\pm\rangle$ and so $\alpha = 90°$ and $\beta = 0°$. Starting at the ground state, the corresponding rotation matrix $U(t)$ (Eq. 3.16) dictates the time evolution of the system

$$|\psi(t)\rangle = \begin{pmatrix} -i\sin\frac{\Omega}{2}t \\ \cos\frac{\Omega}{2}t \end{pmatrix}. \tag{3.46}$$

The Bloch vector will always stay in the yz-plane. The density matrix for this undamped rotation is

$$\rho_{no\,dec}(t) = |\psi(t)\rangle\langle\psi(t)| = \frac{1}{2}\begin{pmatrix} 1-\cos\Omega t & -i\sin\Omega t \\ i\sin\Omega t & 1+\cos\Omega t \end{pmatrix}. \tag{3.47}$$

Rabi oscillations without decoherence are shown in Fig. 3.3(a).

Let us now find a simple expression for a driven qubit which also involves damping. In order to be able to compare the resulting density matrix with the ideal one (Eq. 3.47) we define

$$\rho(t) = \begin{pmatrix} \rho_0(t) & -i\rho_1(t) \\ i\rho_1(t) & 1-\rho_0(t) \end{pmatrix}. \tag{3.48}$$

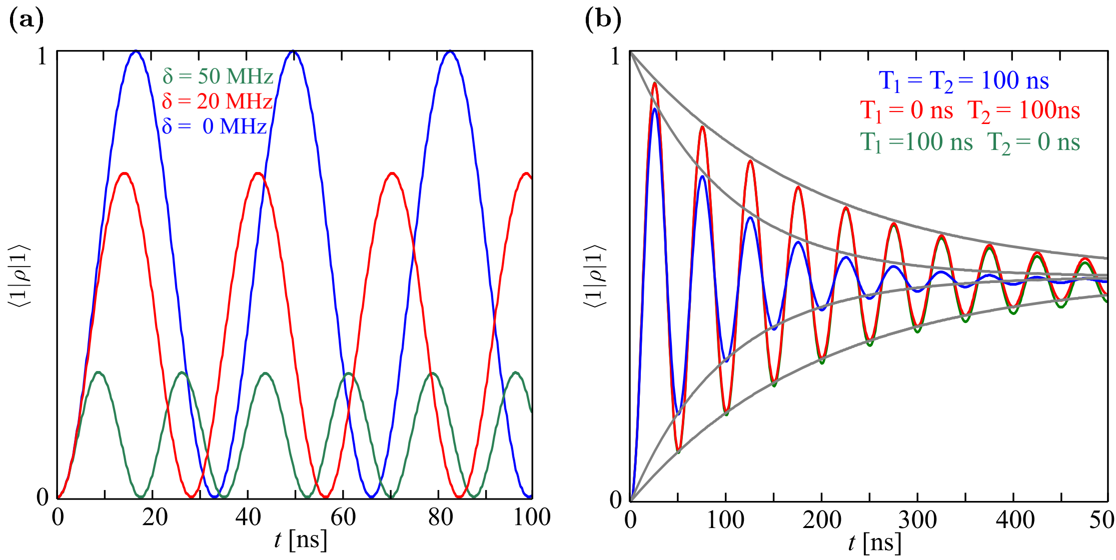

Figure 3.3: **(a)** Rabi oscillations without decoherence effects at different detunings are shown, **(b)** decaying Rabi oscillations are displayed

with real functions ρ_0 and ρ_1. Using the master equation in the form of Eq. (3.31) we find the differential equations for these two unknown functions that have to be solved:

$$\dot{\rho}_0 = -\Gamma_1\rho_0 + \Omega\rho_1 \qquad \text{and} \tag{3.49}$$

$$\dot{\rho}_1 = -\Omega\rho_0 - \Gamma_2\rho_1 + \frac{\Omega}{2}. \tag{3.50}$$

An equivalent expression is

$$\begin{pmatrix}\dot{\rho}_0\\ \dot{\rho}_1\end{pmatrix} = \begin{pmatrix}-\Gamma_1 & \Omega\\ -\Omega & -\Gamma_2\end{pmatrix}\begin{pmatrix}\rho_0\\ \rho_1\end{pmatrix} + \begin{pmatrix}0\\ \Omega/2\end{pmatrix} \tag{3.51}$$

One can easily verify that the solution of a differential equation of the form

$$\dot{y} = Ay + b \tag{3.52}$$

with a matrix A and a vector b is

$$y(t) = C \cdot e^{At} - A^{-1}b, \tag{3.53}$$

where C is the starting condition. We will see in further equations that the homogeneous part will decay with time. Thus, the result for the steady state is

$$\begin{pmatrix} \rho_{0\infty} \\ \rho_{1\infty} \end{pmatrix} = \frac{1}{2(\Gamma_1\Gamma_2 + \Omega^2)} \begin{pmatrix} \Omega^2 \\ \Omega\Gamma_1 \end{pmatrix}. \tag{3.54}$$

The decay rates of the qubit and the Rabi frequencies are

$$\Gamma_1 \approx \Gamma_2 \approx 10\text{MHz} < \Omega \approx 2\pi \cdot 30\text{MHz} \tag{3.55}$$

allow us to simplify the expression of the stationary solution to

$$\begin{pmatrix} \rho_{0\infty} \\ \rho_{1\infty} \end{pmatrix} \approx \begin{pmatrix} 0.499 \\ 0.03 \end{pmatrix} \approx \begin{pmatrix} 0.5 \\ 0 \end{pmatrix}. \tag{3.56}$$

This is in good agreement with the time independent part of the undamped oscillations in Eq. (3.47).

The procedure to find also the time dependent part of the solution is the same as in Eq. (3.13) by using eigenstates and eigenvalues. Unfortunately, the calculations get very complicated so that we have to make the approximation

$$\left| \frac{\Gamma_1 - \Gamma_2}{\Omega} \right| \ll 1. \tag{3.57}$$

The eigenvalues of the matrix in Eq. (3.51) then are

$$\lambda_\pm = -\frac{\Gamma_1 + \Gamma_2}{2} \pm i\Omega, \tag{3.58}$$

and the eigenvectors simplify to

$$v_\pm = \begin{pmatrix} 1 \\ \pm i \end{pmatrix}. \tag{3.59}$$

Putting everything together, the final solution is

$$\begin{pmatrix} \rho_0(t) \\ \rho_1(t) \end{pmatrix} = \frac{1}{2} e^{-\frac{\Gamma_1+\Gamma_2}{2}} \begin{pmatrix} \cos\Omega t & \sin\Omega t \\ -\sin\Omega t & \cos\Omega t \end{pmatrix} \cdot C + \begin{pmatrix} 0.5 \\ 0 \end{pmatrix}. \tag{3.60}$$

By comparing this result with the density matrix in Eq. (3.47) we find the starting condition $C = (-1 \;\; 0)$ and so

$$\rho(t) = \frac{1}{2} e^{-t/\tau} \begin{pmatrix} -\cos\Omega t & -i\sin\Omega t \\ i\sin\Omega t & \cos\Omega t \end{pmatrix} + \begin{pmatrix} 0.5 & 0 \\ 0 & 0.5 \end{pmatrix}, \tag{3.61}$$

where τ is the characteristic time of the damping

$$\tau = \left(\frac{1}{2T_1} + \frac{1}{2T_2}\right)^{-1}. \tag{3.62}$$

Fig. 3.3(b) displays decaying Rabi oscillations simulated by the Lindbladian equation. The exponentially falling curves with corresponding characteristic rates of 1/100 ns (blue) and 1/200 ns (red and green).

In our experiments, the qubit is excited by a so called π-pulse. This means, that the qubit is performing Rabi oscillations for half a period. Accordingly, a $\pi/2$-pulse and a $3\pi/2$-pulse bring the Bloch vector of the qubit to the states $|-_i\rangle$ and $|+_i\rangle$, respectively.

3.1.5 Decay

The measurement of the relaxation yields the time T_1. After exciting the qubit by a π-pulse and waiting for different times the probability is measured that the qubit is still in the excited state. The Hamiltonian has the simple form

$$H = \begin{pmatrix} E & 0 \\ 0 & 0 \end{pmatrix}. \tag{3.63}$$

The density matrix can be expressed as

$$\rho = \begin{pmatrix} \rho_{11} & 0 \\ 0 & 1-\rho_{11} \end{pmatrix} \tag{3.64}$$

with the initial condition $\rho_{11}(0) = 1$. Thus, the master equation (3.31) shrinks to the differential equation

$$\dot{\rho_{11}} = -\Gamma_1 \rho_{11}, \tag{3.65}$$

and so

$$\rho_{11}(t) = e^{-\Gamma_1 t}. \tag{3.66}$$

The energy transfer between the states and the environment is described only by the rate Γ_1.

3.1.6 Ramsey fringes

Norman Ramsey was a PhD student of Isidor Rabi. Among other things, he explored the core spin by using magnetic resonance techniques (Nobel Price in 1989). The

Ramsey experiment for determination of the dephasing time T_2 is named in honor of him. Fig. 3.4(a) displays the pulse sequence. The bleary upper curve symbolizes the excitation spectrum of the qubit in dependence on the external flux (Sec. 2.2.2). After the first $\pi/2$-pulse the Bloch vector reaches the state $|-_i\rangle$. Then the qubit evaluates freely performing some rotations around the z-axis with possible detuning from the resonance. Before the sequence is terminated by the readout a second $\pi/2$-pulse is applied on the qubit.

In terms of the RWA and the rotating frame picture we can rephrase this problem as follows: starting from the state $|-_i\rangle$ the Bloch vector oscillates around the z-axis with the detuning angular frequency $\delta = E/\hbar - \omega_0$. Then it is mapped back on the state $|-_i\rangle$ because this state will be rotated to $|1\rangle$ by the second pulse. Indeed, also during the two $\pi/2$-pulses the qubit is subject to decoherence. And the considerations made here do not neglected that. The fact that the initial state is not $|0\rangle$ and the final state is not $|1\rangle$ affects only the contrast of the oscillations. Since the loss of information is in each experiment and for each $\pi/2$-pulse the same the damping of the oscillations is in fact independent of the two pulses.

The Hamiltonian for the free evolution of the Bloch vector in this case is

$$H = \hbar \begin{pmatrix} \delta & 0 \\ 0 & 0 \end{pmatrix}. \tag{3.67}$$

By using the general expression of the 2x2 density matrix

$$\rho = \begin{pmatrix} \rho_{11} & \rho_{10} \\ \rho_{10}^* & 1-\rho_{11} \end{pmatrix}. \tag{3.68}$$

we can express the time dependence by solving the master Eq. (3.31) as

$$\rho(t) = \begin{pmatrix} C_0 e^{-\Gamma_1 t} & C_1 e^{-\Gamma_2 t} e^{-i\delta t} \\ C_1^* e^{-\Gamma_2 t} e^{i\delta t} & 1 - C_0 e^{-\Gamma_1 t} \end{pmatrix}, \tag{3.69}$$

where C_0 and C_1 are independent starting parameters. By setting

$$\rho(0) = |-_i\rangle\langle -_i| = \frac{1}{2} \begin{pmatrix} 1 & -i \\ i & 1 \end{pmatrix} \tag{3.70}$$

we find $C_0 = 1/2$ and $C_1 = -i/2$. Thus, the expectation value to measure the system in the state $|-_i\rangle$ or equivalently to find the system in the excited state after

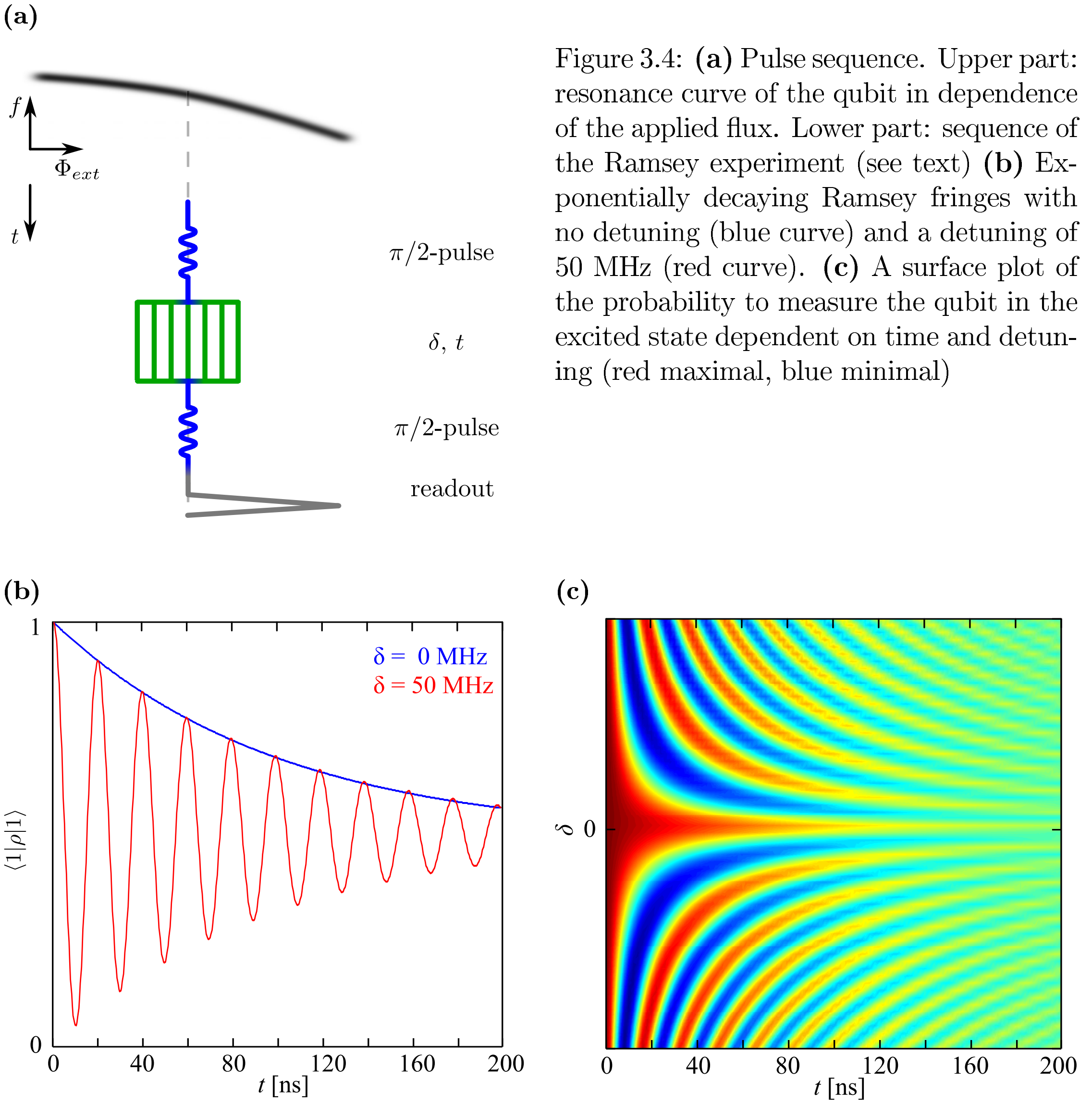

Figure 3.4: **(a)** Pulse sequence. Upper part: resonance curve of the qubit in dependence of the applied flux. Lower part: sequence of the Ramsey experiment (see text) **(b)** Exponentially decaying Ramsey fringes with no detuning (blue curve) and a detuning of 50 MHz (red curve). **(c)** A surface plot of the probability to measure the qubit in the excited state dependent on time and detuning (red maximal, blue minimal)

the whole pulse sequence is

$$\langle -_i|\rho(t)|-_i\rangle = \frac{e^{-\Gamma_2 t}}{2}\cos\delta t + \frac{1}{2}. \tag{3.71}$$

This expression describes oscillations with the detuning frequency $\delta/2\pi$ and the damping rate Γ_2. In Fig. 3.4(b), the blue curve with no detuning acts as the envelope for the red oscillating curve. A surface plot with varying detuning and time between the two $\pi/2$-pulses is displayed.

3.2 Microscopic two-level systems (TLSs)

As described in the introduction, when considering decoherence in a superconducting qubit one has always to take also the parasitic two-level systems (TLS) in to account. The origin of two-level systems in superconducting qubits is still not understood. It seems that they have the same nature as tunneling systems in solids [20]. According to [37, 35, 2, 52] TLSs are microscopic defects which either are located in the tunneling barrier of the Josephson Junction or at the surface of the superconducting layer.

When going into the quantum limit, things get much easier. The TLSs, as the name already tells, are two-level quantum systems and they completely obey the quantum mechanical rules. The characteristic times of these natural defects show rather random behavior [2, 24]. In our case, the two TLSs used in experiments have much longer coherence times than the qubit. Furthermore, they fulfill the relation $T_2 \approx 2T_1$. Thus, the decoherence is limited by the relaxation process. This means, TLSs have a very low pure dephasing rate indicating a small coupling to the environment. In contrast, TLSs may interact very strongly with the qubit [18, 44].

3.2.1 Interaction and Hamiltonian

As in the case of Rabi oscillations the interaction occurs due to electric fields. This can be modeled again by the annihilation and creation operators. In the basis of the qubit and TLS eigenstates $\{|1\rangle,\ |0\rangle\} \otimes \{|e\rangle,\ |g\rangle)\} = \{|1e\rangle,\ |1g\rangle,\ |0e\rangle,\ |0g\rangle\}$

$$H_{int} = g_c(\sigma_+^q \otimes \sigma_-^s + \sigma_-^q \otimes \sigma_+^s), \tag{3.72}$$

where the superscript letters q and s correspond to qubit and TLS, respectively. g_c denotes a real coupling strength. When expressing each Hamiltonian of the two systems in the rotating frame of the microwave field with the frequency $\omega_0/2\pi$ the total Hamiltonian for the hybrid qubit-TLS system H_{qs} reads

$$H_{qs} = H_q \otimes \mathbb{1}_2 + \mathbb{1}_2 \otimes H_s + H_{int} = \begin{pmatrix} \hbar(\delta\omega_q + \delta\omega_s) & 0 & 0 & 0 \\ 0 & \hbar\delta\omega_q & g_c/2 & 0 \\ 0 & g_c/2 & \hbar\delta\omega_s & 0 \\ 0 & 0 & 0 & 0 \end{pmatrix}, \tag{3.73}$$

where $\hbar\delta\omega_q = E_1 - \hbar\omega_0$ and $\hbar\delta\omega_s = E_e - \hbar\omega_0$ are defined as the energy differences between the respective system and the microwave field.

When turning on the microwave source the qubit will start to perform Rabi oscillations at a frequency $\Omega_q/2\pi$. Mediated by the second excited state of the qubit $|2\rangle$ the TLS performs also Rabi oscillations with the frequency $\Omega_s/2\pi$ which is by a factor of approximately 5 smaller [31]. This can be modeled as an effective complex coupling strength $-i\hbar\Omega_q$ between the states $|1g\rangle$ and $|1e\rangle$. The Hamiltonian for the driven qubit-TLS system then reads

$$H_{qs,mic} = \begin{pmatrix} \hbar(\delta\omega_q + \delta\omega_s) & -i\hbar\Omega_s & \hbar\Omega_q & 0 \\ i\hbar\Omega_s & \hbar\delta\omega_q & g_c/2 & \hbar\Omega_q \\ \hbar\Omega_q & g_c/2 & \hbar\delta\omega_s & 0 \\ 0 & \hbar\Omega_q & 0 & 0 \end{pmatrix}. \tag{3.74}$$

3.2.2 Beating between the qubit and TLS

To have a full picture of the dynamics between qubit and TLS we have to look on the resulting Hamiltonian and find expressions for these damped oscillations. A detailed analysis of the relaxation of the qubit in presence of TLSs was made by Müller *et. al.* [41]. Here, I want to extract two particular cases.

The first case considers the situation, when the excited qubit is brought into resonance with one TLS. Since we have only one excitation in the system the state $|1e\rangle$ remains unpopulated. By neglecting this state the effective Hamiltonian shrinks to a 3x3 matrix:

$$H_{eff} = \begin{pmatrix} \hbar\delta\omega_q & g_c/2 & 0 \\ g_c/2 & \hbar\delta\omega_q & 0 \\ 0 & 0 & 0 \end{pmatrix}. \tag{3.75}$$

Note here the similarity of the upper 2x2 matrix in H_{eff} and the Hamiltonian for a resonantly driven qubit H_{res} (Eq. 3.45). Since one can always add a multiple of the identity matrix to a Hamiltonian they have the same shape. In correspondence to the Rabi oscillations, we introduce here the π-rotation where the states of the qubit and of the TLS are swapping with each other. An equal entanglement between the two systems is achieved by a $\pi/2$-rotation. On the other hand, the time evolution of the initially excited qubit described by H_{eff} shows not only damped oscillations but also the average value itself decreases to zero. The reason for the latter statement is that here the ground state is the steady state and it does not participate in any rotations.

Fig. 3.5(a) displays the simulated (Sec. 3.2.3) curve. All required parameters were taken from Tab. (4.1, TLS is TLS2). The decay rates of the beating are given as follows:

$$\Gamma_{av} = \frac{1}{2}\left(\Gamma_1^q + \Gamma_1^s\right) \text{ and}$$
$$\Gamma_{osc} = \frac{1}{2}\left(\Gamma_1^q + \Gamma_1^s\right) + \frac{1}{2}\left(\Gamma_2^{*q} + \Gamma_2^{*s}\right) = \frac{1}{2}\left(\Gamma_{av} + \Gamma_2^q + \Gamma_2^s\right), \tag{3.76}$$

where Γ_1, Γ_2^* and Γ_2 correspond to the rates of relaxation, pure dephasing and dephasing, respectively. The superscript letters q and s represent the qubit and the TLS.

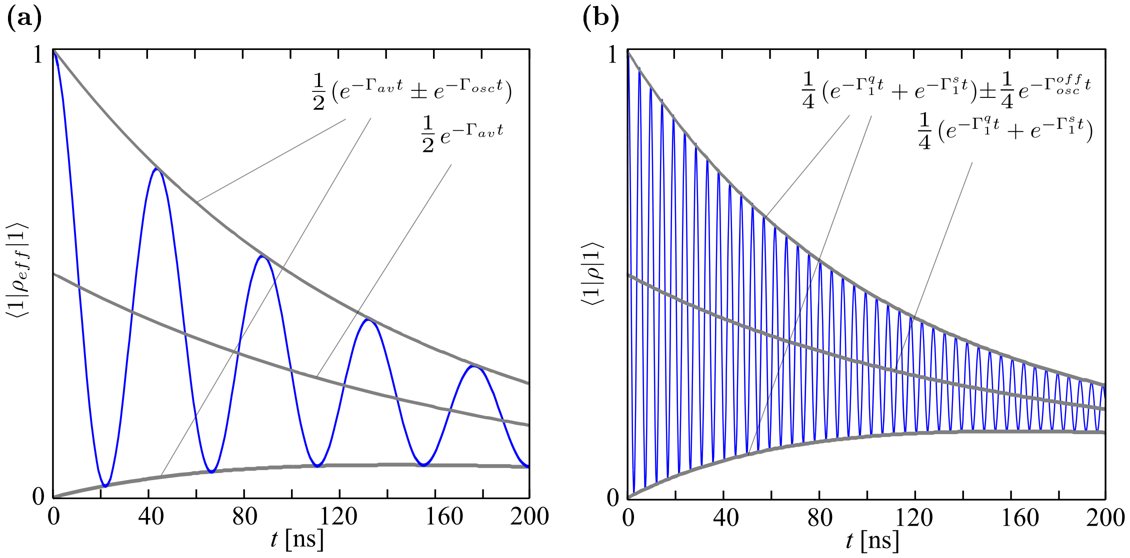

Figure 3.5: **(a)** Beating between the excited qubit and TLS at resonance.The damping oscillations consist of two damping parts: the decay rate for the average value is denoted as Γ_{av}, that for the oscillating part as Γ_{osc}. **(b)** Ramsey-type oscillations between qubit and TLS (see text). The parameters for both simulated curves were extracted from Tab. (4.1). The TLS corresponds to TLS2.

The calculated inverse decaying times for our qubit-TLS2 system are $\Gamma_{av} = 1/177$ ns and $\Gamma_{osc} = 1/118$ ns. It is remarkable that both times are higher than the characteristic time $\tau = 105$ ns for the Rabi oscillations (Eq. 3.62).

The second case is slightly more difficult. During the measurements described in Sec. (4.2 and 4.3) the qubit is entangled with the TLS by a $\pi/2$-rotation and then detuned for some time. To simplify matters, for the theoretical curve depicted in Fig. 3.5(b) the initial as well as the projection state and the detuning were set to $|-_i\rangle^{qs} = (|0e\rangle - i|1g\rangle)/\sqrt{2}$ (Sec. 4.2.1) and 210 MHz, respectively. The detuning is large enough so that we can neglect an influence of the TLS to the decay time of the qubit and vice versa. Thus, the decrease of the average value of the oscillations is proportional to the sum of the two corresponding exponential factors. The expression for the damping factor of the oscillating part in the off-resonant regime depends only on the decay and dephasing times of the respective subsystems

$$\Gamma_{osc}^{off} = \frac{1}{2}\left(\Gamma_1^q + \Gamma_1^s\right) + \Gamma_2^{*q} + \Gamma_2^{*s} = \Gamma_2^q + \Gamma_2^s. \tag{3.77}$$

In the case of the qubit-TLS2 hybrid system Γ_{osc}^{off} is about 1/89 ns.

3.2.3 Simulation

To compare the experimental results with theoretical predictions and to extract important parameters with the fitting method, I wrote a simulation in the programming language Matlab®, Version 7.7.0.471 (R2008b). My program takes three two-level quantum systems into account. They are denoted as TLS1, qubit and TLS2. The eigenstates of this tripartite hybrid system reads

$$\text{basis} = \{|e\rangle, |g\rangle\} \otimes \{|1\rangle, |0\rangle\} \otimes \{|e\rangle, |g\rangle\}. \tag{3.78}$$

The total Hamiltonian has the form

$$H_{tot} = (H_{s1} \otimes \mathbb{1}_2 \otimes \mathbb{1}_2) + (\mathbb{1}_2 \otimes H_q \otimes \mathbb{1}_2) + (\mathbb{1}_2 \otimes \mathbb{1}_2 \otimes H_{s2}) + (H_{int,1} \otimes \mathbb{1}_2) + (\mathbb{1}_2 \otimes H_{int,2}). \tag{3.79}$$

The zero level is set to the microwave energy. The Hamiltonians of the respective systems H_{s1}, H_q, H_{s2} (TLS1, qubit, TLS2) equal the matrix of Eq. (3.43). When the microwave source is on Ω is set to a corresponding value, if no field is present $\Omega = 0$. The interaction Hamiltonians $H_{int,1}$ and $H_{int,2}$ (qubit-TLS1, qubit-TLS2) are defined in Eq. (3.72). If desired, also the respective longitudinal couplings and a direct interaction between the two TLSs can be included.

The simulation takes also account of decoherence effects via the Lindbladian equation and the corresponding decoherence channels (Sec. 3.1.3). Although the master equation is a first-order differential equation it is possible to calculate the time evolution of the quantum states exactly. Therefore, a superoperator of the dimensions $\dim(H_{tot})^2$ x $\dim(H_{tot})^2$ is constructed and the density matrix then can be calculated via the usual procedure by using eigenbasis and eigenvalues of the superoperator [11].

The simulation is in good agreement with the experimental results. To entangle two TLSs (Sec. 4.3) the right pulse sequence was even first found theoretically before the measurement was done.

Chapter 4

Experimental results

In the first part the chip and the experimental setup are presented and the quantum systems are characterized. The main experiments showing coherent dynamics of the qubit with one and two TLSs are described in the second and third part, respectively.

4.1 Experimental setup and characterization of the quantum systems

4.1.1 Description of the UCSB chip

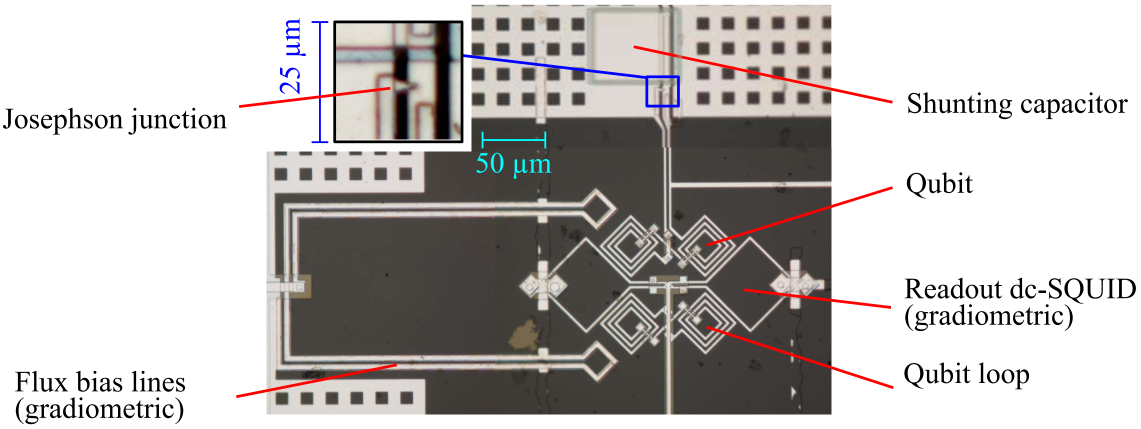

Figure 4.1: The chip from UCSB. The experiments in this thesis were performed with that chip. The design of the bias lines and SQUID is gradiometric. Below the SQUID an additional coil is placed which has the same parameters as the qubit loop to reduce the net flux in the SQUID generated by the qubit.

The chip was provided to our group by Prof. John Martinis (UCSB). First results with these chips are published in 2006 [50]. A photo of the chip is shown in Fig. 4.1. Note that the group of Martinis *et al.* attach great importance to gradiometric design. The flux bias lines and the dc-SQUID are arranged in such a way that the integral of the flux over the SQUID loop is zero. The flux enters symmetrically into the SQUID from two sides and its effect is annihilated. In contrast, the qubit is placed closer to one bias line than to the other resulting in a non-zero flux bias. To compensate the flux generated from the current in the qubit loop on the opposite side of the SQUID an additional coil is designed, which has the same form and inductance as the loop of the qubit. Thus, it is ensured that the SQUID magnetometer is always at the best working point resulting in a readout of the qubit with high fidelity.

Aluminum serves as superconductor and AlO_x as the isolation layer. The junction area was 1 $\mu\mathrm{m}^2$, which is, for example, a factor of ten smaller in comparison to the chips fabricated at Hypres Inc. With a critical current density of 170 $\mathrm{A/cm}^2$ I_c equals 1.7 μA. The ratio of the loop inductance of 720 pH to the Josephson inductance ($L_{J,0} = 200$ pH) results in the β_L parameter (Eq. 2.19) of 3.6. The self capacitance of the JJ equals 50 fF. This would correspond to a plasma frequency $\omega_p/2\pi$ of 51 GHz (Eq. 2.12). Therefore, the JJ is shunted by a large plate capacitor with an area of 60x60 $\mu\mathrm{m}^2$ and filled with silicon-nitride. The capacitance was designed to be 800 fF so that ω_p is reduced by a factor of 4 to 12 GHz. The decoherence times T_1 and T_2 were measured to be 110 and 90 ns, respectively. We were experimenting with this qubit already for 4 years, the decoherence times have not changed at all.

4.1.2 Experimental setup

On the left side we present the photo of the dilution unit of the cryostat. The sample holder with the chip inside is fixed at the bottom, where the mixing chamber (Sec. 2.2.1) produces a temperature of less than 30 mK. The experimental setup is outlined in Fig. 4.2. The green box symbolizes the chip (Sec. 4.1.1), which is cooled to a temperature of approximately 30 mK. To manipulate the qubit (blue) microwave pulses are required. Therefore, the continuous wave generated by the microwave source (μW) is prepared with the help of two mixers in series. The DC pulses of the first port of the arbitrary waveform generator (Tektronix, AWG7062B) applied on the mixers switch the microwave on and off. Before the microwaves reach the qubit they are attenuated by approximately 30 dB and they pass the on-chip DC break (orange), which filters out the low frequency noise.

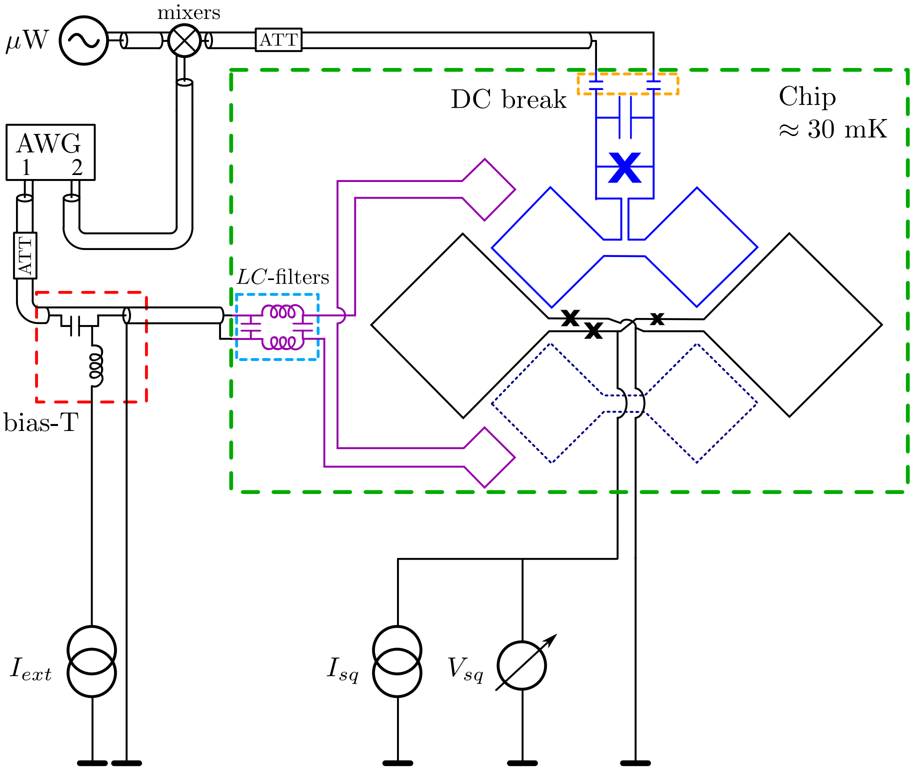

Figure 4.2: Experimental setup. The green box symbolizes the chip at a temperature of 30 mK. The qubit is controlled by microwaves, which are pulsed by using two mixers in series and the AWG, and by the extern flux bias, which is partially controlled by AWG. The readout is performed by a dc-SQUID which is connected to a current source and a voltmeter.

As discussed in Sec. 2.2.2, the potential of the qubit is controlled by applying the external flux, which results from the current I_{ext}. The second port of the AWG generates the fine tuning of the flux bias, which is responsible for the realization of the pulse sequences discussed in the following experiments, as well as the readout pulse. The flux bias signal is damped by approximately 10 dB to increase the resolution of the pulse amplitude, and then goes through a bias tee (bias-T, red), which combines the output signal of the AWG with the DC current I_{ext}. To filter out high frequency components, the chip has a series of low-pass LC-filters (light blue). After the readout pulse, the state of the qubit is measured with the dc-SQUID (black) [32].

4.1.3 Characterization of the quantum systems

Excitation spectrum

The first measurement after cooling down the chip records the excitation spectrum $f_q(\Phi_{ext})$ of the qubit (Eq. 2.11). To find the resonance frequency at a particular extern flux bias Φ_{ext} a long microwave pulse each with different frequencies is applied on the qubit. The duration of this pulse has to be much longer (in our case 500 ns) than the decoherence time of the qubit (in our case ∼100 ns) to ensure that the qubit is in the stationary limit of Rabi oscillations. The pulse sequence and the results are shown in Fig. 4.3(a) and (b). For the bias a current source and an arbitrary waveform generator (AWG) are used (Sec. 4.1.2). The current source generates a pulse to tilt the potential of the qubit to the working point, and the AWG is responsible for changing the bias in correspondence to pulse sequences of experiments.

Since the induced current in the qubit is proportional the externally applied flux Φ_{ext}, we can express the resonance frequency of the qubit f_q (Eq. 2.11) as

$$f_q = f_p \sqrt[4]{1 - \left(\frac{\Phi_{ext} - \Phi_0}{\Phi_c}\right)^2}, \tag{4.1}$$

where f_p is the plasma frequency of the qubit and Φ_c is the critical flux needed to induce the critical current of the Josephson junction I_c. Φ_0 takes account for a possible offset of the external flux. In particular, this factor plays an important role when considering the resonance frequency of the qubit only in dependence on the flux bias generated by the AWG. Then, the generated flux by the current source is carried by Φ_0. In further analysis, we will use rather the qubit frequency f_q than the externally applied flux Φ_{ext}. This is more convenient when comparing the experimental results with theoretical predictions directly.

Here, we introduce a new quantity f_{res}. In contrast to the qubit frequency f_q, f_{res} represents the real resonance of the measurement. Usually, f_q equals f_{res}. However, at some qubit frequencies f_q the spectrum splits in two parts resulting in $f_{res} \neq f_q$. These avoided level crossings (Fig. 4.3(b)) give evidence of presence of parasitic quantum systems, so called two-level-systems (TLS) (Sec. 3.2). The frequency range of interest for this thesis extends over the resonance frequencies of two TLSs shown in Fig. 4.3(c). Let us call the higher one with the resonance frequency of 7.944 GHz TLS1 and that with 7.734 GHz TLS2. The simulation (Fig. 4.3(d)) takes them into account with the decoherence times specified in Tab. (4.1). The line width of the spectrum depends on the microwave power (experiment) and so on the Rabi

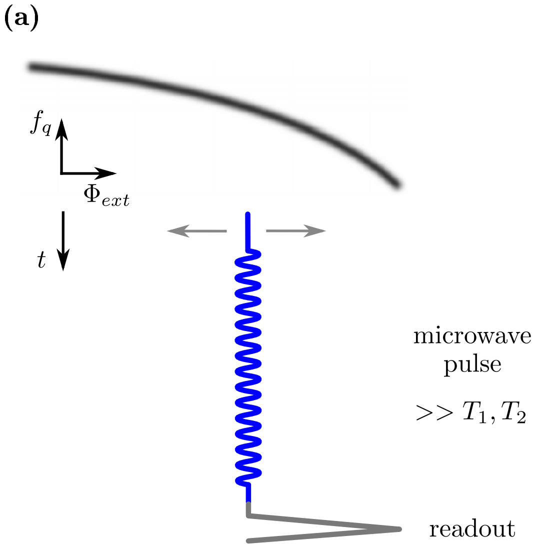

Figure 4.3: Excitation spectrum of the qubit. **(a)** Pulse sequence. The upper bleary curve symbolizes the spectrum of the qubit. At different biases (indicated by two grey arrows) long microwave pulses (500 ns) are applied on the qubit and then the readout is performed. **(b)** A very broad plot of the excitation spectrum in dependence on arbitrary units. **(c)** The region of interest with recalculated qubit frequency f_q. The level splitting at 7.944 GHz occurs due to TLS1, at 7.734 GHz due to TLS2 **(d)** The simulation of (c)

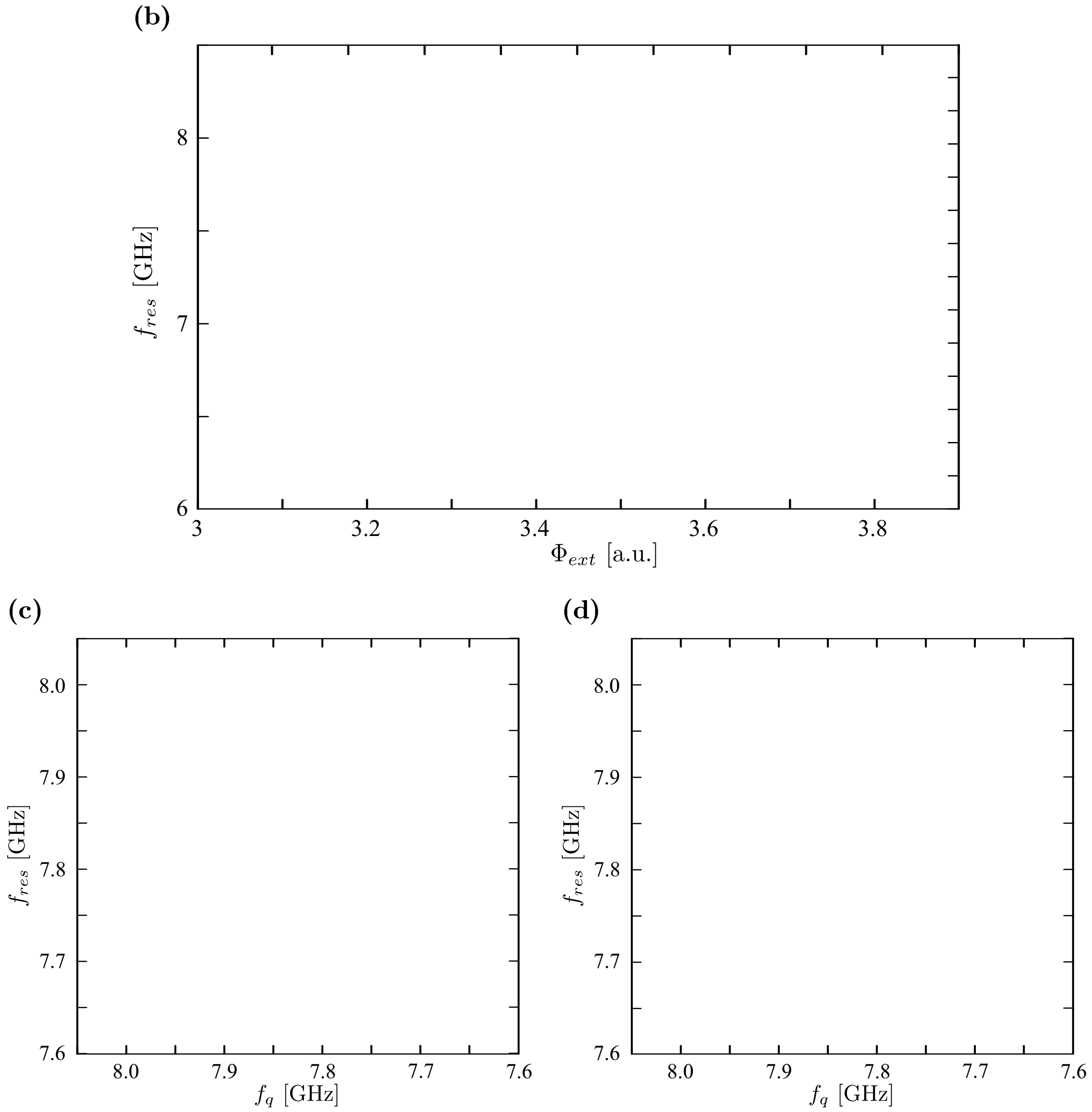

frequency (simulation). In correspondence to the measurement the Rabi frequency was determined to be 5 MHz. A measurement of beating (Sec. 3.2.2) between qubit and TLSs (Fig. 4.5) showed an additional TLS (TLS3). Its coupling is too small for the resolution of the resonance spectrum. Note the very high pure dephasing times of the TLSs of several micro seconds. The TLSs satisfy the condition of an ideal atom $T_2 \approx 2T_1$ (Eq. 3.32). Note also, that the horizontal axis in the plot in Fig. 4.3(c) is expressed in units of f_q, and therefore can be compared directly with the simulation.

	T_1 [ns]	T_2 [ns]	T_2^* [ns]	f_{res} [GHz]	g [MHz]
qubit	110	100	183		
TLS1	350	600	4200	7.944	34.8
TLS2	450	800	7200	7.734	22.5
TLS3	≈ 100	≈ 200	-	7.85	14

Table 4.1: Table with the decoherence times of the qubit and TLSs and the couplings of the TLSs with the qubit

Decoherence times of the Qubit

Once the resonances are found one can perform measurements to characterize the qubit. First, the Rabi oscillations (Sec. 3.1.4) are observed (Fig. 4.4(a)). The damping rate was measured to be 100 ns. The result from Eq. (3.62) $\tau = 105$ ns is in good agreement with the experiment. To extract the decay time T_1 (Sec. 3.1.5), the qubit is excited by π-pulse and then the readout is performed after waiting for different times t (Fig. 4.4(b)). The Ramsey experiment (Sec. 3.1.6), which consists of varying waiting times t with optional detuning between two $\pi/2$-pulses, yields the dephasing time T_2 (Fig. 4.4(c)). The pure dephasing time T_2^* is calculated with Eq. (3.32). To get reliable decoherence times they have to be measured at different flux biases because they can be drastically reduced in the vicinity of a TLS [37]. The decoherence times are collected in Tab. (4.1).

Decoherence times of TLSs

The two-level systems are characterized by performing the same experiments as for the qubit characterization (Sec. 4.1.3). It is possible to excite them directly with a microwave π-pulse. The coupling is mediated by the second excited state of the qubit [31, 4]. Although we do not have a separate readout channel for TLSs, we can determine their state by swapping it with a π-rotation on the qubit and then

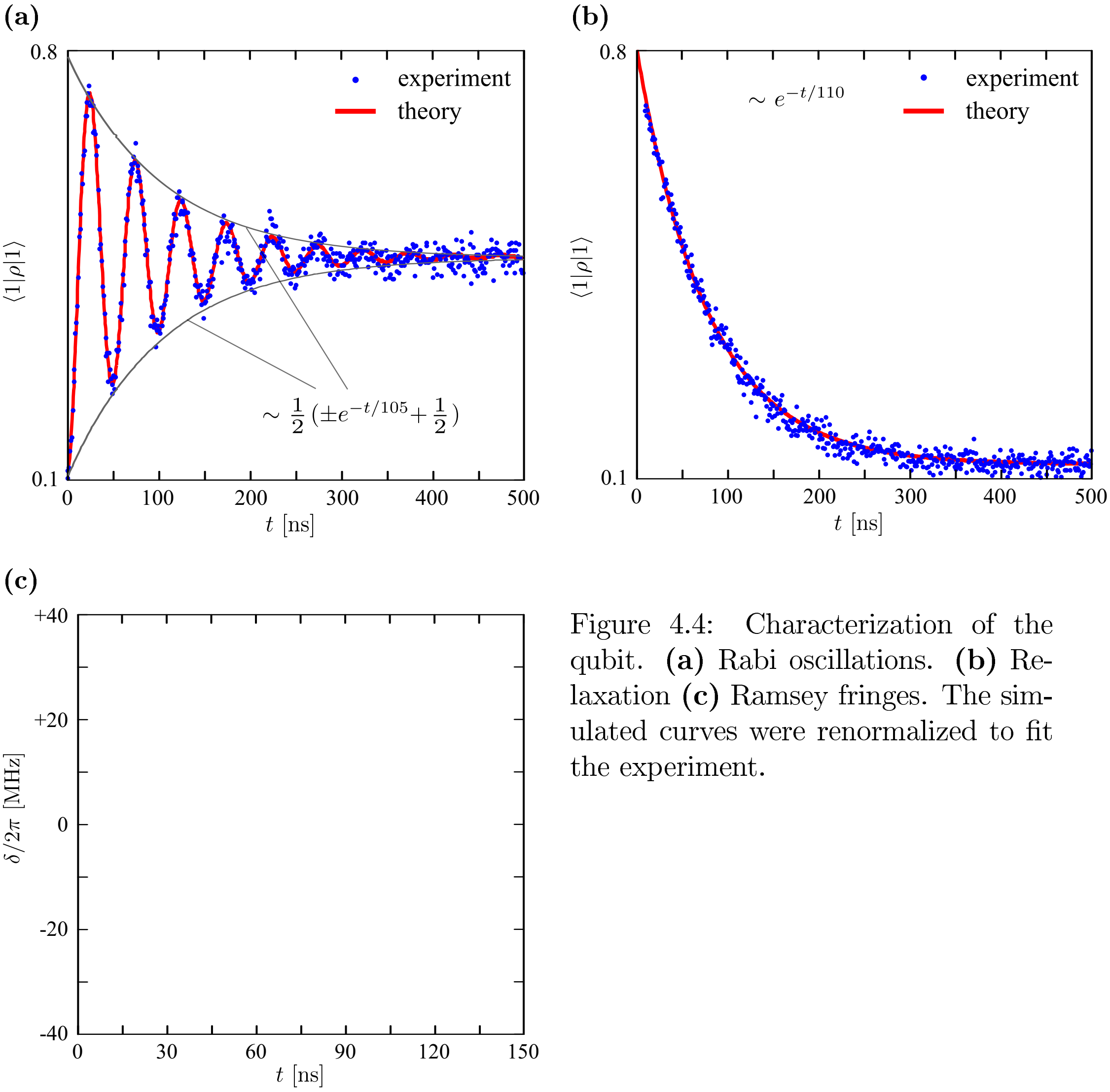

Figure 4.4: Characterization of the qubit. **(a)** Rabi oscillations. **(b)** Relaxation **(c)** Ramsey fringes. The simulated curves were renormalized to fit the experiment.

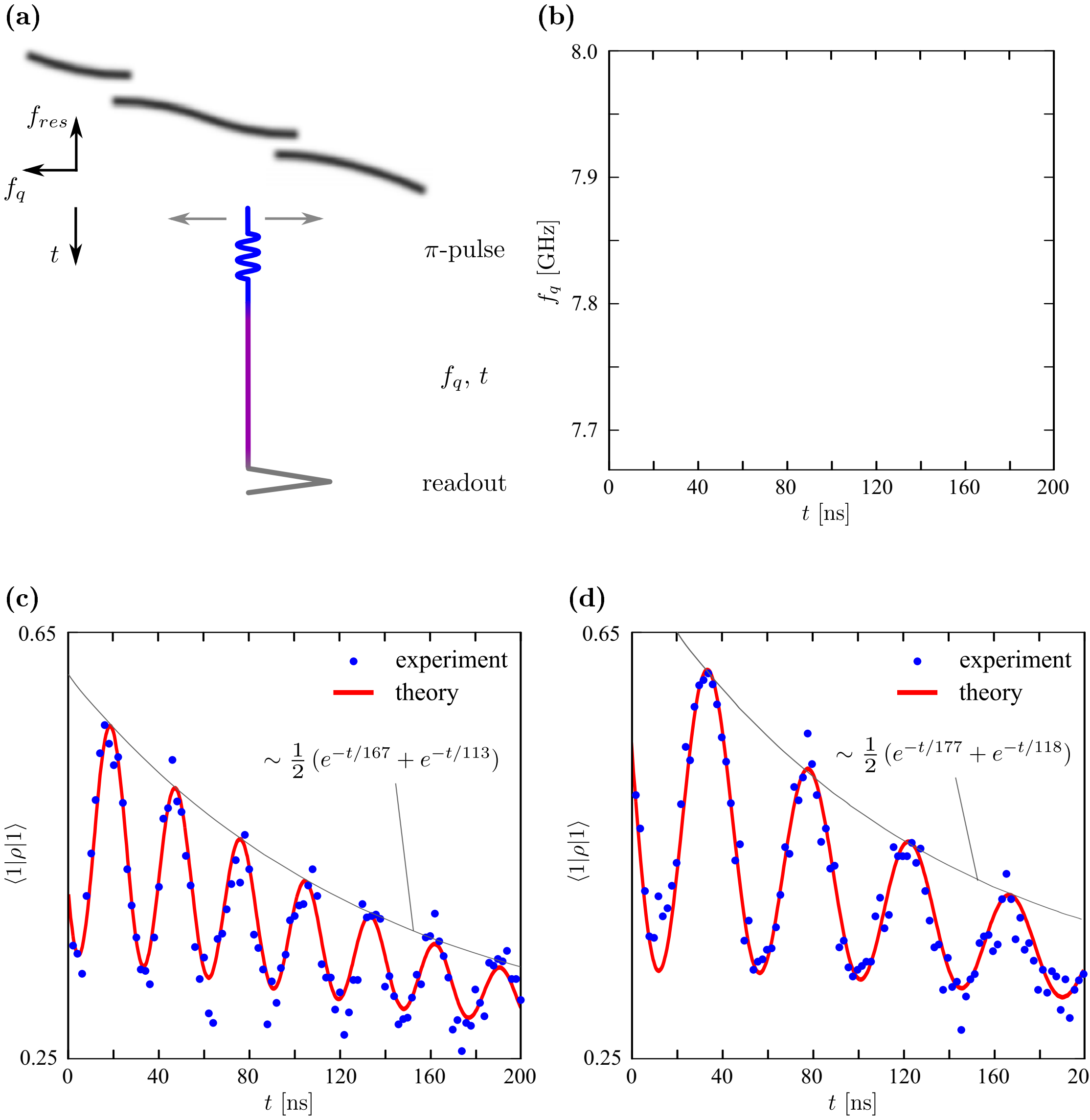

Figure 4.5: Beating. **(a)** Pulse sequence. The upper bleary line represents the resonance spectrum. f_q is the resonance frequency of the qubit. At different qubit biases (indicated by two grey arrows) the π-pulse is applied (blue), after the beating time t the readout is performed (grey). **(b)** Beatings of the excited qubit with TLS1 (7.944 GHz), TLS2 (7.734 GHz) and TLS3 (7.85 GHz). By comparing the time evolution of the oscillations at frequencies of **(c)** TLS1 and **(d)** TLS2 the coupling strengths can be determined quite precisely. The simulated curves were renormalized to fit the experiment.

performing the readout. The coupling strength g between the qubit and TLSs can be determined quite precisely by observing the beating (Sec. 3.2.2) between the two systems (Fig. 4.5). The characteristic times of the damping can be calculated by the Eqs. (3.76). The qubit is biased at different frequencies and then excited by a π-pulse. After waiting for some time t the probability of the qubit to be in the excited state is measured. The decoherence times of the three TLSs in the frequency range of interest are shown in Tab. (4.1). It was not possible to find out the characteristic times for TLS3 since they are too short in respect to the necessary time for a π-rotation.

4.2 Experiments between qubit and one TLS

4.2.1 Quantum state tomography and preparation of an arbitrary state

When considering experiments in the quantum limit, particularly the field of quantum computation [43], it gets very important to characterize the state of the coherent quantum system. This is done by finding the corresponding density matrix, which in turn can be reconstructed by performing quantum state tomography [39]. A measurement of a quantum system projects the state to its eigenstates. It yields no information about coherence between these eigenstates which is described by the off-diagonal entries of the density matrix (Sec. 3.1.3). The term quantum tomography implies a controlled rotation of the quantum system so that effectively another eigenbasis is created. By preparing the initial state many times and measuring the projection to different eigenstates a full description of the initial state can be recalculated. Usually, the initial eigenbasis is referred to as the z-axis. The rotations of the state are made in such way so that the state is projected on the x- or y-axis. This results in the Bloch sphere and the Bloch vector discussed in Sec. (3.1.1).

The first quantum tomography in an experiment was realized in the field of quantum optics by D'Arino *et al.* in 1995 [13]. Nowadays, it is a common technique. In the field of superconducting qubits for example, since the year 2006 almost every paper presenting some experiments shows also tomography results [50]. In that field, qubits are controlled by microwaves. As discussed in the section about Rabi oscillations (Sec. 3.1.4), the Bloch vector of the qubit starts to oscillate in presence of a resonant microwave field passing from the ground state to the excited state. The corresponding coupling strength is defined as a real number so that the x-axis is the rotation axis. By performing this rotation the projection of the Bloch vector to the y-axis can be realized. To have also the expectation value in respect to the x-axis, the coupling strength between the ground and the excited state is made purely imaginary. This can be arranged by a $\pi/2$-phase shift of the microwave signal, e.g. by using an IQ-mixer [50]. By "reversing" the quantum tomography also the preparation of an arbitrary state becomes possible.

The main idea of the quantum tomography to have control of the Bloch vector can be also realized in a different way. We can take advantage of the parasitic, but also coherent two-level systems (TLS) coupled to our qubit. The formalism for this approach is straight forward. The two states of the qubit are denoted as $\{|1\rangle, |0\rangle\}$ and that of the TLS as $\{|e\rangle, |g\rangle\}$. Together, they span a 4-dimensional product space

$\{|1\rangle, |0\rangle\} \otimes \{|e\rangle, |g\rangle\}$. At the beginning of each experiment, the qubit is detuned from the TLS and the microwave source is used to excite the qubit with a π-pulse. This is the only function of the microwaves in the experiment presented here. The state $|1e\rangle$ has two excitations and therefore does not play a role. In contrast, due to energy relaxation the probability to find the whole system in the ground state $|0g\rangle$ is increasing with time. However, it does not affect the dynamics of the system. $|0g\rangle$ it is an eigenstate which is not coupled to other states and will therefore not participate in any rotations. Thus, we can concentrate only on the two states $|1g\rangle$ and $|0e\rangle$.

To be able to use the Bloch sphere and the equations discussed in Sec. (3.1.1), we have to redefine the states. The states $|1\rangle$ and $|0\rangle$ are replaced by the states $|1g\rangle$ and $|0e\rangle$, respectively. The corresponding states on the x- and y-axis then can be rewritten as

$$|\pm\rangle^{qs} = \frac{|0e\rangle \pm |1g\rangle}{\sqrt{2}}, \; |\pm_i\rangle^{qs} = \frac{|0e\rangle \pm i|1g\rangle}{\sqrt{2}}, \tag{4.2}$$

where the superscript letters qs denote the states of hybrid system qubit-TLS.

Note here two remarks. First, the ground state is not represented on the Bloch sphere. The relaxation of the system can be modeled by a shortening of the Bloch vector to the origin of the Bloch sphere with time. Thus, it affects only the contrast of the measurement. Secondly, here it is not necessary that the state $|1g\rangle$ is energetically higher than the state $|0e\rangle$, it depends on the relative position of the qubit in respect to the TLS. By taking this into account, we can transfer the considerations of rotation described in Sec. (3.1.2) to this case. Thus, as it is also the case of Rabi oscillations, the x-axis stays the rotation axis at resonance.

It is important to point out the main differences between the manipulation of the Bloch vector by microwaves and by coherent interaction with a TLS. First, the preparation of an arbitrary state by using a TLS can be only done, if either the TLS or the qubit are excited (in our case it is the qubit). Second, as mentioned above, the rotation around the y-axis in the case where microwaves are used is achieved by a phase shift of $\pi/2$ of the microwave signal. An equivalent but less obvious explanation therefor would be that the Bloch vector at some time point suddenly acquires an additional phase of $\pi/2$ and the x-axis persists the rotation axis. That is, indeed, the idea when considering a rotation with a TLS. That happens when detuning the qubit from the TLS by the angular frequency δ for the time $\pi/2\delta$. Note that δ has to exceed the coupling strength between qubit and TLS by at least a factor of 15 [1]. Third, we have to compare the main features of Rabi oscillations (Sec. 3.1.4) and beating (Sec. 3.2.2). A driven qubit will never be in an eigenstate. Starting with the state $|0, n\rangle$, where n denotes the photon number of the microwave field, it will oscillate between $|0, n\rangle$ and $|1, n-1\rangle$. When the qubit decays, it will continue to interact with the microwave field rotating from $|0, n-1\rangle$ to $|1, n-2\rangle$ etc. In the limit of long times the qubit will pass into a steady state. When considering the hybrid system qubit-TLS the energy oscillates between the states $|1g\rangle$ and $|0e\rangle$. Here, the process ends in the eigenstate $|0g\rangle$. Fortunately, our TLSs have much longer decoherence times than the qubit, so that the damping rate for these oscillations in resonance is even slightly lower than that for Rabi oscillations. The last point concerns the quantum tomography itself. By performing Rabi oscillations either around the x-axis or y-axis the population and phase of the state $|1\rangle$ in respect to the state $|0\rangle$ can be determined. In contrast, if the state of the qubit is manipulated with the TLS, only the relation of the state $|1g\rangle$ in respect to the state $|0e\rangle$ is reproduced. It yields no information between the states $|1g\rangle$ and $|0g\rangle$.

4.2.2 Generation of $|\pm\rangle^{qs}$ states with two rotations

Let us now prove the ability to prepare arbitrary states of the qubit and then perform a tomography. The most interesting area on the Bloch sphere is the equatorial plane. There are all the states defined in Eq. (4.2) which will yield maximal oscillations ($|\pm_i\rangle^{qs}$) or no oscillations at all ($|\pm\rangle^{qs}$) when the qubit is in resonance with the TLS.

The desired time evolution of the Bloch vector is shown in Fig. 4.6(a),(b). The pulse sequence to realize this controlled rotations is displayed in Fig. 4.6(c). First, the qubit is placed to the microwave frequency of 7.569 GHz. This corresponds to a detuning of 165 MHz from TLS2. Then it is excited with a π-pulse which has a duration of 20 ns (blue) and is tuned into resonance with TLS2. There it is kept for 11 ns which results in a $\pi/2$-rotation (green). Afterwards, the qubit is detuned again by 165 MHz for the time t_1 (orange) and brought back to resonance. After the beating time t_2 (purple) the readout is performed (grey).

In the following these rotations are analyzed analytically. After the π-pulse generated by the microwave field the hybrid system qubit-TLS2 is in the state $|1g\rangle$ which is lying on top of the Bloch sphere (blue thin arrow) (Fig. 4.6). Thus, the starting condition is

$$|\psi_0\rangle = |1g\rangle = \begin{pmatrix} 1 \\ 0 \end{pmatrix}. \tag{4.3}$$

The qubit then is brought into resonance with the TLS and the Bloch vector starts to oscillate around the axis defined by the eigenstates $|\pm\rangle^{qs}$ (Fig. 4.6(a)). The direction of rotation is determined by the fact that the energy of $|+\rangle^{qs}$ is higher

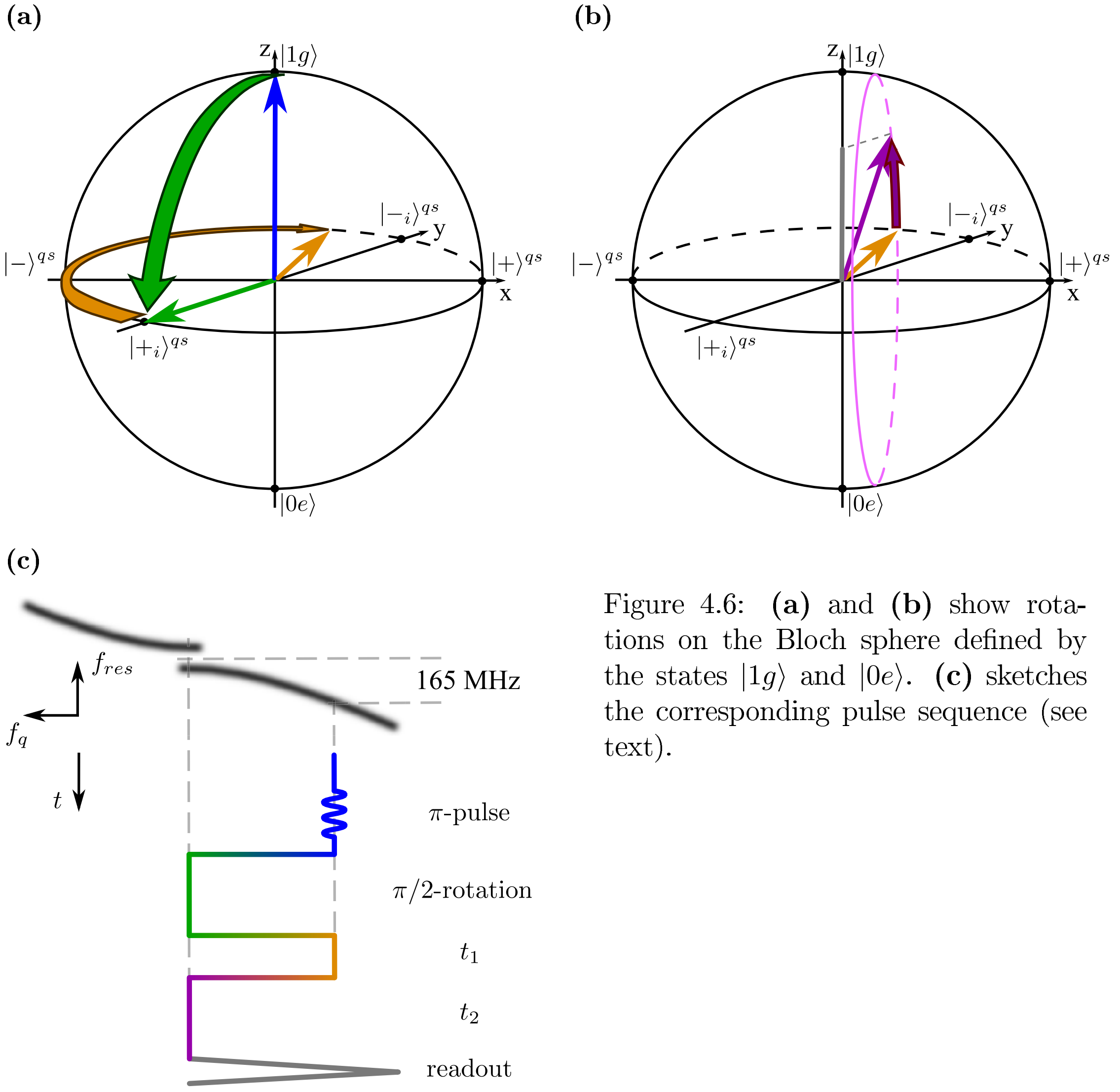

Figure 4.6: **(a)** and **(b)** show rotations on the Bloch sphere defined by the states $|1g\rangle$ and $|0e\rangle$. **(c)** sketches the corresponding pulse sequence (see text).

than that of $|-\rangle^{qs}$. By using the right hand rule (Sec. 3.1.2) the Bloch vector rotates into direction of the state $|+_i\rangle^{qs}$. The duration of this rotation is fixed so that this step is finished when the Bloch vector reaches the state $|+_i\rangle^{qs}$ (green thin arrow) which corresponds to a $\pi/2$-rotation. The unitary matrix which describes this entanglement can be found by using Eq. (3.16), where $\alpha = 90°$ and $\beta = 0°$ (Eq. 3.10) correspond to the angles of the eigenstate $|+\rangle^{qs}$. The angle by which the Bloch vector is rotated is $\pi/2$, and so

$$U_0 = \frac{1}{\sqrt{2}} \begin{pmatrix} 1 & -i \\ -i & 1 \end{pmatrix}. \tag{4.4}$$

Since this experiment was made with TLS2 and the coupling strength is $g_2/h = 23$ MHz the time for rotation is fixed to 11 ns. Afterwards the qubit is brought back

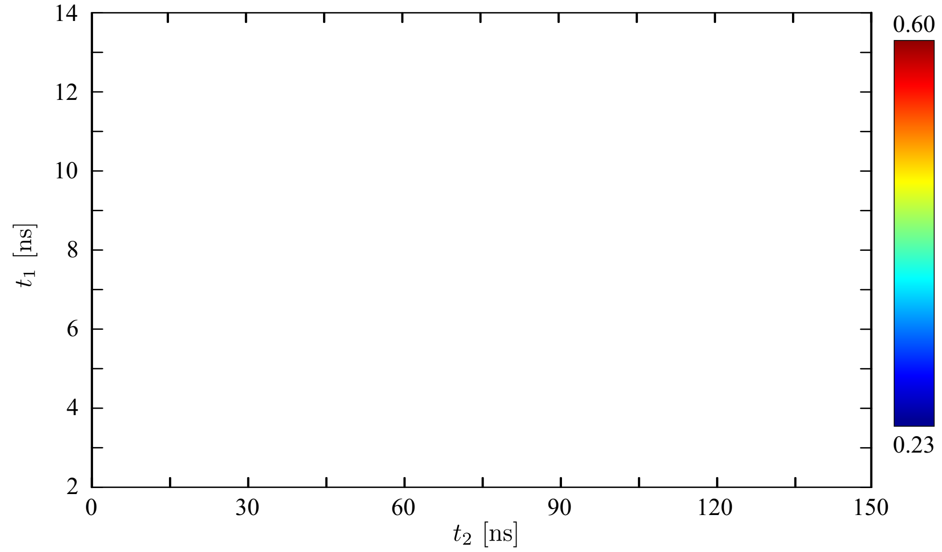

Figure 4.7: Measurement of the pulse sequence shown in Fig. 4.6. The Bloch vector oscillates on the equatorial plane around the z-axis for the time t_1. Then it rotates around the x-axis for the time t_2. The disappearance of oscillations at the times t_1 of 4.5 ns, 7.5 ns etc. determine the Bloch vector to point to the states $|+\rangle^{qs}$, $|-\rangle^{qs}$, etc.

to the initial position. Here it is parked for the time t_1. The detuning between the qubit and TLS2 equals $\delta/2\pi = 165$ MHz. The Hamiltonian for this configuration is

$$H_1 = \begin{pmatrix} -\hbar\delta & g_2/2 \\ g_2/2 & 0 \end{pmatrix}. \tag{4.5}$$

The energy is negative indicating that the resonance frequency of the qubit is below that of TLS2. Therefore, the Bloch vector starts to rotate nearly around the z-axis clockwise. We find the oscillating frequency $\omega_1/2\pi$ (Eq. 3.15) and the angles α and β (Eq. 3.10) describing the location of the eigenstates on the Bloch sphere to be

$$\frac{\omega_1}{2\pi} \approx 167 \text{ MHz } \approx \frac{1}{6 \text{ ns}} \text{ and} \tag{4.6}$$

$$\alpha \approx 8°,\ \beta = 0. \tag{4.7}$$

The unitary time evolution operator (Eq. 3.16) then can be written as

$$U_1(t_1) \approx \begin{pmatrix} e^{i\frac{\omega_1}{2}t_1} & -i\alpha\sin\frac{\omega_1}{2}t_1 \\ -i\alpha\sin\frac{\omega_1}{2}t_1 & e^{-i\frac{\omega_1}{2}t_1} \end{pmatrix}. \tag{4.8}$$

For an ideal rotation around the z-axis α has to be zero. Unfortunately, this is not the case here. The reason is that the qubit is not detuned far enough. The ratio $\hbar\delta/g_2$ is approximately 7. In the paper of Hofheinz *et al.* [21] it is proposed to detune 25 times the coupling which corresponds to an α of 2°. In our case the detuning would be equal to 575 MHz. The problem with such a high detuning is that the rotations around the z-axis are too fast. The time for one cycle would be less than 2 ns. To smooth the shape of the pulses and to remove parasitic oscillations, the lowpass filter at the output port of our AWG (arbitrary waveform generator) was set to 200 MHz. This results in rising and falling times each of around 1 ns, which corresponds already to a half of rotation.

As explained above, the period of the oscillations is 6 ns. Thus, starting with $|+_i\rangle^{qs}$, the state of the system will first pass $|-\rangle^{qs}$ after approximately 1.5 ns. After 4.5 ns it will reach the state $|+\rangle^{qs}$ and after 7.5 ns it will come again to $|-\rangle^{qs}$ (Fig. 4.6(a)).

In the next step, the qubit is brought into resonance with TLS2 for the time t_2. The corresponding Hamiltonian and the time evolution operator ($\alpha = 90°,\ \beta = 0°$) then are

$$H_2 = \begin{pmatrix} 0 & g_2/2 \\ g_2/2 & 0 \end{pmatrix} \tag{4.9}$$

and

$$U_2(t_2) = \begin{pmatrix} \cos\frac{\omega_2}{2}t_2 & -i\sin\frac{\omega_2}{2}t_2 \\ -i\sin\frac{\omega_2}{2}t_2 & \cos\frac{\omega_2}{2}t_2 \end{pmatrix}, \tag{4.10}$$

where $\omega_2 = g_2/\hbar$. Afterwards, the pulse sequence is terminated by the readout. The probability to measure the qubit in the excited state after that sequence is given by

$$\mathcal{P}(t_1, t_2) = |\langle\psi_0|U_2(t_2)U_1(t_1)U_0|\psi_0\rangle|^2. \tag{4.11}$$

If we assume α to be zero we can find an analytical expression in the form

$$\mathcal{P}_{\alpha=0}(t_1, t_2) = \frac{1}{2}\left(1 - \cos(\omega_1 t_1)\cos\left(\omega_2 t_2 + \frac{3\pi}{2}\right)\right). \tag{4.12}$$

The measurement is shown in Fig. 4.7 versus times t_1 and t_2. Due to the duration of the rising and falling times of the pulses of 1 ns, t_1 and t_2 start with 2 ns. The oscillations at a fixed time t_1 visualize the beating between the states $|1g\rangle$ and $|0e\rangle$ indicating a rotation of the Bloch vector around the x-axis. Thus, maximal beating arises at t_1 of 0 ns ($|+_i\rangle^{qs}$, not shown), 3 ns ($|-_i\rangle^{qs}$), 6 ns ($|+_i\rangle^{qs}$) etc. In contrast, the oscillations vanish when the system is in its eigenstates, so at 1.5 ns ($|-\rangle^{qs}$, not shown), 4.5 ns ($|+\rangle^{qs}$), 7.5 ns ($|-\rangle^{qs}$) etc.

The theoretical results one can see in Fig. 4.8. The surface plot with a qubit detuned by 575 MHz from TLS2 as a comparison is shown in Fig. 4.8(a). The

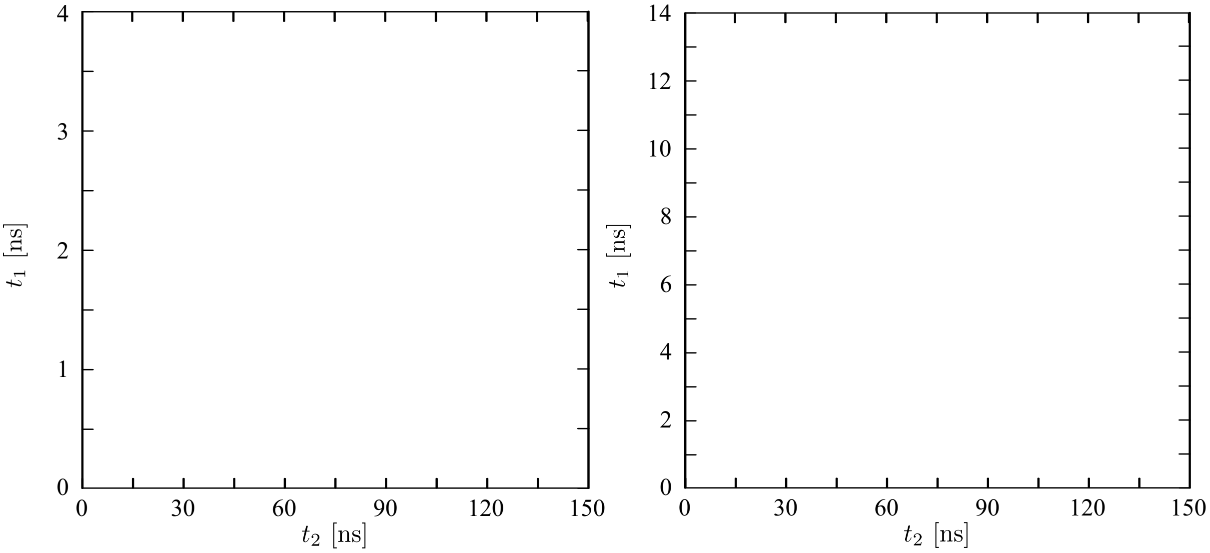

(a) $\delta/2\pi = 575$ MHz **(b)** $\delta/2\pi = 165$ MHz

(c) $\delta/2\pi = 165$ MHz, qubit missed the resonance by $+4$ MHz

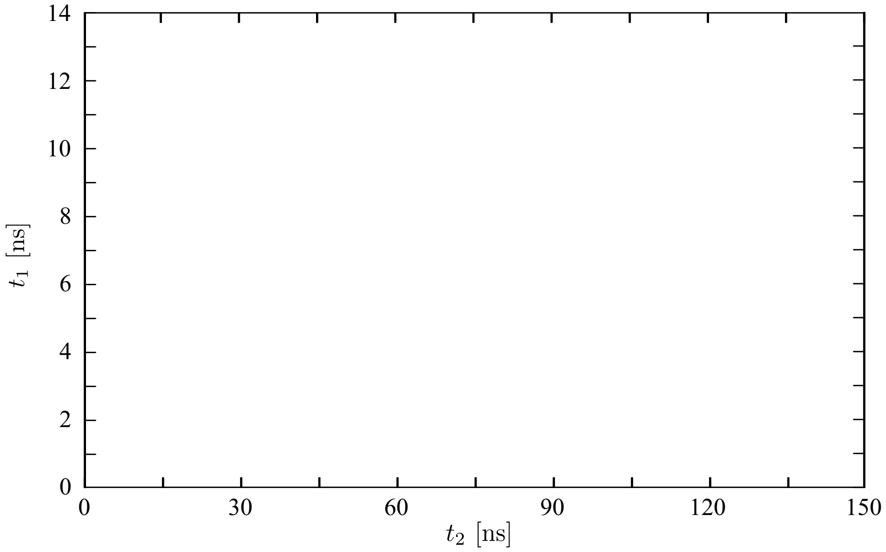

Figure 4.8: Simulation of the pulse sequence shown in Fig. 4.6. Qubit detuned by 575 MHz **(a)**, 165 MHz **(b)** from TLS2 while exciting and while the rotations during t_1. **(c)** Qubit detuned by 165 MHz for the time t_1 and by $+4$MHz for the time t_2

real situation with $\delta/2\pi = 165$ MHz is displayed in Fig. 4.8(b). Here, one can recognize that the chess board structure turns into a diamond shape. However, the experimental results show rather a chess board than diamonds. An obvious reason for this disagreement is an error in calibration of the experiment. The variation of the corresponding times for the π-pulse or the $\pi/2$-rotation in the theory does not improve the similarity between simulation and experiment. Since the AWG has a time resolution of 0.2 ns large errors on the time axis are rather implausibly. On the other hand, the uncertainty in frequency of the qubit is quite large. The pulse for tuning and detuning the qubit generated by the AWG has an amplitude of 50 mV with a resolution of 2 mV. This results in a step size of 7 MHz. Indeed, when considering the qubit biased 4 MHz above TLS2 during the time t_2, the chess board shape is reproduced (Fig. 4.8(c)).

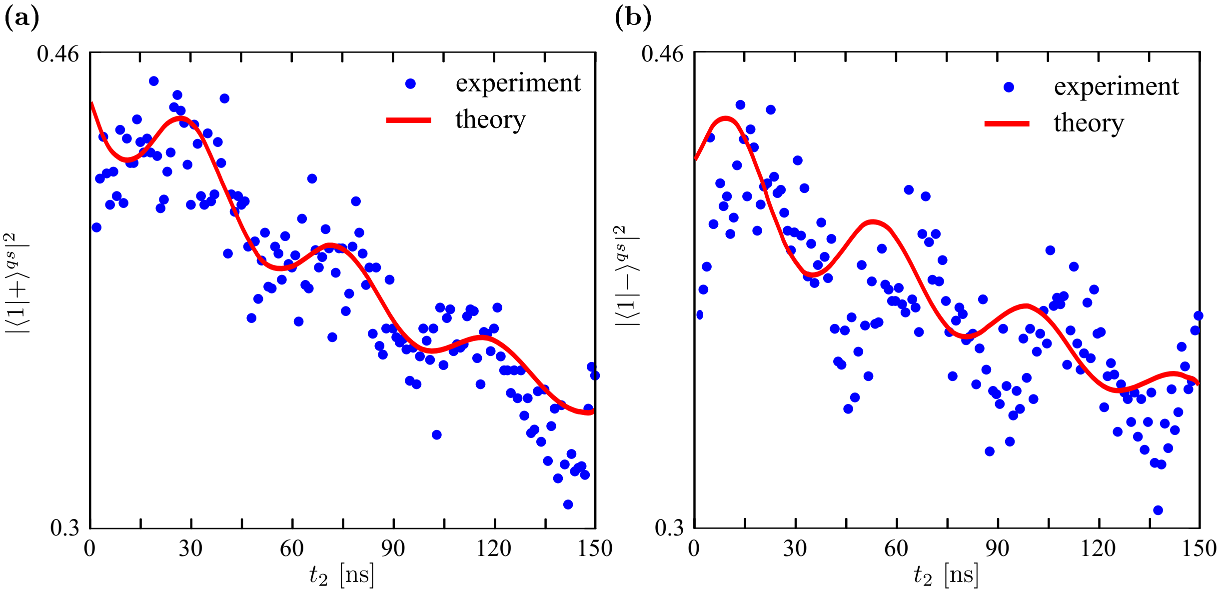

Figure 4.9: Decay of the $|\pm\rangle^{qs}$ states. Cut from the surface plot in Fig. 4.8 at **(a)** $t_1 = 4.6$ ns ($|+\rangle^{qs}$) and **(b)** $t_1 = 7.6$ ns ($|-\rangle^{qs}$)

The behaviour of the decay of the state $|+\rangle^{qs}$ is shown in Fig. 4.9(a). One can see its exponential dependence on time. However, the curve still possesses oscillations. The theory is in good agreement with the experiment confirming the idea described above. In contrast, the fit of the state $|-\rangle^{qs}$ (Fig. 4.9(a)) is shifted to the left by 7 ns. I have not found any explanation for a so large offset. Even considering other fitting parameters like longitudinal coupling between the TLS and qubit do not improve the fit. Taking into account TLS3 (Sec. 4.1.3) with a resonance frequency of 116 MHz above TLS2 also does not make the agreement better.

Here, I want to resume the idea of tomography. At the time $t_1 = 4.5$ ns Fig. 4.7 does not show significant oscillations indicating that the Bloch vector is in an eigenstate of the qubit-TLS2 system in resonance. In contrast, at the time $t_1 = 6$ ns, which corresponds to a phase difference of $\pi/2$, maximal oscillations appear. For times t_2 close to zero the probability to find the qubit in the excited states rather goes down than up. This is the result of the tomography of the state $|+\rangle^{qs}$. Another rather simple example is the state $|0e\rangle + e^{-i\varphi}|1g\rangle$ with $\varphi = 135°$. On the Bloch sphere this state is located on the equatorial plane between the states $|-\rangle^{qs}$ and $|-_i\rangle^{qs}$. Starting the time evolution of the Bloch vector from $|+_i\rangle^{qs}$, this state is created after $t_1 = 2.25$ ns, and thus the $\pi/2$-rotation is terminated after 3.75 ns. The two oscillating curves show the same behavior. In principle, one can extend this type of tomography to the whole Bloch sphere.

4.2.3 Generation of $|\pm\rangle^{qs}$ states with one rotation

As we have discussed in the previous section, we have prepared states between qubit and TLS2 with two rotations of the Bloch vector which are close to eigenstates of the hybrid system qubit-TLS2 in resonance. When observing the decay of these states (Fig. 4.9) the Bloch vector shows small oscillations. We found that a possible reason for that is a not precise calibration. A question arises whether it is possible to prepare these states more accurately with an easier approach and eventually faster.

The answer is yes. We can do it by rotating the Bloch vector only once from the state $|1g\rangle$ directly to the desired states $|\pm\rangle^{qs}$, as shown in Fig. 4.10. The evolution of the Bloch vector on the Bloch sphere and the corresponding pulse sequence is displayed in Fig. 4.10 (a) and (b).

First, like in the experiment with two rotations, we excite the qubit with a π-pulse detuned from TLS2 by $\delta/2\pi = 165$ MHz (blue). To prove the $|\pm\rangle^{qs}$-creation, again the beating is observed by tuning the qubit into resonance with TLS2 for a varying time t (purple). The second degree of freedom was chosen to be the qubit-TLS2 detuning because it is much easier to calculate the pulse time than to calibrate the flux bias of the qubit to a particular energy. Fig. 4.10(c) shows the dependence of the angle α between the rotation axis and the z-axis (Eq. 3.10) and the rotation angular frequency ω (Eq. 3.15). The energy of interest which corresponds to an α of 45° (135°) is detuned from the resonance with TLS2 by $-g_2/h$ $(+g_2/h)$. The time for a half rotation is then reduced by a factor $\sqrt{2}$ to 15.6 ns.

Fig. 4.11(a) presents the simulation for the experiment in an ideal situation. When the qubit is parked far below TLS2 for that fixed rotation α is very small. That means on one hand that the rotating axis is close to the z-axis and on the other

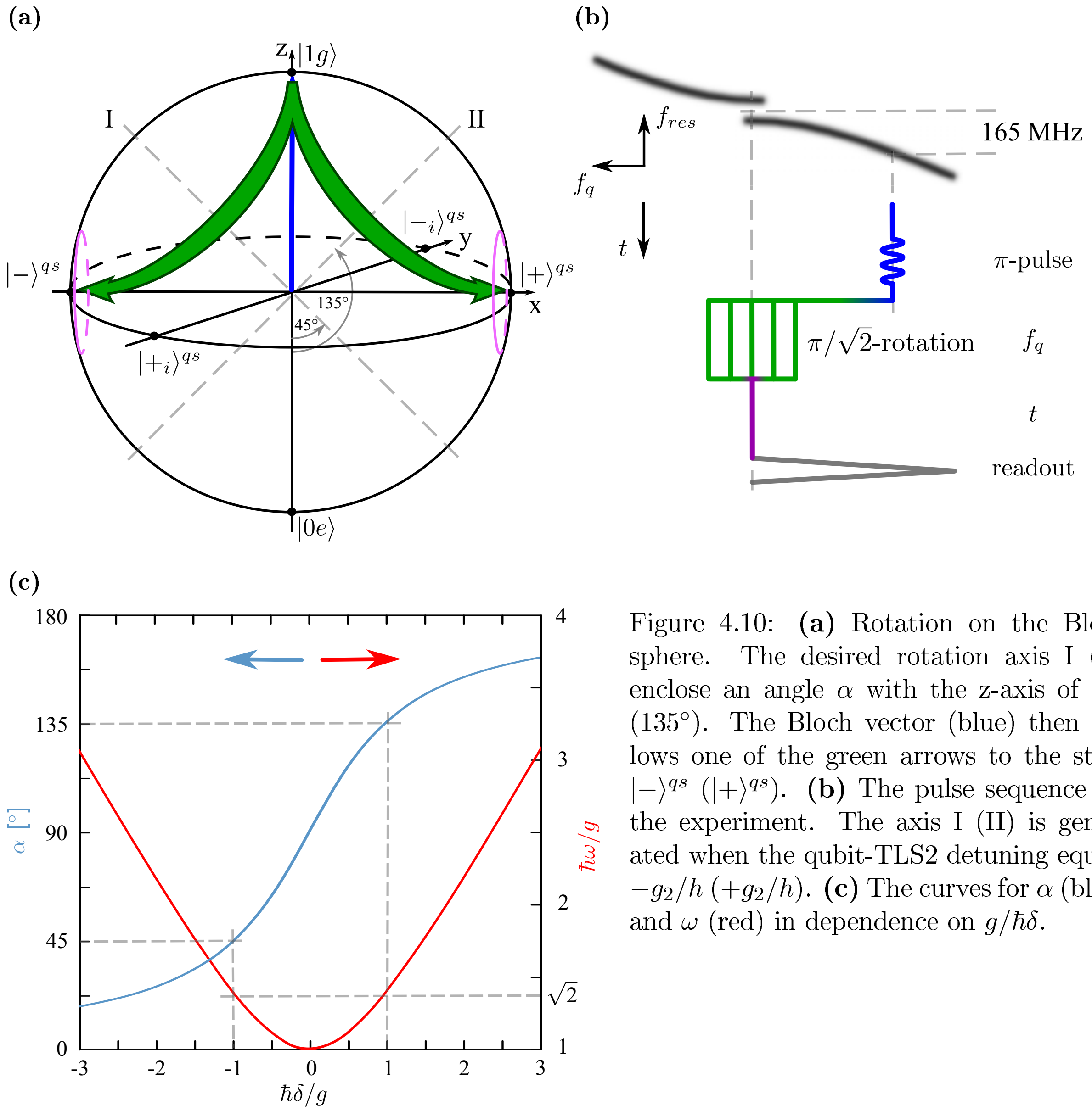

Figure 4.10: **(a)** Rotation on the Bloch sphere. The desired rotation axis I (II) enclose an angle α with the z-axis of 45° (135°). The Bloch vector (blue) then follows one of the green arrows to the state $|-\rangle^{qs}$ ($|+\rangle^{qs}$). **(b)** The pulse sequence for the experiment. The axis I (II) is generated when the qubit-TLS2 detuning equals $-g_2/h$ ($+g_2/h$). **(c)** The curves for α (blue) and ω (red) in dependence on $g/\hbar\delta$.

hand that the Bloch vector will oscillate rather on the $|-\rangle^{qs}$ side of the Bloch sphere than on the $|+\rangle^{qs}$ side. While moving towards resonance, α increases. While α is less than 45° the probability to measure the qubit in the excited state at beating times t close to zero is rather high. The reason is that the Bloch vector evaluates only in the upper half of the Bloch sphere. When α equals 45° the qubit is below TLS2 with a detuning of exactly g_2/h. Thus, when the qubit is tuned into resonance with TLS2 the Bloch vector points to the state $|-\rangle^{qs}$ and the oscillations in time t vanish. In the range of $45° < \alpha < 135°$ after the first rotation the Bloch vector points below the equatorial plane. This results in a low probability that the qubit is in the excited state for very small t. Thus, the oscillations are shifted by π in comparison

Figure 4.11: Theory and measurements. **(a)** Surface plot of an ideal situation described in Fig. 4.10. **(b)** Measurement **(c)** Theoretical plot with the following modifications: at 7.85 GHz TLS3 has its resonance frequency, qubit-TLS2 detuning during π-pulse equals 165 MHz, when the beating is observed the qubit is still detuned by -4 MHz from TLS2.

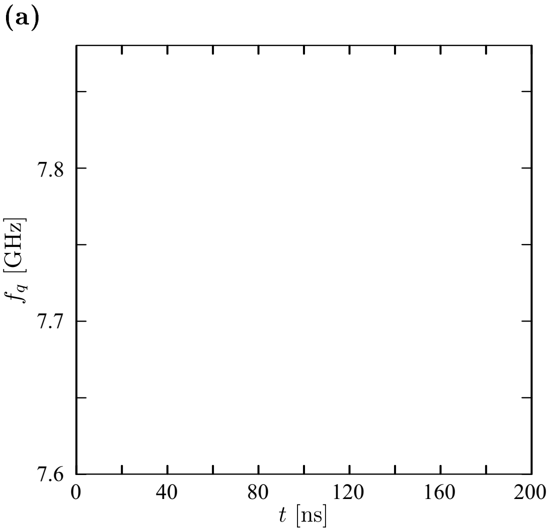

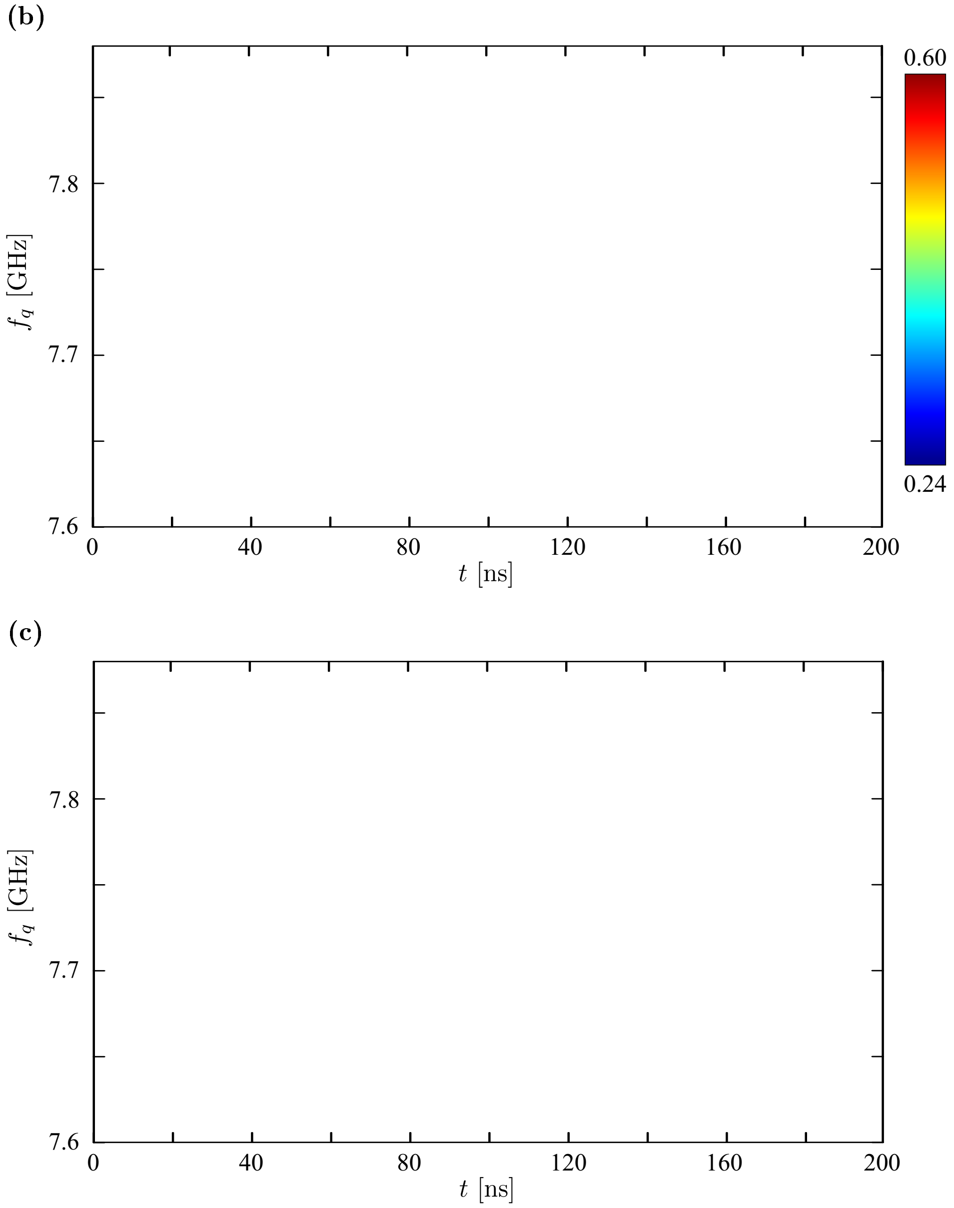

to the previous case. When α reaches 135° the Bloch vector will be rotated to $|+\rangle^{qs}$ which is again an eigenstate of the qubit-TLS2 system in resonance. This is the case when the qubit is detuned by $+g_2/h$. The evolution of the Bloch vector at higher detunings can be treated in the same way as detuning towards lower energy, but here the Bloch vector will rather oscillate on the side of positive x-axis than on the side of negative x-axis.

In Fig. 4.11(a) one can also notice small oscillations depending on detuning frequency f_q. Since the oscillation frequency changes but the rotation time is fixed, the Bloch vector will point to different states when the qubit is tuned in resonance with TLS2. If for example the Bloch vector is on the $|+_i\rangle^{qs}$ side of the Bloch sphere, first the probability of the state $|1g\rangle$ will decrease when the qubit is moved to the resonance. In contrast, the Bloch vector will first move up if when during the change of the qubit bias it points to states behind the xz-plane.

In Fig. 4.11(b) and (c) one can see the measurement as well as the corresponding theoretical plot. The experiment differs from the "ideal situation" in the following points. First, the interruption of the oscillations at 7.85 GHz occurs due to the presence of TLS3 (Sec. 4.1.3) which has its resonance frequency about 116 MHz above TLS2. Second, the oscillations depending on detuning frequency above the resonance are faster than these below the resonance. The reason for that, as the simulation shows, is that the qubit is placed too close to TLS2 during the π-pulse. Third, as discussed in the experiment with two rotations, the resolution in f_q is approximately 7 MHz. The discrepancy between the experiment and simulation is improved when assuming that even at the resonance condition the qubit is detuned from TLS2 by -4 MHz.

By changing some experimental parameters we managed to prepare the states $|\pm\rangle^{qs}$ and to measure their exponential decay (Fig. 4.12). Both states show same decay characteristic times of approximately 100 ns. Nevertheless, the relaxation of the state $|+\rangle^{qs}$ possesses still oscillations which can be explained with the presence of TLS3. To measure that exponential decay we reduced the step in f_q to 2 MHz by adding attenuators at the AWG port. Furthermore, during the π-pulse, the qubit was detuned by 400 MHz from TLS2. To correct the calibration errors we variated each quantity around its calculated values. Thus, the optimal time for rotation, and qubit bias during the rotation and at resonance with TLS2 could be found.

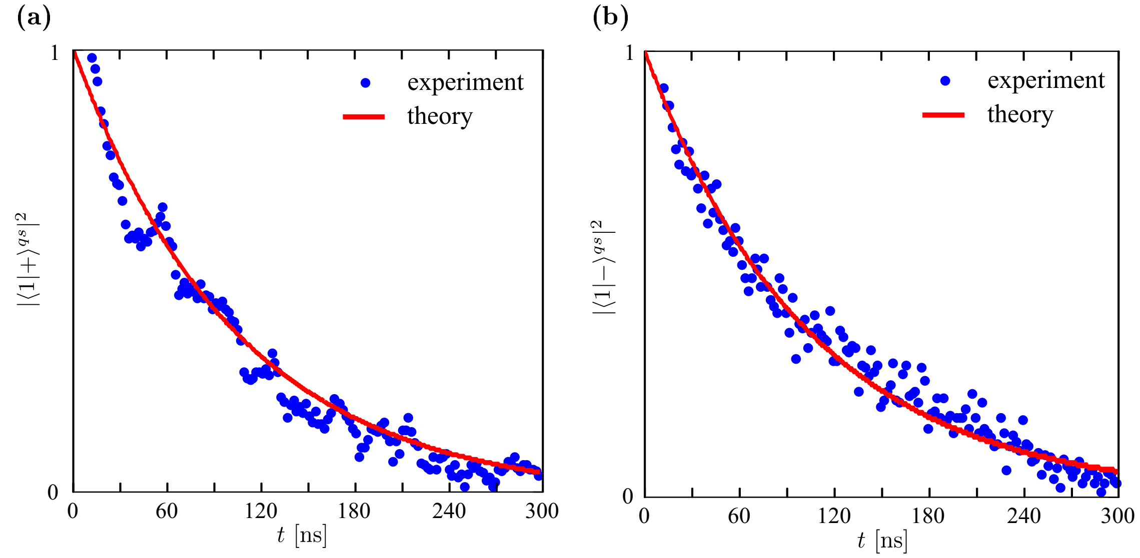

Figure 4.12: Decay of the states $|+\rangle^{qs}$ **(a)** and $|-\rangle^{qs}$ **(b)**. Both measurements show the same characteristic time of 100 ns. The decay of the state $|+\rangle^{qs}$ possesses still small oscillations due to presence of TLS3.

4.3 Experiments between qubit and two TLSs

4.3.1 Entanglement of quantum systems

Entanglement between two and more qubits is a crucial feature in quantum algorithms. The development of a computer based on quantum manipulation requires the proof of entanglement between qubits. Therefore, one has to measure the density matrix of the whole system. As discussed in Sec. (3.1.3), the diagonal elements of the density matrix give the probabilities about the states, whereas the off-diagonal elements yield the information about coherence. The latter necessitates a simultaneous readout of the quantum subsystems, i.e. the probabilities of all qubits have to be measured independently after each experiment. In this way, one can verify entanglement by performing tomography on the qubits before the readout [49] or by showing the violation of Bell's inequality [9, 1]. In our experiment, a tripartite system is composed of the subsystems phase qubit and two TLSs. The qubit is the only subsystem whose state can be determined by measurements. Thus, it is impossible to readout the states of the qubit and TLSs simultaneously. The TLSs can be measured by performing a π-rotation with the qubit (Sec. 3.2.2) followed by the readout. This results, however, in the loss of information of the former state of the qubit.

4.3.2 Coherent dynamics between two TLSs

Another way to reveal the evidence of entanglement is to observe coherent interaction between the quantum systems [1]. For example, the experiment where the states $|\pm\rangle^{qs}$ are prepared with two rotations (Sec. 4.2.2) illustrates such a measurement. The excited qubit performs a $\pi/2$-rotation with the TLS resulting in an entanglement. Afterwards, the qubit is detuned for some time and then brought again in resonance with the TLS. We observe constructive and destructive interferences. When the phase between the qubit and the TLS is zero or π ($|\pm\rangle^{qs}$) the experiment does not show oscillations. In contrast, a phase of $\pm\pi/2$ ($|\pm_i\rangle^{qs}$) possesses maximal beating. In the following, I describe an experiment which proves coherent quantum dynamics between two TLSs.

The pulse sequence for the experiment is demonstrated in Fig. (4.13). As in the previous experiments between qubit and one TLS (Sec. 4.2), it starts by a π-pulse on the qubit at 7.569 GHz with a duration of 20 ns (blue). Afterwards, it is brought into resonance with TLS2 (7.734 MHz) for 11 ns which results in a $\pi/2$-rotation (green). Then, the qubit is biased at different frequencies and hold there for a varying time

t (purple). Before the pulse sequence terminates with the readout pulse (grey), a second $\pi/2$-rotation is performed between the qubit and TLS2 (green).

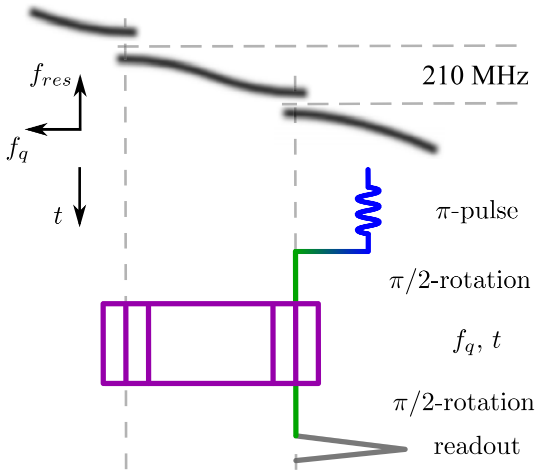

Figure 4.13: Pulse sequence. After entangling the excited qubit with TLS2 it is detuned for the time t. Before the readout it performs a second $\pi/2$-rotation with TLS2. Thus, it imitates the Ramsey experiment.

The idea for this measurement is somehow similar to the Ramsey experiment (Sec. 3.1.6), where the qubit, starting from the ground state, is rotated by a microwave $\pi/2$-pulse resulting in the state $|-_i\rangle = (|0\rangle - i|1\rangle)/\sqrt{2}$ (Eq. 3.4) and after free evolution is followed by an additional $\pi/2$-pulse and readout. In contrast, in our experiment the excited qubit performs a $\pi/2$-rotation due to the interaction with TLS2 which results in the state $|+_i\rangle^{qs} = (|0e\rangle + i|1g\rangle)/\sqrt{2}$ (Eq. 4.2). The same comparison can be also applied when considering the second $\pi/2$-pulse and the corresponding rotation. The difference between the Ramsey fringes and the experiment presented here is reflected during the "free" evolution of the qubit. While in the Ramsey experiment the microwave is turned off and the qubit can really precise around its z-axis, the coupling between the qubit and a TLS is always present. Therefore, if the qubit is in resonance with TLS2 we measure oscillations, and only in the off-resonant limit the fringes are reproduced. The measurement and the simulation of this Ramsey-like experiment are presented on Fig. 4.14(a). The Fourier Transform of the time evolution is displayed on Fig. 4.14(b) (experiment) and (c) (simulation). The hyperbola seen on the lowest graphs is described by the relation (3.15, with $E = \hbar\delta$) $\omega = \sqrt{\delta^2 + (g_2/\hbar)^2}$, where g_2 is the coupling strength between qubit and TLS2. The red round areas on the surface are artifacts. Due to a step in f_q of 3 MHz and in f of 5 MHz (maximal measured time between the two $\pi/2$-rotations amounts to 200 ns) the resolution is not high enough for the smoothing procedure in Matlab®. Nevertheless, the theory reproduces the experimental data with good accuracy.

To have a tripartite system we have to establish interaction with TLS1. Therefore, between the two $\pi/2$-rotations the qubit is tuned to frequencies around TLS1 which has its resonance 210 MHz above TLS2. Without any TLSs one would expect to see just oscillations with approximately the detuning frequency as it is shown in Fig. 3.5(b). The analysis of the measurement would be the same as that of the generation of the states $|\pm\rangle^{qs}$ with two rotations (Sec. 4.2.2), but with variable detuning δ and a fixed time t_2 of 11 ns.

However, due to presence of two TLSs, the time evolution of our tripartite system is more complex. The basis of the total system consists of the 8 states constructed from the eigenstates of the three subsystems. The notation is $\{|e\rangle, |g\rangle\} \otimes \{|1\rangle, |0\rangle\} \otimes \{|e\rangle, |g\rangle\}$, where the first and the third bracket corresponds to TLS1 and TLS2, respectively. Since the total system has only one excitation, we can neglect higher excited states. The ground state $|g0g\rangle$ is also disregarded since it does not interact with other states. Therefore, we can restrict ourselves to the 3-dimensional subspace $\{|e0g\rangle, |g1g\rangle, |g0e\rangle\}$ and the corresponding Hamiltonian

$$H = \begin{pmatrix} E_{e0g} & g_1/2 & 0 \\ g_1/2 & E_{g1g} & g_2/2 \\ 0 & g_2/2 & E_{g0e} \end{pmatrix}, \tag{4.13}$$

where g_1 and g_2 define the qubit-TLS1 and qubit-TLS2 coupling constants, respectively. We set the energy level for TLS2 E_{g0e} to zero and denote the energy of TLS1 E_{e0g} as $\hbar\Delta$. Furthermore, we neglect the influence of one TLS when the qubit is near resonance with the other. We take also use of the states defined in Eq. (4.2) between qubit and TLS2. We start the analysis with the initial state $|\psi_0\rangle$ after the excitation of the qubit

$$|\psi_0\rangle = \begin{pmatrix} 0 \\ 1 \\ 0 \end{pmatrix}. \tag{4.14}$$

The unitary matrix for the $\pi/2$-rotation between qubit and TLS2 can be written as (Eq. 3.16)

$$U_{\pi/2} = \frac{1}{\sqrt{2}} \begin{pmatrix} 1 & -i \\ -i & 1 \end{pmatrix}. \tag{4.15}$$

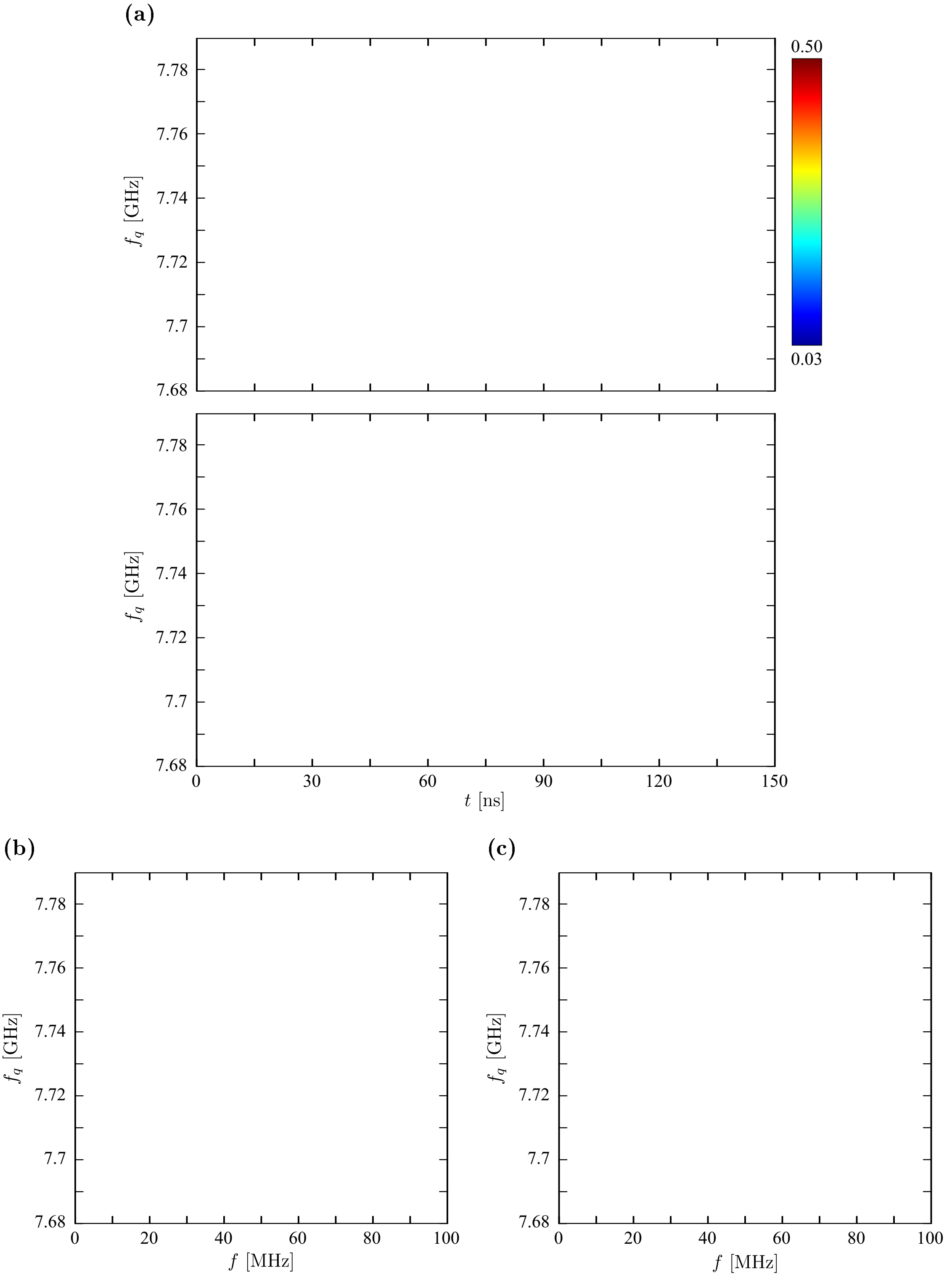

Figure 4.14: Coherent dynamics between qubit and TLS2. **(a)** Time domain measurement (upper plot) and simulation (lower plot). Near resonance the beating between qubit and TLS2 is observed. In the off-resonant limit fringes as in the Ramsey experiment can be seen. The Fourier Transformation of both measurement **(b)** and simulation **(c)** is shown. The red round areas are artifacts.

Thus, by taking into account TLS1, the total matrix has the form

$$U_0 = \begin{pmatrix} e^{-i\Delta t_0} & 0 \quad 0 \\ 0 & \\ 0 & U_{\pi/2} \end{pmatrix}, \tag{4.16}$$

where $t_0 = 11$ ns is the time needed for the rotation. The upper TLS acquires the phase Δt_0, and

$$U_0|\psi_0\rangle = \frac{1}{\sqrt{2}}\begin{pmatrix} 0 \\ 1 \\ -i \end{pmatrix} \propto |g\rangle|+_i\rangle^{qs}. \tag{4.17}$$

When the qubit is near resonance with TLS1, TLS2 evaluates freely, and we can restrict ourselves to the subspace $\{|e0g\rangle, |g1g\rangle\}$. The time evolution operator U_{TLS1} (Eq. 3.16) is

$$U_{TLS1} = \begin{pmatrix} \cos\frac{v_1}{2}t + i\sin\frac{v_1}{2}t\,\cos\alpha & -i\sin\frac{v_1}{2}t \\ -i\sin\frac{v_1}{2}t & \cos\frac{v_1}{2}t - i\sin\frac{v_1}{2}t\,\cos\alpha \end{pmatrix}, \tag{4.18}$$

where $v_1 = g_1/\hbar$ and $\tan\alpha = -g_1/(E_{g1g} - \hbar\Delta)$ (Eq. 3.10.) The time operator for the tripartite system then reads

$$U_1 = \begin{pmatrix} e^{-i\Delta t} \cdot U_{TLS1} & & \begin{matrix} 0 \\ 0 \end{matrix} \\ 0 & 0 & 1 \end{pmatrix}. \tag{4.19}$$

The last rotation before the readout of the qubit equals the first rotation U_0. That means, the maximal probability to measure the qubit in the excited state is provided by the state $|g\rangle|-_i\rangle^{qs}$.

By a small transformation and by using Eq. (4.17) we can significantly simplify the expression to find the qubit in the excited state after the pulse sequence:

$$\mathcal{P}(t,\alpha) = |\langle\psi_0|U_0U_1U_0|\psi_0\rangle|^2 = |\langle U_0^\dagger\psi_0|U_1|U_0\psi_0\rangle|^2 = |\ {}^{qs}\langle -_i|\langle g|U_1|g\rangle|+_i\rangle^{qs}|^2 \tag{4.20}$$

The expression $\langle g|U_1|g\rangle$ shrinks the 3x3 matrix U_1 to a 2x2 matrix U_{eff} by canceling the entries corresponding to the state $|e0g\rangle$ (the upper row and the left column).

$$U_{eff} = \begin{pmatrix} e^{-i\Delta t}\left(\cos\frac{v_1}{2}t - i\sin\frac{v_1}{2}t\,\cos\alpha\right) & 0 \\ 0 & 1 \end{pmatrix}, \tag{4.21}$$

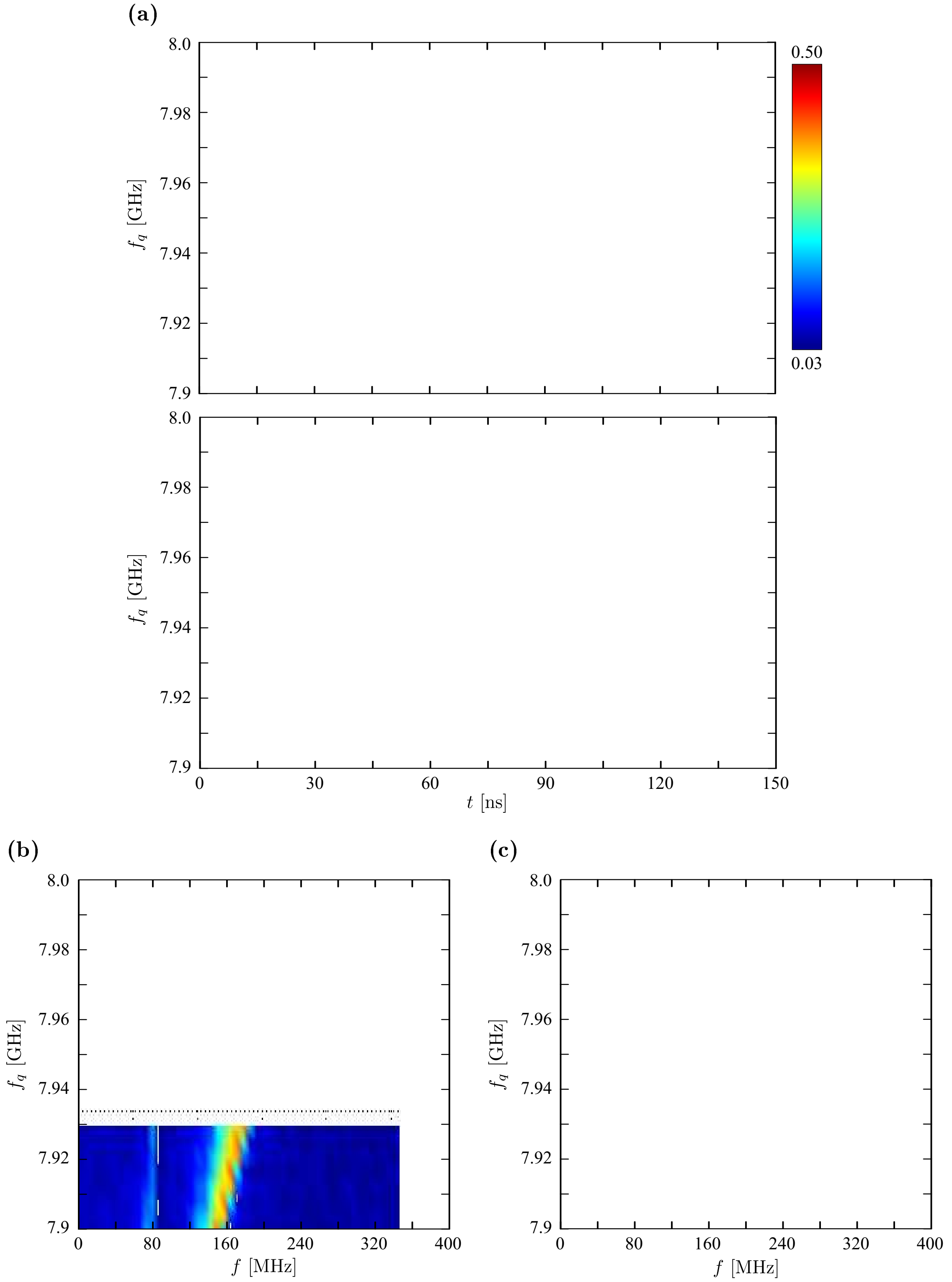

Figure 4.15: Coherent dynamics between qubit, TLS1 and TLS2. **(a)** At frequencies of TLS1 an interference pattern is observed. The upper plot shows the measurement and the lower one the simulation. The Fourier Transformation is displayed in **(b)** (experiment) and **(c)** (theory). At the resonance condition, the oscillations consist of the frequencies 35 MHz, 210 ± 18 MHz.

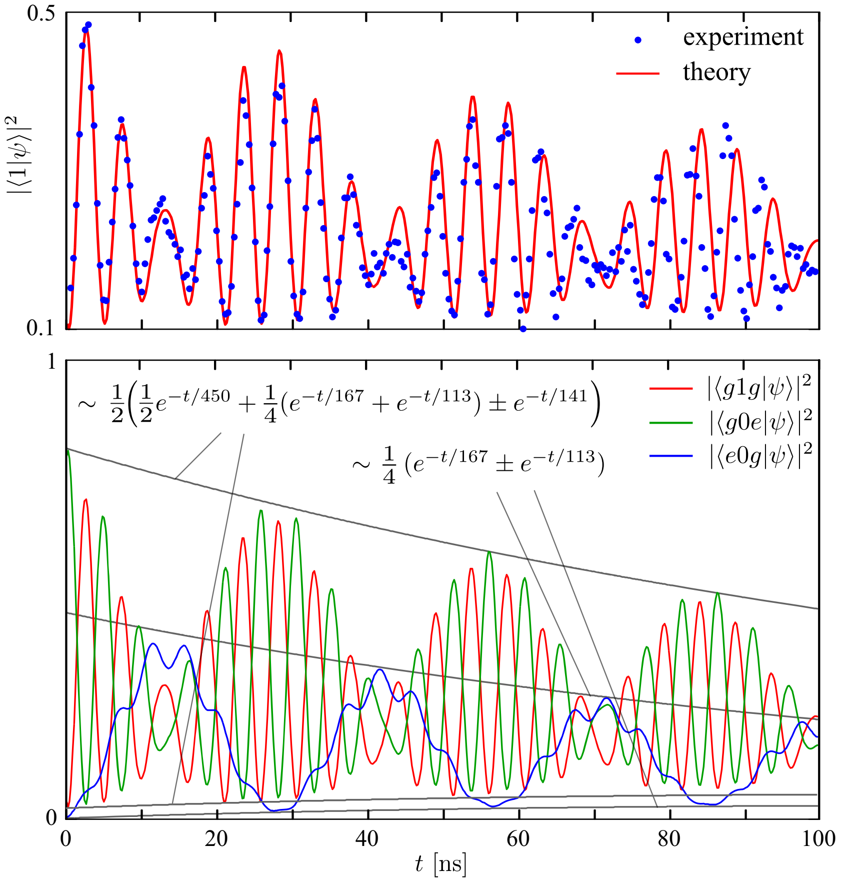

Figure 4.16: **(a)** The cut from the surface plots displayed in Fig. 4.15(a) at the resonance condition is shown. **(b)** The curves of the probabilities to find each subsystem in its excited state are plotted. The corresponding envelopes which possess exponential behavior are also shown.

and so

$$\mathcal{P}(t,\alpha) = \left|\frac{1}{2}\begin{pmatrix} i & 1\end{pmatrix} U_{eff} \begin{pmatrix} i \\ 1\end{pmatrix}\right|^2 = \left|1 - e^{-i\Delta t}\left(\cos\frac{v_1}{2}t + i\sin\frac{v_1}{2}t\,\cos\alpha\right)\right|^2 \qquad (4.22)$$

The experimental results and the simulation are shown in Fig. 4.15(a). One can see fast oscillations which appear and disappear with a smaller frequency. The Fourier Transformation for the experimental and theoretical time evolution is shown in Fig. 4.15(b) and (c). At the resonance condition with TLS1, it shows a peak at a frequency of 35 MHz. That is due to coupling between qubit and TLS1. Near the resonance with TLS1 an avoided level crossing is easily recognized. The splitting equals 35 MHz.

To compare the experimental and theoretical agreement directly we look at the oscillations at the resonance condition with TLS1 (Eq. 4.22). The analytical expression to find the qubit in the excited state is

$$\begin{aligned}\mathcal{P}_{res}\left(t, \alpha = \frac{\pi}{2}\right) &= \left|1 - e^{-i\Delta t}\cos\frac{v_1}{2}t\right|^2 \\ &= \frac{1}{4}\left(\frac{3}{2} + \frac{1}{2}\cos v_1 t - \cos\left[\left(\Delta - \frac{v_1}{2}\right)t\right] - \cos\left[\left(\Delta + \frac{v_1}{2}\right)t\right]\right).\end{aligned} \tag{4.23}$$

The cut from the measurement at 7.944 GHz and the corresponding simulated curve are shown in the upper plot of Fig. 4.16. The amplitude and the offset of the theoretical curve were fitted to the experimental data. One can see the same behavior of the measurement and theory. The equation (4.23) proves that the oscillations consist of three angular frequencies: v_1 and $\Delta \pm v_1/2$. At times where the fast oscillations vanish the qubit has transferred all its energy to TLS1, the following $\pi/2$-rotation with TLS2 yields the probability of 1/4 to measure the qubit in the excited state. On the other hand, maximal oscillations are observed when the qubit is tuned back to TLS2 with maximal excitation. The simulated excitations for TLS1 (blue) and TLS2 (green) are displayed in the lower plot of Fig. 4.16. The qubit (red) and TLS2 are in antiphase with each other, as expected. The fast oscillations between qubit and TLS2 disappear when TLS1 is maximally excited. The amplitude of the $|e0g\rangle$ state (TLS1) shows also fast small oscillations. The Fourier Transformation of this curve (not shown) proves the beating frequency of g_1/h and contains additional two peaks at frequencies of $\Delta/2\pi \pm g_1/2h$.

It is also interesting to verify the calculations of Müller *et al.* [41]. In his paper, he considers the decay of the oscillations between the qubit and TLSs. We discussed in Sec. (3.2.2) the two cases, where the qubit is in resonance and off-resonance with one TLS. Here, I would like to combine the two limits. The qubit is on one hand in resonance with TLS1, on the other hand it is detuned from TLS2. The values for the characteristic times are summarized in Tab. 4.1 and the envelopes for the oscillations are plotted in the lower part of Fig. 4.16. The rates for decoherence of the qubit-TLS1 system in resonance are denoted as $\Gamma_{av}^{qs1} = (\Gamma_1^q + \Gamma_1^{s1})/2$ (averaged decay rates) and $\Gamma_2^{qs1} = (\Gamma_2^q + \Gamma_2^{s1})/2$ (averaged dephasing rates). They are calculated to be

$$\Gamma_{av}^{qs1} = 1/167 \text{ ns and } \Gamma_2^{qs1} = 1/171 \text{ ns}. \tag{4.24}$$

Thus, the inverse decay characteristic time for the oscillations equals

$$\Gamma_{osc}^{qs1} = \frac{1}{2}\Gamma_{av} + \Gamma_2^{qs1} = 1/113 \text{ ns}. \tag{4.25}$$

When taking also the off-resonant TLS2 into account, the decay of the average value of the oscillations of the qubit will consist of the three exponential terms with Γ_{av}^{qs1}, Γ_{osc}^{qs1} and Γ_1 of TLS2. The damping rate of these oscillations Γ_{osc}^{off} is calculated to be

$$\Gamma_{osc}^{off} = \Gamma_2^{qs1} + \Gamma_2^{s2} = 1/141 \text{ ns}. \tag{4.26}$$

By adding these terms with corresponding coefficients, the envelope for the qubit to be in the excited state can be expressed as

$$\sim \frac{1}{2}\left(\frac{1}{2}e^{-t/450} + \frac{1}{4}(e^{-t/167} + e^{-t/113}) \pm e^{-t/141}\right) \tag{4.27}$$

The time t is measured in ns. The exponentially decaying curves are plotted in the lower part of Fig. 4.16. They fit the relaxation of the tripartite system very well.

4.3.3 Proof of TLS entanglement by analyzing the beating frequencies

In the following, we present an experiment that proves the entanglement between TLS1 and TLS2. The measurement reveals the beating frequencies between entangled and independently excited TLSs. Due to the complexity of the pulse sequences and the resulting dynamics of the total system, we omit here unnecessary details of the analysis.

The two pulse sequences are shown in Fig. 4.17. As explained in the previous section, the entanglement between two TLSs (Fig. 4.17(a)) is achieved by exciting the qubit with a π-pulse (blue), performing a $\pi/2$-rotation with one TLS (green), then a π-rotation with the other TLS (red). In the presented experiment we changed the microwave frequency of the π-pulse to 7.462 GHz. Afterwards the qubit is tuned back to the microwave frequency for the time t_1. Since the qubit is now in its ground state, the time evolution of the system can be expressed as

$$|\psi_1\rangle = \frac{1}{\sqrt{2}}(e^{-i\omega_{s1}t_1}|e0g\rangle + e^{-i\omega_{s2}t_1}|g0e\rangle), \tag{4.28}$$

where $\hbar\omega_{s1}$ and $\hbar\omega_{s2}$ are the energies of TLS1 and TLS2. The pulse sequence displayed in Fig. 4.17(b) creates a configuration where the state of the total system is a product state. After applying a $\pi/2$-pulse on the qubit (blue), the state of the qubit is $(|0\rangle - |1\rangle)/\sqrt{2}$. We transfer this state by independent π-rotations on TLS1 (green) and after a second $\pi/2$-pulse on the qubit on TLS2 (red). Thus, we get

$$\begin{aligned} |\overline{\psi_1}\rangle &= \frac{1}{2}\left(|g\rangle + e^{-i\omega_{s1}t_1}|e\rangle\right) \otimes |0\rangle \otimes \left(|g\rangle + e^{-i\omega_{s2}t_1}|e\rangle\right) \\ &= \frac{1}{2}\left(|g0g\rangle + e^{-i\omega_{s2}t_1}|g0e\rangle + e^{-i\omega_{s1}t_1}|e0g\rangle + e^{-i(\omega_{s1}+\omega_{s2})t_1}|e0e\rangle\right), \end{aligned} \tag{4.29}$$

where $|\overline{\psi}\rangle$ denotes the not-entangled state.

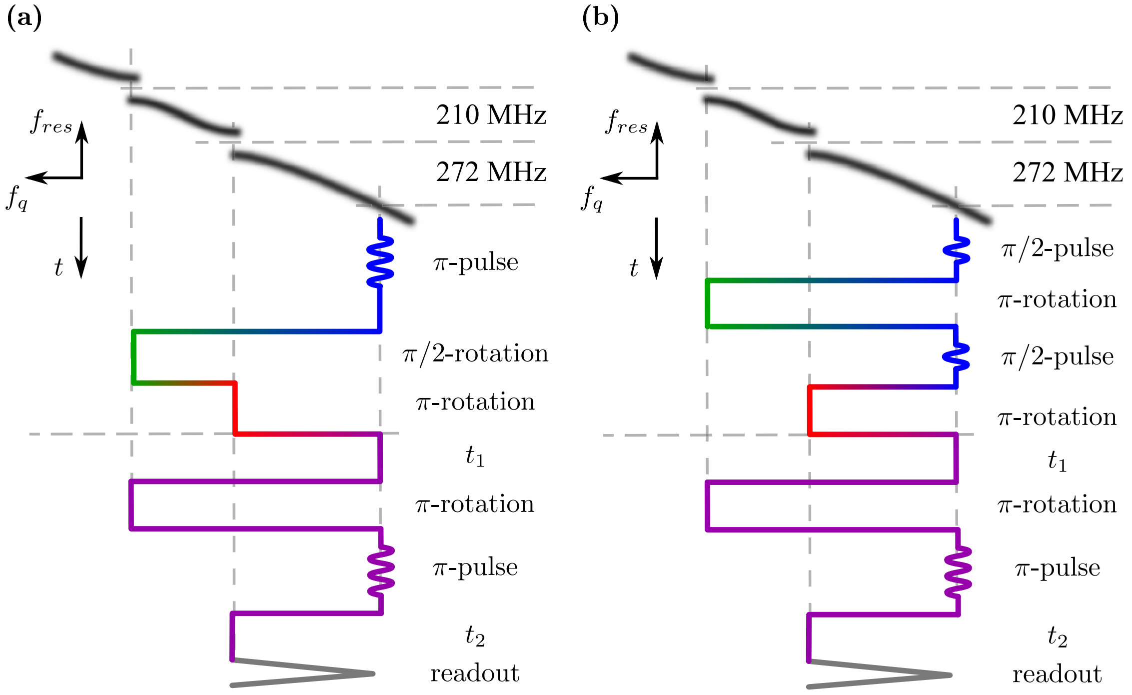

Figure 4.17: Pulse sequences. The bleary black curve symbolizes the resonance spectrum of the qubit. The two pulse sequences prepare either an entanglement between TLS1 and TLS2 **(a)** or a product state between the two TLSs **(b)**. After the preparation, the pulse sequences below the horizontal grey dashed line are equal.

After the time t_1, the continuation of the pulse sequence is for the two cases the same (purple). The qubit is tuned into resonance with TLS1 and a π-rotation is performed transferring the current state of TLS1 to the qubit. Thus, we can eliminate TLS1 from the equations and write the state as

$$|\psi_2\rangle = \frac{1}{\sqrt{2}}\left(e^{-i\omega_{s1}t_1}|1g\rangle + e^{-i\omega_{s2}t_1}|0e\rangle\right) \text{ and} \tag{4.30}$$

$$|\overline{\psi_2}\rangle = \frac{1}{2}\left(|0g\rangle + e^{-i\omega_{s2}t_1}|0e\rangle + e^{-i\omega_{s1}t_1}|1g\rangle + e^{-i(\omega_{s1}+\omega_{s2})t_1}|1e\rangle\right) \tag{4.31}$$

If now the qubit would be brought into resonance with TLS2 for the time t_2, the two results for the entangled and not-entangled case would be very similar. The states $|1g\rangle$ and $|0e\rangle$, depending on their phase, would yield oscillations similar to the chess board shown in Fig. 4.7. Since the ground state $|0g\rangle$ and the double excited state $|1e\rangle$ are eigenstates, they will not contribute to the beatings. Therefore, the only difference would be the amplitude. The oscillations of $|\overline{\psi_2}\rangle$ would have a magnitude which is approximately half of that of the state $|\psi_2\rangle$, which has been observed experimentally.

However, to see crucial different behavior of states, the additional π-pulse on the qubit has to be applied. The unitary matrix for this operation on the qubit reads (Eq. 3.16)

$$H_\pi = \begin{pmatrix} 0 & -i \\ -i & 0 \end{pmatrix}. \tag{4.32}$$

Apart from some phase, this results in an interchange of the ground and the excited state of the qubit. One can see also from the Hamiltonian for the qubit-TLS system in Eq. (3.74) that microwaves turn on the coupling between the states $|0g\rangle$ and $|1g\rangle$, and between the states $|0e\rangle$ and $|1e\rangle$. We can neglect any oscillations between the states $|1g\rangle$ and $|1e\rangle$ since the microwave frequency is detuned from TLS2. Thus,

$$|\psi_3\rangle = \frac{1}{\sqrt{2}}\left(e^{-i\omega_{s1}t_1}|0g\rangle + e^{-i\omega_{s2}t_1}|1e\rangle\right) \text{ and} \tag{4.33}$$

$$|\overline{\psi_3}\rangle = \frac{1}{2}\left(|1g\rangle + e^{-i\omega_{s2}t_1}|1e\rangle + e^{-i\omega_{s1}t_1}|0g\rangle + e^{-i(\omega_{s1}+\omega_{s2})t_1}|0e\rangle\right). \tag{4.34}$$

If now the qubit is tuned into resonance with TLS2, the measurement will yield completely different results. While $|\psi_3\rangle$ is an eigenstate of the total system, the probability of the qubit of the state $|\overline{\psi_3}\rangle$ will oscillate with a frequency $(\omega_{s1}+\omega_{s2})/2\pi$ which is the sum of the TLS1 and TLS2 frequencies. The measurement results are shown in Fig. 4.18. The oscillations depending on the time t_2 occur due to relaxation. After the very first pulse the system starts to decay into the ground state so that the population of the state $|1g\rangle$ after the second π-pulse will be higher than other occupation probabilities. The measurement of the sequence where the TLSs were entangled (Fig. 4.18(a)) shows also small oscillations depending on t_1. The appearence of these oscillations, which are also reproduced by theory (Fig. 4.18(b)), is not obvious and requires further analysis. As expected, the not-entangled TLSs show fast oscillations (Fig. 4.18(c),(d)).

We can compare the results also in the frequency domain by performing the Fourier Transformations of the time t_1 (Fig. 4.19). The possible beating frequencies of the total system are illustrated in Fig. 4.19(e). The entangled TLSs show oscillations with a frequency of slightly above 200 MHz (Fig. 4.19(a),(b)). This

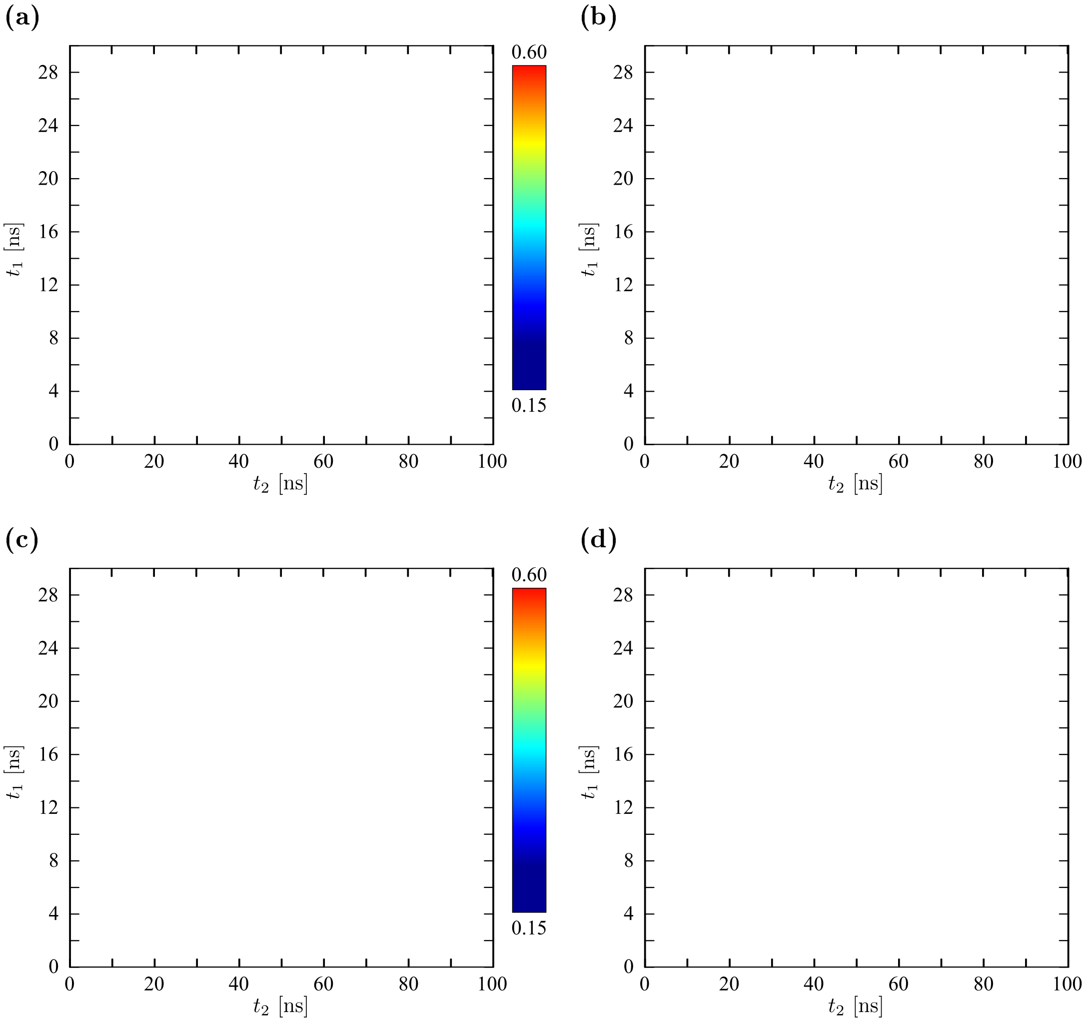

Figure 4.18: The experimental results **(a)** and the theory **(b)** are shown for the case of entangled states. The corresponding measurement and theory for the independently excited TLSs are displayed in **(c)** and **(d)**, respectively. The difference of the two cases are the oscillation frequencies depending on time t_1.

corresponds to the energy difference between the TLSs (210 MHz), however, it is surprisingly to observe this beating. This frequency vanishes if the TLSs are not entangled (Fig. 4.19(c),(d)). Instead of that, fast oscillations appear, which were estimated to have a frequency of 760 MHz. The frequencies of the measurement and the theory show different amplitudes. This discrepancy occurs probably due to calibration errors in the experiment. However, the whole spectrum visible on the measurement plots is also present in the theoretical predictions, though some frequencies are hardly observable on Fig. 4.19(b) and (d).

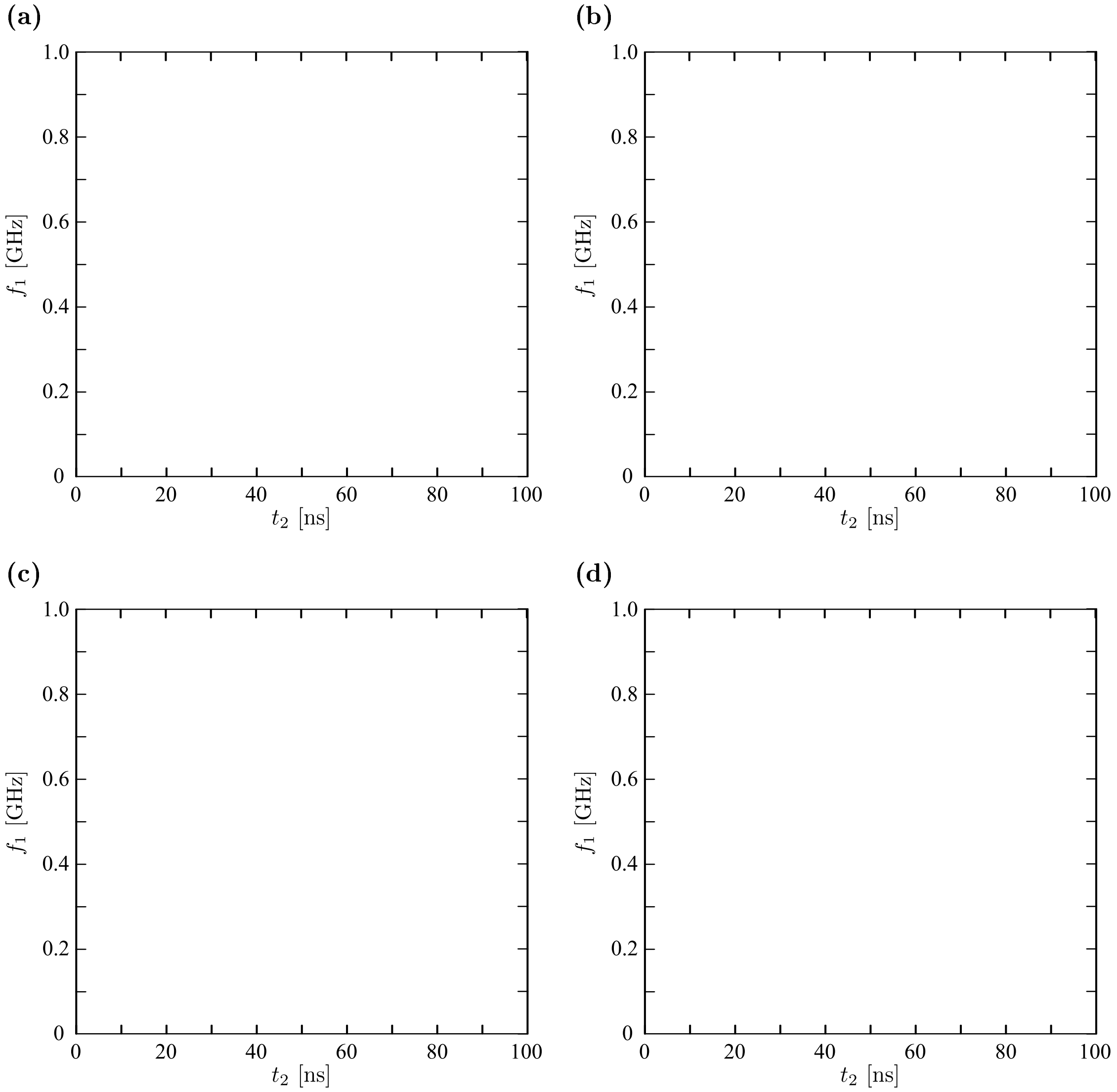

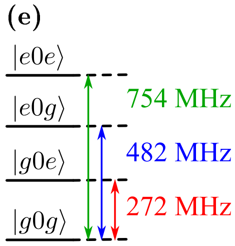

Figure 4.19: **(a)**-**(d)** The Fourier Transformations on t_1 of the corresponding results in Fig. 4.18. One can observe on (c) and (d) the appearance of fast oscillations with the frequency of 760 MHz (no entaglement) in comparison to (a) and (b) where the TLSs were entangled. The possible beating frequencies between the states are illustrated in **(e)**.

Chapter 5

Summary

In this work we present experiments with a phase qubit, consisting of a superconducting loop which is interrupted by a Josephson juntion (JJ) forming an rf-SQUID. In sections 2.1 and 2.2 we described its behavior as a point mass inside an one-dimensional, anharmonic potential. This potential depends on the current flowing through the JJ, and therefore on the applied external magnetic flux in the loop. Thus, the level separation defined by the potential can be tuned, resulting in a change of the resonance frequency of the phase qubit. In section 4.1 we explained the experimental setup and the spectroscopy of the qubit. The resonance frequency can be probed by applying microwave pulses to the qubit and measuring the probability to find the qubit in its excited state.

The spectrum of the phase qubits often contains avoided level crossings, which indicate the presence of microscopic two-level systems (TLSs) coupled to the qubit, see section 3.2. While the exact nature of these TLSs remains unclear, the majority was identified as arising from lattice defects located in the insulating layer of the JJ. We proved experimentally that TLSs constitute coherent quantum systems. In our case, the phase qubit was coupled to two TLSs, whose decay time T_1 exceeded that of the qubit by a factor of 4, and the dephasing time T_2 was limited by T_1 satisfying the relation of an ideal atom $T_2 \approx 2T_1$.

We introduced two ways to analyze the dynamics of this tripartite system. The straightforward way is to use the formalism of the density matrix. Therefore, a simulation in the programming language Matlab® was performed. It takes into account three two-level quantum systems coupled to each other. To include also relaxation and dephasing processes, the simulation solves the master equation in the Lindblad form for the total system consisting of 8 levels. The only parameters the simulation requires are the resonance frequencies and the decoherence times T_1 and T_2 of each subsystem, and the coupling strengths between the phase qubit and each of the two TLSs. We showed that this model is in very good agreement with the coherent dynamics of the total system observed in experiments.

The alternative way to understand the dynamics is more intuitive. We introduced the representation and the time evolution of a two-level quantum system on the Bloch sphere, see section 3.1. Here, the quantum state can be described by the azimuth and polar angle of the Bloch vector of unity length. For a given Hamiltonian, the time evolution of the vector can be visualized by its rotation around the axis defined by the eigenstates. This representation is also useful when considering the qubit-TLS or TLS-qubit-TLS system, if reasonably restricting to a two dimensional subspace. Since during the experiments the total system had only one excitation, the population of states corresponding to more than one excitation can be neglected. The ground state does not interact with other states, and therefore does not affect the rotations. However, the system exponentially decays into the ground state and the contrast of observed quantum beatings goes to zero.

The coupled qubit-TLS system consists of 4 levels. Therefore, only two states remain, whose dynamics can be explained on the Bloch sphere in a very clear way. In section 4.2, we engineered the eigenstates of the qubit-TLS system in resonance by two different approaches: by a double rotation of the Bloch vector around the x- and z-axis, and by a direct rotation around a prepared axis. To prove the preparation of states, we tuned the qubit into resonance with the TLS and observed quantum beatings between the states. Exactly at the times when the eigenstates were generated, the oscillations vanished. Due to this coherence and the high level of control, we demonstrated how to prepare arbitrary states of both the qubit and TLS. Furthermore, we have discussed that these results can be compared to a tomography of the prepared states. The restriction to the two-dimensional subspace results in a Hamiltonian, which has exactly the same form as that of the driven qubit.

For the first time, we managed to observe coherent dynamics between two TLSs resulting in an entanglement between them. This experiment is described in section 4.3. To visualize also the dynamics of the tripartite system TLS-qubit-TLS on the Bloch sphere, we took advantage that the TLSs are separated from each other by more than 200 MHz. Therefore, if the qubit is in resonance with one TLS, the time evolution of the other TLS corresponds to that of a free quantum system. The entanglement between two TLSs is engineered by entangling first the qubit with one TLS and then transferring the remaining excitation of the qubit to the other TLS. We have verified the entangled state by analyzing the beating frequencies. The TLS-qubit-TLS system was prepared once in the state of entangled TLSs and the other time in a separable state of the two TLSs, in which the qubit was in its ground state after the preparation. By applying an additional microwave pulse we could observe oscillations with completely different frequencies. While the beating frequency in the case of entangled states corresponds to the energy difference of the two TLSs, the oscillations in the case of the separable state showed all 4 frequencies corresponding to the energy differences of the four levels.

In conclusion, our experiments show great opportunity for using phase qubits to manipulate and control microscopic two-level defects in solids. Therefore, it is fair to assume that one can also use TLSs as a quantum memory or even as independent qubits.

Bibliography

[1] Markus Ansmann, H. Wang, Radoslaw C. Bialczak, Max Hofheinz, Erik Lucero, M. Neeley, A. D. O'Connell, D. Sank, M. Weides, J. Wenner, A. N. Cleland, and John M. Martinis, *Violation of Bell's inequality in Josephson phase qubits*, Nature **461** (2009), no. 7263, 504–506.

[2] O. Astafiev, Yu. A. Pashkin, Y. Nakamura, T. Yamamoto, and J. S. Tsai, *Quantum Noise in the Josephson Charge Qubit*, Phys. Rev. Lett. **93** (2004), no. 26, 267007.

[3] Antonio Barone and Gianfranco Paterno, *Physics and Applications of the Josephson Effect*, Wiley-VCH, 1982.

[4] P. Bushev, C. Müller, J. Lisenfeld, J. H. Cole, A. Lukashenko, A. Shnirman, and A. V. Ustinov, *Hybrid quantum system surveyed using multi-photon spectroscopy*, ArXiv e-prints (2010).

[5] L. Childress, M. V. Gurudev Dutt, J. M. Taylor, A. S. Zibrov, F. Jelezko, J. Wrachtrup, P. R. Hemmer, and M. D. Lukin, *Coherent Dynamics of Coupled Electron and Nuclear Spin Qubits in Diamond*, Science **314** (2006), no. 5797, 281–285.

[6] I. Chiorescu, Y. Nakamura, C. J. P. M. Harmans, and J. E. Mooij, *Coherent Quantum Dynamics of a Superconducting Flux Qubit*, Science **299** (2003), no. 5614, 1869–1871.

[7] J. I. Cirac and P. Zoller, *Quantum Computations with Cold Trapped Ions*, Phys. Rev. Lett. **74** (1995), no. 20, 4091–4094.

[8] John Clarke and Alex I. Braginski, *The SQUID Handbook: Fundamentals and Technology of SQUIDs and SQUID Systems*, Wiley-VCH; 1 edition, 2004.

[9] John F. Clauser, Michael A. Horne, Abner Shimony, and Richard A. Holt, *Proposed Experiment to Test Local Hidden-Variable Theories*, Phys. Rev. Lett. **23** (1969), no. 15, 880–884.

[10] Claude Cohen-Tannoudji, Bernard Diu, and Frank Laloe, *Quantum Mechanics, Volume 1*, Wiley-Interscience, 2006.

[11] J. H. Cole, J. C. Ang, and A. D. Greentree, *Solving super operator problems*, Centre of Quantum Computer Technology, School of Physics, University of Melbourne, Victoria 3010, Australia, September 17 2009.

[12] Jared H. Cole, Andrew D. Greentree, Daniel K. L. Oi, Sonia G. Schirmer, Cameron J. Wellard, and Lloyd C. L. Hollenberg, *Identifying a two-state Hamiltonian in the presence of decoherence*, Phys. Rev. A **73** (2006), no. 6, 062333.

[13] G. M. D'Ariano, U. Leonhardt, and H. Paul, *Homodyne detection of the density matrix of the radiation field*, Phys. Rev. A **52** (1995), no. 3, R1801–R1804.

[14] M. H. Devoret, A. Wallraff, and J. M. Martinis, *Superconducting Qubits: A Short Review*, ArXiv Condensed Matter e-prints (2004).

[15] Bernard Diu, Claude Cohen-Tannoudji, and Frank Laloe, *Quantum Mechanics, Volume 2*, Wiley-Interscience, 2006.

[16] David P. DiVincenzo, *The Physical Implementation of Quantum Computation*, Fortschritte der Physik **48** (2000), no. 9-11, 771–783.

[17] G. J. Dolan, *Offset masks for lift-off photoprocessing*, Applied Physics Letters **31** (1977), no. 5, 337–339.

[18] Alex Grishin, Igor V. Yurkevich, and Igor V. Lerner, *Low-temperature decoherence of qubit coupled to background charges*, Phys. Rev. B **72** (2005), no. 6, 060509.

[19] E. L. Hahn, *Spin Echoes*, Phys. Rev. **80** (1950), no. 4, 580–594.

[20] A. Heuer and R. J. Silbey, *Microscopic description of tunneling systems in a structural model glass*, Phys. Rev. Lett. **70** (1993), no. 25, 3911–3914.

[21] Max Hofheinz, H. Wang, M. Ansmann, Radoslaw C. Bialczak, Erik Lucero, M. Neeley, A. D. O'Connell, D. Sank, J. Wenner, John M. Martinis, and A. N. Cleland, *Synthesizing arbitrary quantum states in a superconducting resonator*, Nature **459** (2009), no. 7246, 546–549.

[22] A. A. Houck, D. I. Schuster, J. M. Gambetta, J. A. Schreier, B. R. Johnson, J. M. Chow, L. Frunzio, J. Majer, M. H. Devoret, S. M. Girvin, and R. J. Schoelkopf, *Generating single microwave photons in a circuit*, Nature **449** (2007), no. 7160, 328–331.

[23] http://www.oxford instruments.com.

[24] G. Ithier, E. Collin, P. Joyez, P. J. Meeson, D. Vion, D. Esteve, F. Chiarello, A. Shnirman, Y. Makhlin, J. Schriefl, and G. Schön, *Decoherence in a superconducting quantum bit circuit*, Phys. Rev. B **72** (2005), no. 13, 134519.

[25] E.T. Jaynes and F.W. Cummings, *Comparison of quantum and semiclassical radiation theories with application to the beam maser*, Proceedings of the IEEE **51** (1963), no. 1, 89 – 109.

[26] B. D. Josephson, *The discovery of tunnelling supercurrents*, Rev. Mod. Phys. **46** (1974), no. 2, 251–254.

[27] B. E. Kane, *A silicon-based nuclear spin quantum computer*, Nature **393** (1998), no. 6681, 133–137.

[28] A. Yu. Kasumov, R. Deblock, M. Kociak, B. Reulet, H. Bouchiat, I. I. Khodos, Yu. B. Gorbatov, V. T. Volkov, C. Journet, and M. Burghard, *Supercurrents Through Single-Walled Carbon Nanotubes*, Science **284** (1999), no. 5419, 1508–1511.

[29] E. Knill, R. Laflamme, and G. J. Milburn, *A scheme for efficient quantum computation with linear optics*, Nature **409** (2001), no. 6816, 46–52.

[30] L. D. Landau and L. M. Lifshitz, *Quantum Mechanics (Non-Relativistic Theory) Volume 3*, Butterworth-Heinemann (3 edition), 1981.

[31] Jürgen Lisenfeld, Clemens Müller, Jared H. Cole, Pavel Bushev, Alexander Lukashenko, Alexander Shnirman, and Alexey V. Ustinov, *Rabi spectroscopy of a qubit-fluctuator system*, Phys. Rev. B **81** (2010), no. 10, 100511.

[32] Juergen Lisenfeld, *Experiments on Superconducting Josephson Phase Quantum Bits*, Ph.D. thesis, Friedrich-Alexander-Universität Erlangen-Nürnberg, 2008.

[33] Daniel Loss and David P. DiVincenzo, *Quantum computation with quantum dots*, Phys. Rev. A **57** (1998), no. 1, 120–126.

[34] Vladimir E. Manucharyan, Jens Koch, Leonid I. Glazman, and Michel H. Devoret, *Fluxonium: Single Cooper-Pair Circuit Free of Charge Offsets*, Science **326** (2009), no. 5949, 113–116.

[35] I. Martin, L. Bulaevskii, and A. Shnirman, *Tunneling Spectroscopy of Two-Level Systems Inside a Josephson Junction*, Phys. Rev. Lett. **95** (2005), no. 12, 127002.

[36] John Martinis, *Superconducting phase qubits*, Quantum Information Processing **8** (2009), no. 2, 81–103.

[37] John M. Martinis, K. B. Cooper, R. McDermott, Matthias Steffen, Markus Ansmann, K. D. Osborn, K. Cicak, Seongshik Oh, D. P. Pappas, R. W. Simmonds, and Clare C. Yu, *Decoherence in Josephson Qubits from Dielectric Loss*, Phys. Rev. Lett. **95** (2005), no. 21, 210503.

[38] John M. Martinis, S. Nam, J. Aumentado, and C. Urbina, *Rabi Oscillations in a Large Josephson-Junction Qubit*, Phys. Rev. Lett. **89** (2002), no. 11, 117901.

[39] G. Mauro D'Ariano, M. G. A. Paris, and M. F. Sacchi, *Quantum Tomography*, ArXiv Quantum Physics e-prints (2003).

[40] D. E. McCumber, *Effect of ac Impedance on dc Voltage-Current Characteristics of Superconductor Weak-Link Junctions*, Journal of Applied Physics **39** (1968), no. 7, 3113–3118.

[41] Clemens Müller, Alexander Shnirman, and Yuriy Makhlin, *Relaxation of Josephson qubits due to strong coupling to two-level systems*, Phys. Rev. B **80** (2009), no. 13, 134517.

[42] Rémy Mosseri and Rossen Dandoloff, *Geometry of entangled states, Bloch spheres and Hopf fibrations*, Journal of Physics A: Mathematical and General **34** (2001), no. 47, 10243.

[43] Michael A. Nielsen and Isaac L. Chuang, *Quantum Computation and Quantum Information*, Cambridge University Press, 2000.

[44] E. Paladino, L. Faoro, G. Falci, and Rosario Fazio, *Decoherence and* $1/f$ *Noise in Josephson Qubits*, Phys. Rev. Lett. **88** (2002), no. 22, 228304.

[45] V. V. Schmidt, P. Müller, A. V. Ustinov, and I. V. Grigorieva, *The Physics of Superconductors: Introduction to Fundamentals and Applications*, Springer; 1 edition, 2002.

[46] J. A. Schreier, A. A. Houck, Jens Koch, D. I. Schuster, B. R. Johnson, J. M. Chow, J. M. Gambetta, J. Majer, L. Frunzio, M. H. Devoret, S. M. Girvin, and R. J. Schoelkopf, *Suppressing charge noise decoherence in superconducting charge qubits*, Phys. Rev. B **77** (2008), no. 18, 180502.

[47] Marlan O. Scully and M. Suhail Zubairy, *Quantum Optics*, Cambridge University Press, 1997.

[48] R. W. Simmonds, K. M. Lang, D. A. Hite, S. Nam, D. P. Pappas, and John M. Martinis, *Decoherence in Josephson Phase Qubits from Junction Resonators*, Phys. Rev. Lett. **93** (2004), no. 7, 077003.

[49] Matthias Steffen, M. Ansmann, Radoslaw C. Bialczak, N. Katz, Erik Lucero, R. McDermott, Matthew Neeley, E. M. Weig, A. N. Cleland, and John M. Martinis, *Measurement of the Entanglement of Two Superconducting Qubits via State Tomography*, Science **313** (2006), no. 5792, 1423–1425.

[50] Matthias Steffen, M. Ansmann, R. McDermott, N. Katz, Radoslaw C. Bialczak, Erik Lucero, Matthew Neeley, E. M. Weig, A. N. Cleland, and John M. Martinis, *State Tomography of Capacitively Shunted Phase Qubits with High Fidelity*, Phys. Rev. Lett. **97** (2006), no. 5, 050502.

[51] W. C. Stewart, *CURRENT-VOLTAGE CHARACTERISTICS OF JOSEPHSON JUNCTIONS*, Applied Physics Letters **12** (1968), no. 8, 277–280.

[52] D. J. Van Harlingen, T. L. Robertson, B. L. T. Plourde, P. A. Reichardt, T. A. Crane, and John Clarke, *Decoherence in Josephson-junction qubits due to critical-current fluctuations*, Phys. Rev. B **70** (2004), no. 6, 064517.

[53] D. Vion, A. Aassime, A. Cottet, P. Joyez, H. Pothier, C. Urbina, D. Esteve, and M. H. Devoret, *Manipulating the Quantum State of an Electrical Circuit*, Science **296** (2002), no. 5569, 886–889.

[54] Graham A. Webb, *Nuclear Magnetic Resonance*, Royal Society of Chemistry; 1st Edition. edition, 2010.

[55] K. B. Whaley and J. C. Light, *Rotating-frame transformations: A new approximation for multiphoton absorption and dissociation in laser fields*, Phys. Rev. A **29** (1984), no. 3, 1188–1207.

[56] J. Q. You and Franco Nori, *Superconducting Circuits and Quantum Information*, Physics Today **58** (2005), no. 11, 42–47.

[57] Prof. Dr.Claus Zimmermann, *Quantenoptik*, Internet, 2006, http://www.pit.physik.uni-tuebingen.de/zimmermann/lehre/skripten/Quantenoptik.pdf.

Acknowledgements

First of all, I would like to express my gratitude towards Prof. Dr. Alexey V. Ustinov for letting me work on the very interesting topic of my diploma thesis. His professional and mental support during my work were very helpful for me.

Dr. Pavel Bushev earns my thanks for supervising my work and for our useful discussions. He introduced me to the equipment and the evaluation software needed for our experiments.

I would like to thank Dr. Jared Cole for explaining me theoretical models and supervising my simulation.

My thanks go to Dr. Jürgen Lisenfeld for listening to my professional and private problems, and especially for his changes on the electronics so that I could perform my last measurements more accurately.

I thank Dr. Alexander Lukashenko for millikelvin temperatures and good isolation from the environment.

I would like to thank Philipp, Susanne, Bernhard, Piotr, Sebastian and Anastasia for creating a pleasant and funny atmosphere in the room 410.

A special thanks goes to all members of our group for the nice coffee breaks, collective lunches, funny chats and interesting talks.

Огромное спасибо моим родителям, сестрёнке, Сане и мышам (дети) за вашу моральную поддержку в течении моей учёбы. Без своевременной помощи мамы, моя дипломная работа не нашла бы своего завершения.

Я благодарю мою сне-жінку Танюшку за то, что она есть у меня и за то, что она была вторым корректором. Спасибо дочурке Веруше за то, что она дарила мне свою улыбку каждое утро. А нашей кошке Лизе за то, что она составляла мне компанию в ночные часы лёжа на письменном столе.

Erklärung:

Ich versichere, dass ich diese Arbeit selbstständig verfasst und keine anderen als die angegebenen Quellen und Hilfsmittel benutzt habe.

Karlsruhe, den